Aus dem Pathologischen Institut der

Ludwig-Maximilians-Universität München

Direktor: Prof. Dr. med. Frederick Klauschen

in der DKTK-Arbeitsgruppe „Oncogenic Signaling Pathways in Colorectal and Pancreatic Cancer"

Leiter: Dr. rer. nat. Peter Jung

Dissertation

zum Erwerb des Doctor of Philosophy (Ph.D.)

an der Medizinischen Fakultät der

Ludwig-Maximilians-Universität München

Role of TGF-β/SMAD4/c-MYC-regulated NLE1 in tumor growth and liver metastasis of colorectal cancer

---

vorgelegt von

Leon Peter Loevenich

aus Goch, Deutschland

im Jahr 2023

Gedruckt mit der Genehmigung der Medizinischen Fakultät

der Ludwig-Maximilians-Universität München

Erstgutachter: Prof. Dr. rer. nat. Heiko Hermeking

Zweitgutachter: Dr. rer. nat. Peter Jung

Dekan: Prof. Dr. med. Thomas Gudermann

Tag der mündlichen Prüfung: 26.09.2023

To everyone who supported me.

Affidavit

Loevenich, Leon Peter

Thalkirchner Str. 36

80337 Munich

Germany

I hereby declare that the submitted thesis entitled

“Role of TGF-β/SMAD4/c-MYC-regulated NLE1 in tumor growth and liver metastasis of colorectal cancer”

is my own work. I have only used the sources indicated and have not made unauthorized use of services of a third party. Where the work of others has been quoted or reproduced, the source is always given.

I further declare that the dissertation presented here has not been submitted in the same or similar form to any other institution for the purpose of obtaining an academic degree.

Munich, 11.10.2023	Leon Loevenich
Place, date	Signature doctoral candidate

Confirmation of congruency between printed and electronic version of the doctoral thesis

Loevenich, Leon Peter

Thalkirchner Str. 36

80337 Munich

Germany

I hereby declare that the electronic version of the submitted thesis entitled

“Role of TGF-β/SMAD4/c-MYC-regulated NLE1 in tumor growth and liver metastasis of colorectal cancer”

is congruent with the printed version both in content and format.

Munich, 11.10.2023	Leon Loevenich
Place, date	Signature doctoral candidate

Publications

Parts of this thesis have been published in the following article:

Leon P. Loevenich, Markus Tschurtschenthaler, Matjaz Rokavec, Miguel G. Silva, Moritz Jesinghaus, Thomas Kirchner, Frederick Klauschen, Dieter Saur, Jens Neumann, Heiko Hermeking, Peter Jung. 2022. "SMAD4 loss induces c-MYC-mediated NLE1 upregulation to support protein biosynthesis, CRC growth and metastasis." Cancer Res. 2022 Oct 11:CAN-22-1247. doi: 10.1158/0008-5472.CAN-22-1247.

In addition, I contributed to the following articles, which are not further described here:

Sophie L. Boos, **Leon P. Loevenich**, Sebastian Vosberg, Thomas Engleitner, Rupert Oellinger, Jörg Kumbrink, Marlies Michl, Philipp A. Greif, Andreas Jung, Heiko Hermeking, Jens Neumann, Thomas Kirchner, Roland Rad, Peter Jung. 2022. “Disease Modeling on Tumor Organoids Implicates AURKA as a Therapeutic Target in Liver Metastatic CRC.” Cell Mol Gastroenterol Hepatol. 2022;13(2):517-540. doi: 10.1016/j.jcmgh.2021.10.008.

Table of contents

List of abbreviations

2'-O-Me ..... ribose 2'-O methylation
ACTB ..... Actin, beta
ANOVA ..... Analysis of variance
AOM ..... Azoxymethane
APC ..... Adenomatous polyposis coli
AXIN2 ..... Axis inhibition protein 2
BCL-xL ..... B-cell lymphoma-extra large
BIM ..... Bcl-2 interacting mediator of cell death
BMP ..... bone morphogenetic protein
BOP1 ..... Block of Proliferation 1
BRAF ..... B-Raf Proto-Oncogene, Serine/Threonine Kinase
BSA ..... Bovine serum albumin
Cas9 ..... CRISPR-associated protein 9
Ccl20 ..... C-C motif chemokine ligand 20
CCL9 ..... C-C motif chemokine ligand 9
CCR1 ..... C-C chemokine receptor type 1
CCSC ..... CRC stem cells
CDC42 ..... Cell division control protein 42 homolog
CDKN1A ..... Cyclin-dependent kinase inhibitor 1
CDKN1B ..... Cyclin-dependent kinase inhibitor 1B
CDKN2A ..... Cyclin-dependent kinase inhibitor 2A
CDKN2B ..... Cyclin-dependent kinase inhibitor 2B
cDNA ..... Complementary DNA
CFLAR ..... CASP8 and FADD-like apoptosis regulator
ChIP ..... Chromatin-Immunoprecipitation
CHX ..... Cycloheximide
CI ..... confidence interval
cIAP ..... cellular inhibitor of apoptosis protein
CIMP ..... CpG island methylator phenotype
CIN ..... Chromosomal instability
CLL ..... Chronic Lymphocytic Leukemia
CMS ..... Consensus molecular subtypes
COAD ..... Colon Adenocarcinoma
CQ ..... chloroquine
CRC ..... Colorectal cancer
Cre ..... Causes recombination
CRIS ..... CRC intrinsic subtypes
CRISPR ..... Clustered regularly interspaced short palindromic repeats
CSCs ..... Cancer stem cells
CTCs ..... Circulating tumor cells
CVH ..... Chronic vascular permeability
CXCL11 ..... C-X-C motif chemokine ligand 11
CXLC12 ..... C-X-C motif chemokine ligand 12
DAB ..... 3,3'-diaminobenzidine
DAPI ..... 4',6-diamidino-2-phenylindole
DAPK ..... Death associated protein kinase
ddH_2O ..... double distilled water
DepMap ..... Cancer Dependency Map
DKC1 ..... Dyskerin pseudouridine synthase 1
DMAB ..... 3,2'-dimethyl-4-aminophenyl
DMEM ..... Dulbecco's modified eagle medium
DMH 1,2-dimethylhydrazine
DMSO ..... Dimethylsulfoxide
DNA ..... Deoxyribonucleic acid
DSS ..... dextran sodium sulfate
DTT ..... Dithiothreitol
E2F1 ..... E2F transcription factor 1

ECM ..... extracellular matrix
EDTA ..... Ethylenediaminetetraacetic acid
EdU ..... 5-ethynyl-2'-deoxyuridine
EGF ..... Epidermal Growth Factor
EGFR ..... Epidermal growth factor receptor
EMT ..... Epithelial-to-Mesenchymal transition
ENCODE ..... Encyclopedia of DNA elements
EpCAM ..... Epithelial cell adhesion molecule
EpCAM^{MT} ..... membrane-truncated form of EpCAM
ERK1/2 ..... Mitogen-activated protein kinase 1/3
FACS ..... Fluorescence-activated cell sorting
FAP ..... Familial adenomatous polyposis
FBL ..... fibrillarin
FBS ..... Fetal bovine serum, Fetal bovine serum
FFPE ..... Formalin-fixed and paraffin-embedded
FITC ..... fluorescein isothiocyanate
FPKM ..... fragments per kilobase of exon per million mapped fragments
GADD45ß ..... Growth arrest and DNA-damage-inducible 45ß
Gal-LCP ..... galactose-targeted lipid calcium phosphate
GAPDH ..... Glyceraldehyde 3-phosphate dehydrogenase
GDC ..... National Cancer Institute's Genomic Data Commons
GEMM ..... Genetically engineered mouse models
GEO ..... Gene Expression Omnibus
GINS2 ..... GINS Complex Subunit 2
GNI ..... Gross national income
GSEA ..... Geneset Enrichment Analysis
GTPase ..... Guanosine-5'-triphosphatase
HBSS ..... Hank's-balanced salt solution, Hank's balanced salt solution
HDI ..... Human Development Index
HNPCC ..... Hereditary nonpolyposis colon cancer
HR ..... hazard ratio
HRP ..... Horseradish peroxidase, horseradish peroxidase
IFITM3 ..... Interferon-Induced Transmembrane Protein 3
IGF2 ..... Insulin-like growth factor 2
IgG ..... Immunoglobulin G
IKK-β ..... inhibitor of nuclear factor kappa B kinase subunit β
IRES ..... internal ribosome entry site
IVC ..... individually ventilated cages
JNK ..... c-Jun N-terminal kinase
KIRC ..... Kidney renal cell carcinoma
KRAS ..... Kirsten rat sarcoma virus
LAS1L ..... LAS1-like ribosome biogenesis factor
LB ..... Luria-Bertani
LC3B ..... Microtubule-associated protein 1 light chain 3 beta
LGR5 ..... Leucine-rich repeat-containing G-protein coupled receptor 5
LMU ..... Ludwig-Maximilians-University
LOH ..... Loss of heterozygosity
LoxP ..... locus of X-over P1
LSM6 ..... U6 snRNA-associated Sm-like protein LSm6
MAPK ..... mitogen-activated protein kinase
MCL1 ..... Myeloid cell leukemia 1
MDM2 ..... Mouse double minute 2 homolog
MEK ..... Mitogen-activated protein kinase kinase
MEM ..... Minimal Essential Medium
MFI ..... Mean fluorescence intensity
min ..... multiple intestinal neoplasia
MKI67 ..... Marker of Proliferation Ki-67
MLH1 ..... Mut L homolog 1
MMP9 ..... matrix metallopeptidase 9
MNNG ..... N-methyl-N-nitrosoguanidine
MNU ..... N-methyl-N-nitrosourea

mRNAs ..... messenger ribonucleic acids
MSH2 ..... Mut S homolog 2
MSH6 ..... Mut S homolog 6
MSI ..... Microsatellite instability
MSigDB ..... Molecular Signatures Database
mTOR ..... mammalian target of rapamycin
MTOs ..... murine tumor organoids
NAC ..... N-acetyl-cysteine
NaCl ..... Sodium chloride
NAT10 ..... N-Acetyltransferase 10
NaVO3 ..... Sodium metavanadate
NCBI ..... National Center for Biotechnology Information
NF-κB ..... nuclear factor κ-light-chain-enhancer of activated B cells
NGS ..... Next-Generation Sequencing
NK cells ..... Natural killer cells
NLE1 ..... Notchless homolog 1
NORs ..... Nucleolar organizer regions
NPM1 ..... Nucleophosmin
NSG NOD.Cg.PrkdcscidI12rgtm1Wj1/SzJ
OPP ..... O-propargyl-puromycin
ORF ..... Open reading frame
PARP ..... Poly ADP-ribose polymerase
PBS ..... Phosphate-buffered saline
PCR ..... Polymerase chain reaction
PDK1 ..... Pyruvate dehydrogenase lipoamide isozyme 1
PDTOs ..... Patient-derived tumor organoids
PDX ..... Patient-derived xenograft
PEI ..... Polyethylenimine
PES1 ..... Pescadillo ribosomal biogenesis factor 1
PFA ..... Paraformaldehyde
PhIP ..... 2-amino-1-methyl-6-phenylimidazo(4,5-b)pyridine
PI3K ..... Phosphoinositide 3-kinase
PKB ..... Protein kinase B
PMEPA1 ..... Transmembrane prostate androgen-induced protein
PMS2 ..... Postmitotic segregation 2
PMSF ..... Phenylmethylsulfonylfluoride
POLR1A ..... RNA polymerase I subunit A
POLR3K ..... RNA Polymerase III Subunit K
PPIA ..... Peptidylprolyl isomerase A
pRB ..... retinoblastoma protein
pre-rRNA ..... pre-ribosomal RNA
PRMT1 ..... Protein Arginine Methyltransferase 1
PROTAC ..... proteolysis-targeting chimera
PSMG4 ..... Proteasome Assembly Chaperone 4
PTEN ..... Phosphatase and tensin homolog
PVDF ..... Polyvinylidene fluoride
qChIP ..... Quantitative Chromatin Immunoprecipitation
qRT-PCR ..... quantitative Realtime-PCR
RAF ..... Rapidly Accelerated Fibrosarcoma
Ras ..... Rat sarcoma
RB ..... retinoblastoma protein
rDNAs ..... ribosomal DNAs
READ ..... Rectum Adenocarcinoma
RHOA ..... Ras homolog family member A
RIPA ..... Radioimmunoprecipitation buffer
RNA ..... Ribonucleic acid
RNA Pol I ..... RNA polymerase I
RNA Pol II ..... RNA Polymerase II
RNA Pol III ..... RNA Polymerase III
RNAi ..... RNA interference
ROS ..... Reactive oxygen species

RPLP0 ..... ribosomal protein lateral stalk subunit P0
RPLP1 ..... ribosomal protein lateral stalk subunit P1
RPLP2 ..... ribosomal protein lateral stalk subunit P2
RPLs ..... L ribosomal proteins
RPSs ..... S ribosomal proteins
rRNAs ..... ribosomal ribonucleic acids
RRP1 ..... Ribosomal RNA processing 1
R-Smads ..... receptor-regulated Smads
RSR ..... ribotoxic stress response
RTCA ..... Real-Time Cell Analyzer
SBR ..... Smad-binding region
SDS ..... Sodium dodecyl sulfate
SDS-PAGE ..... Sodium dodecyl sulfate-polyacrylamide gel electrophoresis
siRNA ..... small interfering RNA
SL1 ..... Selective factor 1
SMAD1 ..... Mothers against decapentaplegic homolog 1
SMAD2 ..... Mothers against decapentaplegic homolog 2
SMAD3 ..... Mothers against decapentaplegic homolog 3
SMAD4 ..... Mothers against decapentaplegic homolog 4
SMAD5 ..... Mothers against decapentaplegic homolog 5
SMAD8 ..... Mothers against decapentaplegic homolog 5
SMOC2 ..... SPARC-related modular calcium-binding protein 2
snoRNA ..... small nucleolar RNA
snoRNPs ..... Small nuclear ribonucleoproteins
SoC ..... Standard of Care
SQSTM1 ..... sequestosome 1
T7EI ..... T7 endonuclease I
TA ..... transit-amplifying
TAE ..... Tris-acetate-EDTA
TBHP ..... Tert-butyl hydroperoxide
TBS ..... Tris-buffered saline
TBS-T ..... TBS-Tween
TCF ..... T-cell factor
TCGA ..... The Cancer Genome Atlas
TEMED ..... Tetramethylethylenediamine
TFIIIB ..... Pol III transcription factor
TGFBR1 ..... Transforming growth factor-beta receptor I
TGFBR2 ..... transforming growth factor-beta receptor II
TGF-β ..... Transforming growth factor-beta
TIC ..... Tumor-initiating cell
TIF-IA ..... transcription initiation factor IA
TME ..... tumor microenvironment
TNBC ..... Triple-Negative Breast Cancer
TOC ..... Tumor organoid culture medium
TP53 ..... Tumor protein P53
Tris ..... 2-Amino-2-(hydroxymethyl)-1,3-propanediol
tRNAs ..... transfer RNAs
UBTF ..... Upstream binding transcription factor
UQ ..... Upper quartile
VEGF ..... Vascular endothelial growth factor
VPF ..... Vascular permeability factor
WDR12 ..... WD repeat domain 12
ΔΔCt ..... delta delta cycle threshold

List of figures

1. Introduction

1.1. Cancer

Cancer is the world's second leading cause of death, with approximately 19.3 million new cases and 10 million caused deaths in 2020 [1, 2]. It represents one of our society's major public health problems [2].

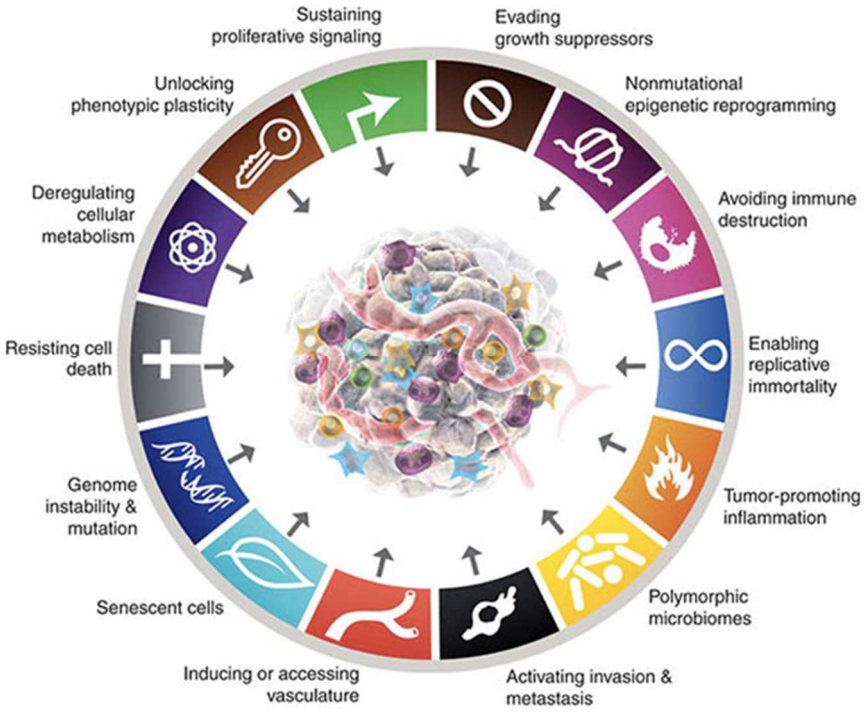

Figure 1: Hallmarks of Cancer
The hallmarks of cancer describe the organizing principle for the diversity of neoplastic disease. They include the following features: "evading growth suppressors, non-mutational epigenetic reprogramming, avoiding immune destruction, enabling replicative immortality, tumor-promoting inflammation, polymorphic microbiomes, activating invasion and metastasis, inducing or accessing vasculature, senescent cells, genome instability, and mutation, resisting cell death, deregulating cellular metabolism, unlocking phenotypic plasticity, sustaining proliferative signaling" [adapted from 3]. Reuse of the figure was allowed by AACR (license number: 5520850050669).

Cancer is a neoplastic disease, progressively evolving from normal cells by acquiring tumorigenic capabilities, the so-called hallmarks of cancer (Figure 1). The first six original hallmarks of cancer were: "sustaining proliferative signaling, evading growth suppressors, activating invasion and metastasis, enabling replicative immortality, inducing angiogenesis, and resisting cell death" [4, 5]. For example, Dvorak *et al.* discovered the induction of angiogenesis as an essential feature for tumor growth in 1979. He described that tumors produce vascular permeability factor (VPF), nowadays renamed vascular endothelial growth factor (VEGF)), which leads to chronic vascular permeability (CVH) and fibrin deposition in wounds and tumors. These findings led to the saying, "Tumors: Wounds that do not heal" [6, 7].

Later, in the course of remarkable progress in cancer research, another set of two emerging hallmarks and two enabling characteristics were added. The two emerging hallmarks were “deregulating cellular energetics” and “avoiding immune destruction”. The two enabling characteristics were “genome instability and mutation” and “tumor-promoting inflammation” [5]. Otto Warburg described one crucial discovery that led to this concept. Cancer cells can reprogram their glucose metabolism to glycolysis – even in the presence of oxygen - thereby limiting their energy metabolism. This state is called “aerobic glycolysis” [8-10].

In 2022, additional hallmarks were included, showing the importance of recent research progress and the complexity of this disease. “Unlocking phenotypic plasticity” and “senescent cells” are the new emerging hallmarks, and “non-mutational epigenetic reprogramming” and “polymorphic microbiomes” are the new enabling characteristics [3]. For example, Hayflick originally discovered senescence in 1961. He demonstrated for the first time that normal human fetal cells enter a senescence phase after 40 to 60 cell divisions. After each cell division, the telomeres are shortened until a critical length is reached. The so-called Hayflick limit [11, 12]. In cancer, senescence can have a tumor-promoting effect. Hwang *et al.* showed that therapy-induced senescence in endothelial cells leads to the secretion of C-X-C motif chemokine ligand 11 (CXCL11), thereby promoting the aggressiveness of breast cancer cells [3, 13].

Finally, these 14 hallmarks are fundamental to our current understanding of cancer development and progression [3].

1.2. Colorectal cancer (CRC)

1.2.1. Incidence

The incidence and mortality of colorectal cancer (CRC) patients are still high, although treatment options are improving continuously [14-16]. In detail, 10.01% of new cancer cases worldwide were diagnosed with CRC in 2020, making it the third most common cancer (Figure 2A). Furthermore, the mortality of CRC accounted for 9.39% worldwide in 2020, making it the second-leading cause of cancer-related deaths (Figure 2B) [1, 17].

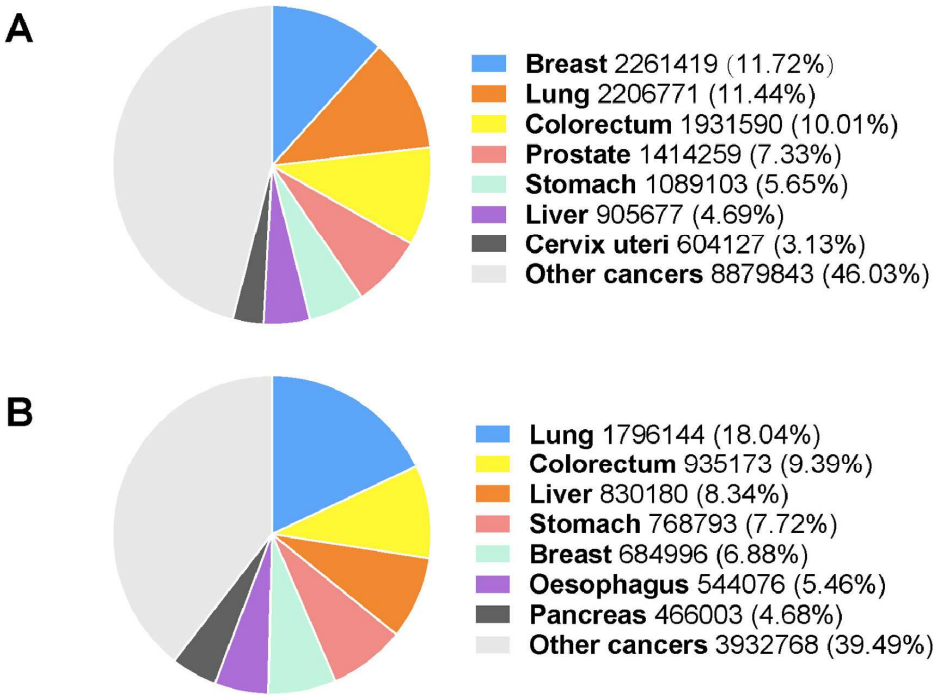

Figure 2: Number of cases and deaths of different cancer types worldwide in 2020
A) Number of estimated new cancer cases in different tumor entities worldwide in 2020. B) Number of estimated cancer-related deaths in different tumor entities worldwide in 2020. Numbers were obtained from the GLOBOCAN study in 2020 [1]. [Figure was derived from 17]. The reuse of figures was allowed by Elsevier (Creative Commons CC-BY-NC-ND license).

Highly developed countries such as Norway, Denmark, and Japan showed the highest age-standardized incidence rates for CRC in 2020. In contrast, less developed countries such as Ghana, Burkina Faso, and Bangladesh showed the lowest age-standardized incidence rates for CRC in 2020. Therefore, the researcher predicted a positive correlation with the Human Development Index (HDI) [1, 17]. The HDI is an index that measures life expectancy, expected years of schooling, and "gross national income (GNI) per capita" (Human Development Reports, https://hdr.undp.org/). Interestingly, the HDI of the Top 10 highest incidence rates was four folds higher compared to the bottom ten lowest incidence rates. Nowadays, a shift in this phenomenon can be observed because highly developed countries are improving their treatment options, and lower developed countries are more often exposed to CRC risk factors. Therefore, incidence rates are declining in HDI-high countries and increasing in HDI-low countries [1, 17].

The reasons for the high incidence and mortality rates of CRC are challenging to define. 60-65% of all CRC patients develop this disease sporadically without any inherited genomic alterations. They acquire different genetic mutations or epigenetic alterations for disease initiation [16, 18, 19]. In contrast, 35-40% of CRC patients suffer from genetic predispositions such as familial adenomatous polyposis (FAP) or Lynch syndrome, also known as hereditary non-polyposis CRC syndrome [20-22]. Nevertheless, environmental

factors such as diet and physical inactivity might also increase the risk of developing cancer [23-25].

1.2.2. Staging

CRC patients are diagnosed concerning how deeply cancer grows into the colonic wall and whether it spreads into other body parts. There are five stages of CRC [26].

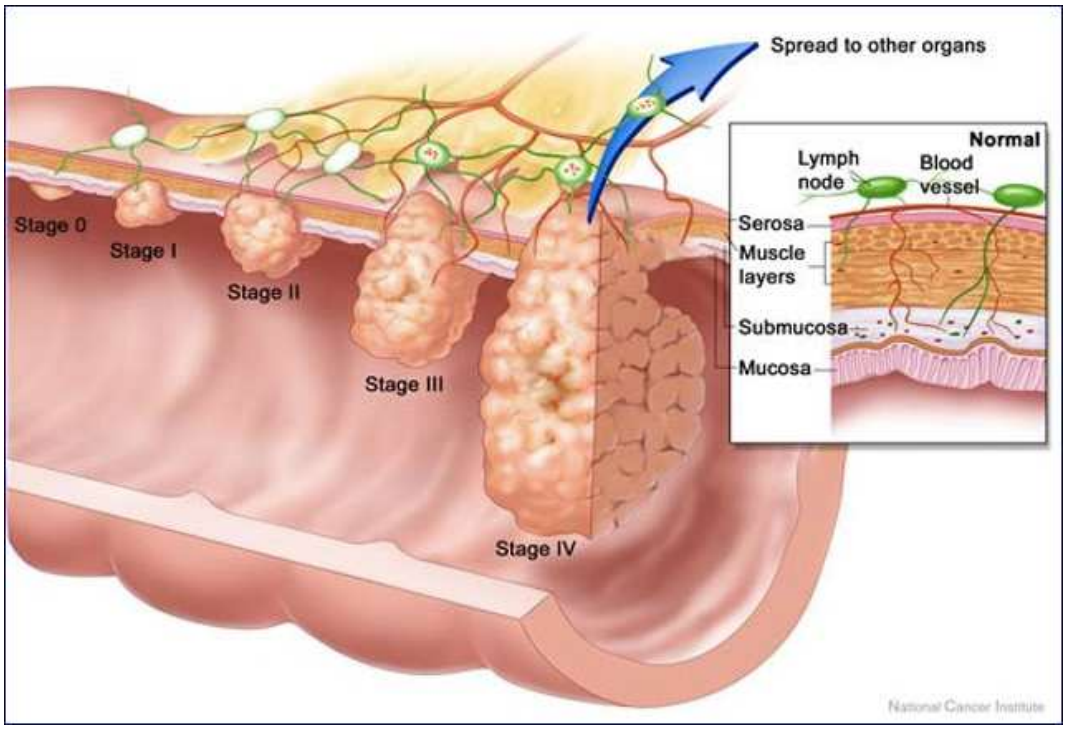

Figure 3: Staging of CRC
The stages of CRC are 0 to IV. Stage 0: Cancer is restricted to the mucosa, also known as 'cancer in situ'. Stage I: Cancer grows through the mucosa of the colon and invades the muscle layer. Stage II: Cancer spreads through the muscle layer/serosa and affects nearby tissue without spreading into lymph nodes. Stage III: Cancer spreads to the lymph nodes near the colon. Stage IV: Cancer spreads to distant body parts, also called metastasis [adapted from 26, 27]. [Figure was derived from 27]. Reuse of the figure was allowed by Springer Nature (license number: 5521250942871).

Stage 0 is the earliest, called ‘cancer in situ’ (Figure 3). It is defined by the accumulation of cancer cells in the mucosa. In stage I, cancer grows through the submucosa of the colon and invades the muscle layer. When cancer spreads through the muscle layer and/or serosa and might affect nearby tissue, it is classified as stage II. Lymph nodes are not involved in this stage. Stage III is defined as the colonization of cancer cells into lymph nodes. When cancer cells infiltrate distant body parts such as the lung or liver, it is defined as stage IV [26].

1.2.3. Genetic alterations

CRC arises from normal colon epithelium by acquiring different genetic and epigenetic alterations, such as gene mutations, gene amplifications, or aberrant deoxyribonucleic

acid (DNA) methylation. These alterations are divided into three different subtypes: Chromosomal instability (CIN), microsatellite instability (MSI), and CpG island methylator phenotype (CIMP) [28].

The CIN subtype is the most frequent cause of CRC, accounting for 80-85% of all CRC cases. It leads to numerous changes in the number of chromosomes, for example, aneuploidy and loss of heterozygosity (LOH) [28, 29]. Especially critical genes such as Adenomatous polyposis coli (*APC*), Kirsten rat sarcoma virus (*KRAS*), Tumor protein P53 (*TP53*), or Mothers against decapentaplegic homolog 4 (*SMAD4*) are affected. The first proposed model addressing in which order these mutations occur was proposed by Fearon and Vogelstein in 1988 (Figure 4) [30].

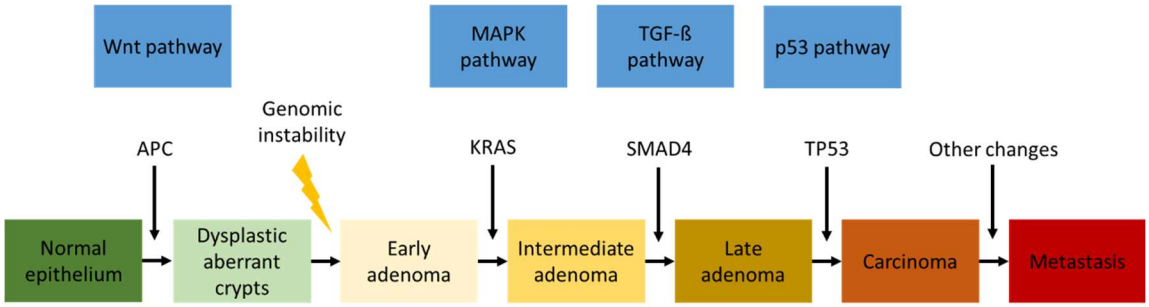

Figure 4: Genetic alterations driving the progression of CRC
Different genetic alterations define the progression of CRC. Pathways commonly affected are highlighted in blue, and the corresponding mutated proteins are described below. APC: Adenomatous polyposis coli, KRAS: Kirsten rat sarcoma virus, TP53: Tumor Protein P53, SMAD4: Mothers against decapentaplegic homolog 4, TGF-β: Transforming growth factor-beta, MAPK: Mitogen-activated protein kinase [based on 30, 31].

Usually, this type of CRC is initiated with the loss of *APC*, leading to constitutive activation of Wnt signaling [32]. In detail, APC is part of the ß-catenin degradation complex and regulates ß-catenin protein levels by blocking its nuclear localization and degrading it. When APC is lost, ß-catenin accumulates and translocates into the nucleus. There, it activates Wnt target genes via DNA-bound T-cell factor (TCF) transcription factors [32-34]. Typical Wnt target genes include Leucine-rich repeat-containing G-protein coupled receptor 5 (*LGR5*), axis inhibition protein 2 (*AXIN2),* and the c-*MYC* oncogene. This process is essential to maintain a proliferative and stem cell-like phenotype, promoting adenoma formation [30, 35, 36].

An activating KRAS gene mutation occurs in 50% of CRC cases [37]. The most common KRAS mutation in CRC is the KRAS G12D mutation [38]. KRAS encodes a guanosine-5'-triphosphatase (GTPase) and activates the phosphoinositide 3-kinase-Pyruvate dehydrogenase lipoamide isozyme 1-Protein kinase B (PI3K-PDK1-PKB) and Rapidly Accelerated Fibrosarcoma-Mitogen-activated protein kinase kinase-Mitogen-activated protein kinase 1/3 (RAF-MEK-ERK1/2) signaling pathways, which suppresses apoptosis

and promotes proliferation [39, 40]. These mutations also correlate with the survival of patients. For example, patients with mutations in KRAS exon 2 codon 13 showed a poorer prognosis, and patients with mutations in KRAS exon 2 codon 12 suffered from a higher metastatic load [41, 42]. Alternatively, mutations in the B-Raf Proto-Oncogene, Serine/Threonine Kinase (*BRAF*) gene occur, activating the BRAF serine-threonine kinase, a downstream mediator of the RAF-MEK-ERK1/2 pathway. These BRAF mutations have similar consequences as KRAS mutations [43, 44].

The next step during CRC progression is the transition from adenomas to carcinomas, usually mediated by the inactivation of TP53 [45]. *TP53* is a tumor suppressor gene on chromosome 17 [46, 47]. Its wild-type form is activated by multiple cellular stresses and mediates cell-cycle arrest and cell death [48]. In CRC patients, its transcriptional activity is often repressed by missense mutations or chromosomal deletion at 17p [45, 46]. When TP53 is lost, CRC cells become even more resistant to apoptosis and augment proliferation [48].

Another critical alteration during the late stage of CRC progression is the acquisition of deregulated transforming growth factor-beta (TGF-β) signaling, for instance, by deletion of *SMAD4* or mutations in the transforming growth factor-beta receptor II (*TGFBR2*) gene [49, 50]. The frequency of these mutations is low. It only accounts for 10-15% of CRC patients with CIN. Hence, they are challenging to use for prognostic purposes [32, 51]. According to certain studies, there might exist a weak correlation between SMAD4 loss and poor overall survival [52, 53]. On the molecular level, deregulated TGF-β signaling promotes resistance to apoptosis and faster proliferation [54, 55]. Further details of this signaling pathway are described in the following chapters.

The MSI subtype is the second most common cause of sporadic CRC development, affecting 15 to 20% of patients [56, 57]. It is defined by the inactivation of DNA mismatch-repair (*MMR*) genes, which repair base-base mismatches in DNA. These defects can either be acquired by spontaneous events or be inherited. When it is inherited, it is called hereditary nonpolyposis colon cancer (HNPCC) or Lynch syndrome [28, 32]. HNPCC patients have an 80% lifetime risk of developing CRC. They show germline mutations, especially in the *MMR* genes, *MSH2* (Mut S homolog 2), *MSH6* (Mut S homolog 6), *MLH1* (Mut L homolog 1), and *PMS2* (postmitotic segregation 2) [58-62]. A second somatic event in the wild-type allele must occur because one wild-type allele is still sufficient to maintain a functional MMR system. In contrast, in patients with sporadic CRC and microsatellite instability, the MMR system is inactivated by epigenetic mechanisms. Most often, the 5' untranslated region of the *MLH1* gene is hypermethylated, leading to the inactivation of the MMR system [59, 63, 64]. Other common mutations in MSI patients are frameshift mutations in the *TGFBR2* gene. By inactivating it, tumor cells can escape the growth-suppressive effect of TGF-β [65, 66].

Lastly, CRC can be caused by the CIMP. CIMP tumors are mainly characterized by global genome hypermethylation, which inactivates tumor suppressor genes [67]. One example of this high degree of methylation is the tumor suppressor gene cyclin-dependent kinase inhibitor 2A (*CDKN2A*), which was detected in 40% of CRCs [68, 69]. Another example is the C-X-C motif chemokine ligand 12 (CXCL12), whose aberrant methylation promotes metastasis in CRC [70]. In addition, the aforementioned *MLH1* gene is a typical example of CpG island methylation [63, 64]. Therefore, it is challenging to define CIMP tumors clearly. They can be MSI or CIN [44, 71, 72].

1.3. Transforming growth factor-beta (TGF-β) signaling

The TGF-β signaling pathway is one of CRC's most commonly deregulated pathways. It controls cell-autonomous functions such as proliferation, differentiation, apoptosis, invasion, and the interaction between tumor cells and their surrounding microenvironment [73, 74].

Under normal physiological conditions, three different TGF-β ligands – TGF-β1, TGF-β2, and TGF-β3 - are binding to transforming growth factor-beta receptor I (TGFBR1) and TGFBR2 (Figure 5). However, TGFBR2 is the only specific receptor for binding TGF-β ligands and, therefore, essential for TGF-β signaling. When TGF-β binds to TGFBR1 and TGFBR2, a heterotetrameric active receptor complex is formed, resulting in the phosphorylation of TGFBR1 by TGFBR2 [75, 76]. TGFBR1 then phosphorylates and activates either SMAD2 and SMAD3 or SMAD1, SMAD5, and SMAD8, dependent on the cell type. These activated receptor-regulated Smads (R-Smads) form a heteromeric complex with SMAD4 and translocate into the nucleus. This complex associates with other DNA-binding transcription factors, co-activators, and co-suppressors to bind to the promoter region of TGF-β target genes. Thus, various proliferation, differentiation, apoptosis, and invasion genes are activated or repressed. The cellular response depends on the cell type [76, 77]. TGF-β signaling can also regulate non-Smad pathways such as p38, c-Jun N-terminal kinase (JNK), Rat sarcoma-Erk (Ras-Erk), PI3K-PKB, and different GTPases such as cell division control protein 42 homolog (CDC42) or Ras homolog family member A (RHOA). These non-Smad pathways also regulate cell-autonomous functions such as migration, invasion, or epithelial-to-mesenchymal transition (EMT) [78-80].

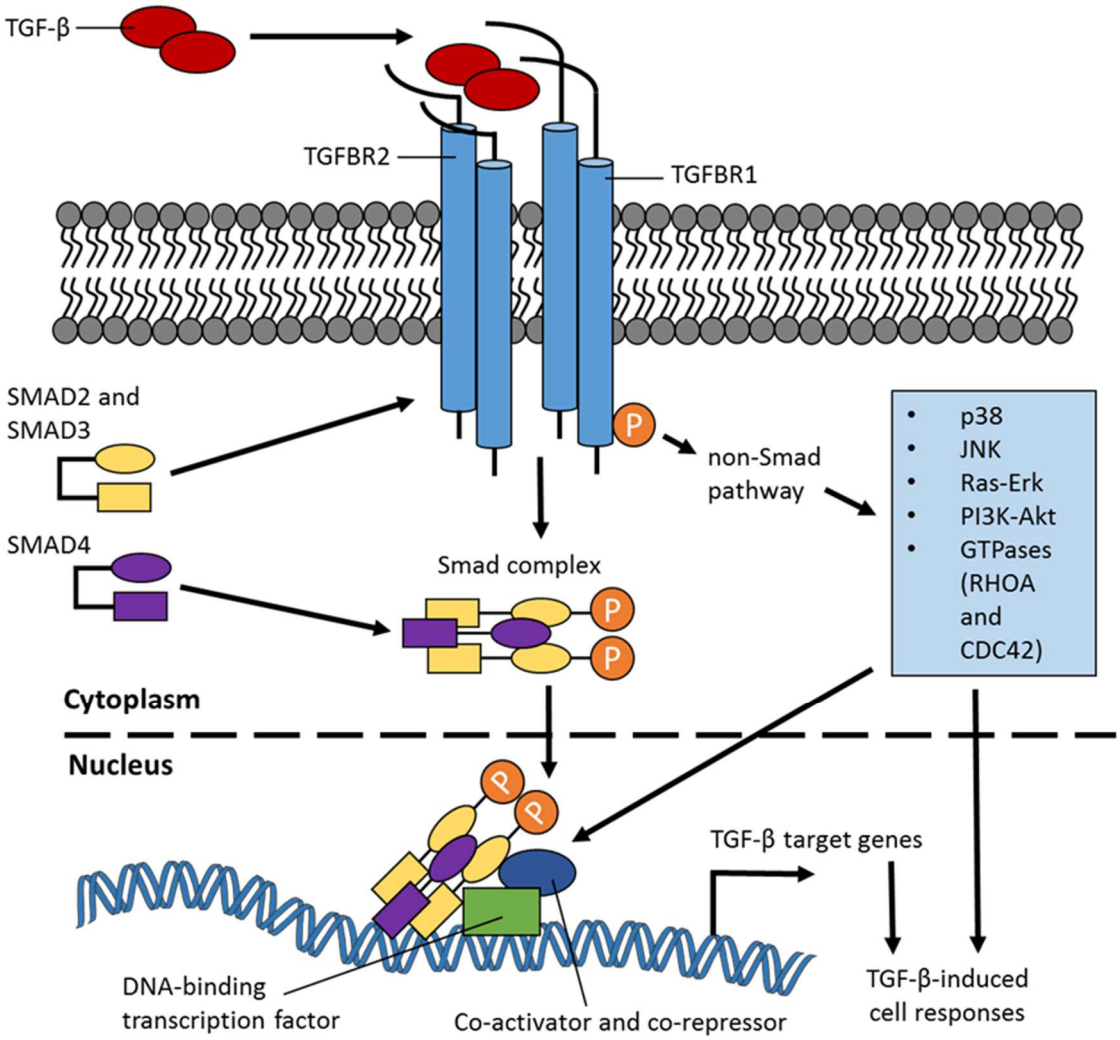

Figure 5: TGF-β signaling
TGF-β signaling can occur via both Smad and non-Smad pathways. First, the TGF-β ligand binds to TGFBR2 and TGFBR1, leading to the phosphorylation of TGFBR1 by TGFBR2. TGFBR1 then phosphorylates and activates SMAD2 and SMAD3, resulting in the formation of the Smad complex. This Smad complex, which includes SMAD2, SMAD3, and SMAD4, translocates into the nucleus and interacts with DNA-binding transcription factors, co-activators, and co-repressors. Thereby various TGF-β target genes, which mediate proliferation, differentiation, and apoptosis, are regulated. Furthermore, TGF-β signaling can activate other signaling pathways such as JNK, Ras-Erk, PI3K-Akt, p38, CDC42, or RHOA via non-Smad pathways [based on 77].

In CRC patients, the mechanism mentioned above cannot occur properly. As already described in chapter 1.2.3, CRC patients often suffer from *TGFBR2* mutations or deletion of *SMAD4*, resulting in poorer overall survival [49, 50, 52, 53]. In detail, mutation of *TGFBR2* prevents signaling to SMAD proteins, and loss of SMAD4 prevents the formation of the Smad complex, both necessary for transcription of TGF-β target genes. Once these TGF-β target genes cannot be repressed or activated, the cancer cells are equipped with tumor-promoting functions [73, 74]. For instance, cancer cells deficient in canonical TGF-β signaling can circumvent apoptosis induction. Usually, TGF-β induces pro-apoptotic target genes such as Bcl-2 interacting mediator of cell death (*BIM*), growth arrest, and DNA damage-inducible 45β (*GADD45β*), and death-associated protein kinase

(*DAPK*) [81-83]. When these signals are lost, tumor growth and survival are promoted. This was recently shown in a BIM-deficient follicular lymphoma mouse model [84]. Moreover, the induction of cell cycle arrest mediated by TGF-β can be prevented. Usually, c-MYC is bound to MIZ and thereby represses transcription of cyclin-dependent kinase inhibitor 2B (*CDKN2B*) (Figure 6). Under treatment with TGF-β, c-MYC is downregulated, and the Smad activator complex (Smad, SP1, MIZ) is formed. This complex recognizes the Smad-binding region (SBR) element of the DNA and activates *CDKN2B/p15* transcription. In cells with *SMAD* or *TGFBR* mutations, this mechanism is abrogated. The Smad activator complex cannot be formed; therefore, the repression of *p15* by c-MYC is not relieved, and cells can proliferate in the presence of TGF-β [85-88]. A similar mechanism was observed for the cyclin-dependent kinase inhibitor 1 (*CDKN1A/p21*) [89].

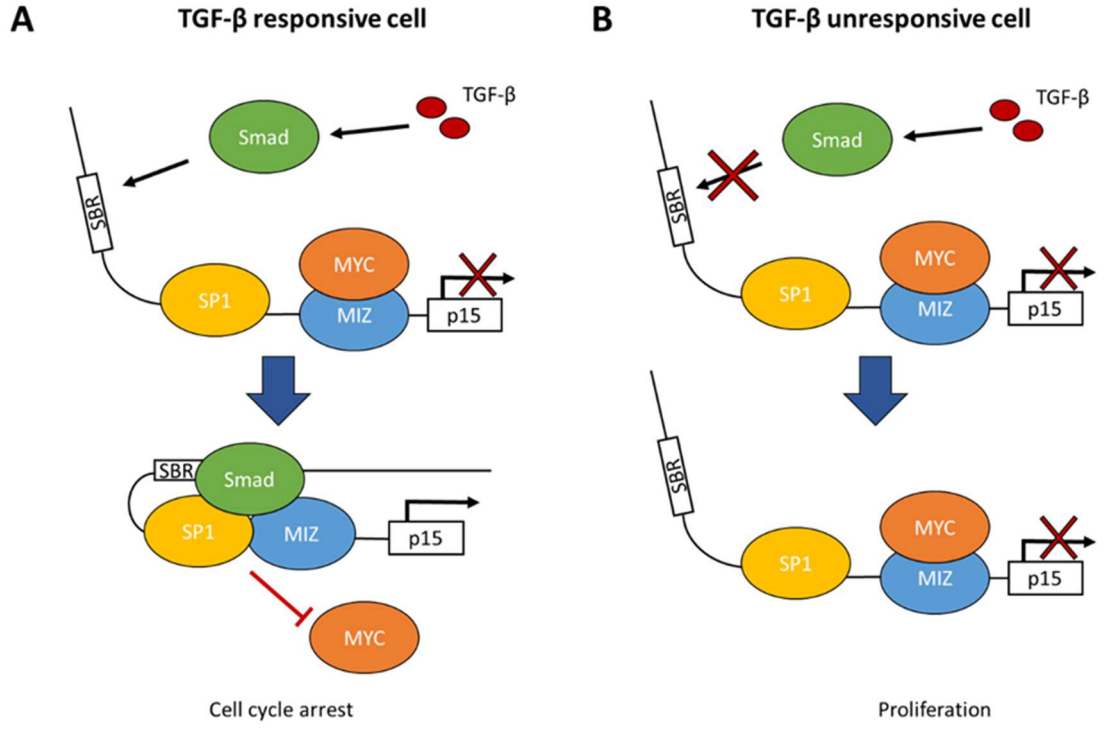

Figure 6: Model of *p15* induction in TGF-β responsive and TGF-β unresponsive cells
A) c-MYC is usually bound to MIZ and thereby represses transcription of *p15*. In response to TGF-β treatment, c-MYC is downregulated, and a Smad activator complex (Smad, SP1, MIZ) that recognizes the Smad-binding region (SBR) element is formed. Thereby transcription of *p15* is activated, and cells undergo cell cycle arrest. B) In TGF-β unresponsive cells (mutations in *SMAD4*, *TGFBR1*, *TGFBR2*), the Smad activator complex is not activated and thereby cannot overcome the repression of *p15* by c-MYC. Therefore, cells can still proliferate under TGF-ß treatment [based on 87, 88].

Furthermore, not only cell-autonomous functions are affected, but also interactions with the adjacent tumor microenvironment [73, 74]. For example, Tauriello *et al.* revealed that mutations in the *TGFBR2* gene led to the suppression of differentiation and activity of T cells, contributing to the immune evasion of tumors [90]. Loss of *Smad4* in the intestinal epithelium of mice treated with dextran sodium sulfate (DSS) revealed upregulation of

inflammation-related genes such as C-C motif chemokine ligand 20 (*Ccl20*) and alterations of the immune microenvironment [91]. Another study found that the absence of *Smad4* increased C-C motif chemokine ligand 9 (CCL9) levels, which attracted myeloid cells via the C-C chemokine receptor type 1 (CCR1). Thus, tumor immune invasion and metastasis were promoted [92, 93]. These are a few examples of how deregulated TGF-β signaling can promote cancer development. Further studies are required to address the molecular consequences of deregulated TGF-β signaling.

1.4. Cancer stem cells (CSC) in CRC

Cancer stem cells (CSCs) are cancer cells with stem-cell-like properties that can initiate tumor growth [94, 95]. It is a widely accepted model in the current research community.

In the past, it was assumed that adult stem cells/CSCs are rare, quiescent, and divide asymmetrically, producing one stem cell and one transit-amplifying (TA) cell [94, 95]. Recent studies contradict this hypothesis. They demonstrated that adult stem cells/CSCs are not necessarily rare and dormant and that niche signals control the fate of daughter cells [95-100]. Depending on the available niche space, adult stem cells/CSCs "[…] can give rise to one, two, or no daughter stem cells […]" [95, 99, 101-105]. If this "niche has […] space for four stem cells, [the] stem cell progeny [will] compete to occupy [this] space" [95, 99, 101-105]. This model, called "neutral competition", was already confirmed in different tissues such as the intestine, epidermis, or stomach [95, 99, 101-105]. Interestingly, fully differentiated daughter cells can re-enter the niche and de-differentiate. By doing so, they can replace lost stem cells [100, 106-108].

The mechanism mentioned above is also observed in CRC. First, a differentiated cell at the top of the crypt is transformed and de-differentiates into a stem-cell-like state. Then CRC stem cells (CCSCs) are generated, spreading the crypt downwards. This spreading from the top to the bottom of the crypt is also called the "Top-down" model [109, 110].

CCSCs can be characterized by their expression of various stem cell markers. In particular, LGR5 and epithelial cell adhesion molecule (EpCAM) are expressed in CRC [94, 111]. These two markers are further described below.

LGR5 is a class A G-protein coupled orphan receptor and a member of the Wnt signaling pathway [112, 113]. It modulates the strength of canonical Wnt signaling by binding to its ligand R-spondin, promoting proliferation and self-renewal [114-116]. Different studies showed that LGR5 is essential for tumor growth and metastasis [94, 106, 116-121]. For example, LGR5 modulated cell mobility, epithelial-mesenchymal transition, and tumor formation in breast cancer [116]. In CRC, LGR5 was found to correlate with Wnt signaling. When the expression of LGR5 was low, WNT signaling was downregulated, leading to reduced tumor formation and Paneth cell differentiation [94,

113, 118-120]. “Lineage tracing [experiments] of primary human CRC-derived organoid cells [revealed] tumor-initiating cell (TIC) activity of $LGR5^+$ cells in serial transplantation” [121, 122]. Furthermore, a population of not actively proliferating $LGR5^+$ cells remained quiescent for prolonged times [121, 122]. In the same year, two other studies strengthen the importance of LGR5 in CRC development [106, 117]. Shimokawa *et al.* demonstrated that the deletion of $LGR5^+$ cells in already established tumors *in vivo* led to the re-expression of LGR5 in differentiated tumor cells. Subsequently, these tumor cells de-differentiated and promoted tumor re-growth [106]. De Sousa e Melo *et al.* discovered that $LGR5^+$ CSCs were required for the formation and maintenance of colon-cancer-derived liver metastasis [117]. LGR5 can also be used to isolate CCSCs [123, 124].

EpCAM is a transmembrane glycoprotein with various functions. These include Ca^{2+}-independent homotypic cell-cell adhesion in the epithelia, proliferation, cell signaling, metastasis, differentiation, migration, and tumorigenesis [111, 125-128]. For example, EpCAM promoted bone metastasis formation in breast cancer *in vivo* [129]. In CRC, the membrane-truncated form of EpCAM ($EpCAM^{MT}$) correlated with more aggressive clinical behavior and shorter survival in patients [130]. Furthermore, Maetzel *et al.* observed the regulation of Wnt target genes such as *c-myc* and *cyclin A/E* by EpCAM [126].

These are just a few examples of how CSCs can be characterized. Other stem cell markers are available. With a further understanding of CSCs and their mechanisms leading to tumor heterogeneity and therapy resistance, novel CSC-directed therapy options might become available [94, 95].

1.5. Ribosome biogenesis in cancer

Ribosome biogenesis describes a strictly regulated and energy-consuming process to generate ribosomes, which are essential for translating messenger ribonucleic acids (mRNAs) into proteins. Thus, they contribute to cell growth and survival. These ribosomes are complexes of ribosomal ribonucleic acids (rRNAs), ribosomal- and ribosome-associated proteins [131-133].

In eukaryotic cells, ribosomes comprise the large 60S subunit and the small 40S subunit. The 60S subunit comprises 47 ribosomal proteins and the 28S, 5.8S, and 5S rRNAs. The smaller 40S subunit contains 33 ribosomal proteins and one 18S rRNA [131-133].

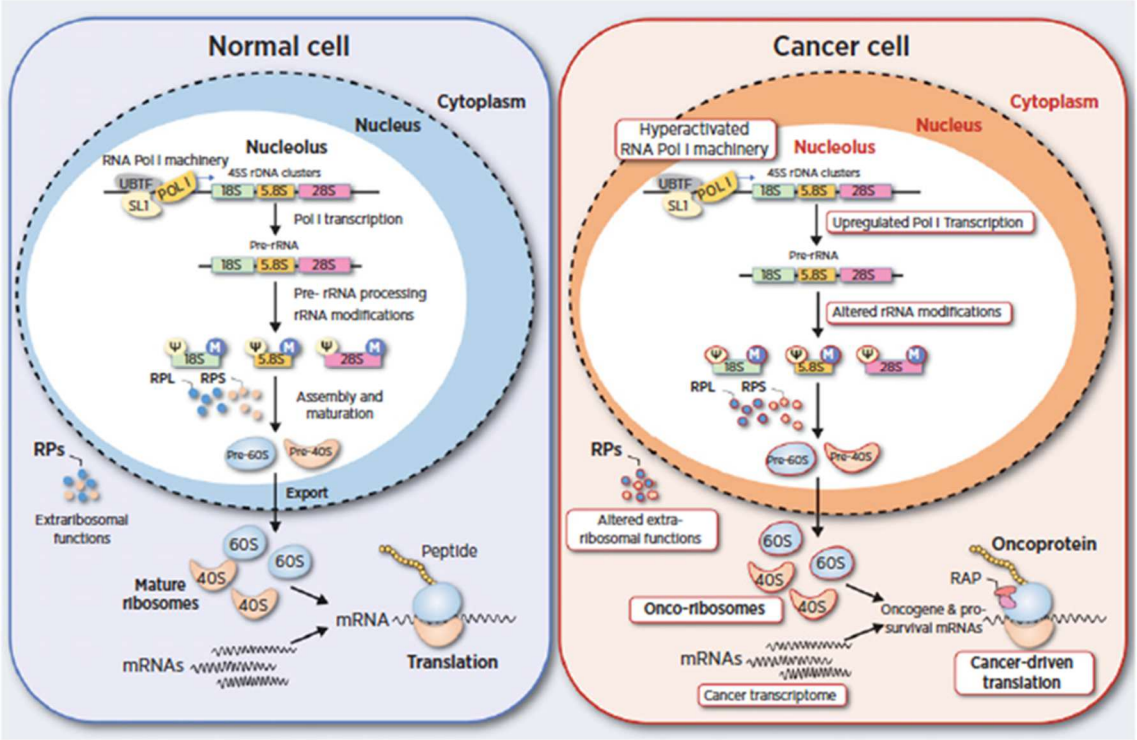

Figure 7: Ribosome biogenesis in normal and cancer cells

Ribosome biogenesis begins with RNA Pol I transcription factors (e.g., SL1, UBTF) binding to active clusters of rDNAs. This leads to the initiation of RNA Pol 1 transcription and pre-rRNA biosynthesis. Next, pre-rRNAs are processed, and rRNAs are further modified. Ribosomal proteins are combined with the previously processed rRNA species to generate the pre-60S and the pre-40S subunits. After maturation, the 60s and 40S subunits are transported into the cytoplasm to act in protein synthesis. The mature ribosomal proteins can also undergo posttranslational modifications, contributing to ribosome heterogeneity. In cancer cells, an upregulation of RNA Pol I increases rRNA biogenesis and satisfies their high demand for ribosomes. Furthermore, other noncanonical/abnormal rRNA modifications and altered extra-ribosomal functions are occurring. This then leads to chemo/radioresistance and cancer progression. Such ribosomes are called "onco-ribosomes" and promote a cancer-driven translation program [obtained from 133]. Reuse of figure was allowed by AACR (license number: 5520850427477).

The maturation of ribosomes begins in the nucleolus (Figure 7). First, upstream binding transcription factor (UBTF) and selective factor 1 (SL1) bind to active clusters of ribosomal DNAs (rDNAs), which reside in the nucleolus in nucleolar organizer regions (NORs). This leads to the initiation of RNA polymerase I (RNA Pol I) transcription. The rDNA is transcribed into pre-ribosomal RNA (47S pre-rRNA), and the 47S pre-rRNA is cleaved and modified to form 18S, 5.8S, and 28S rRNA. For that, the three rRNAs interact with small nuclear ribonucleoproteins (snoRNPs) and various protein-processing factors. Interestingly, the transcription of 28S and 5.8S rRNAs is mediated by RNA Polymerase II (RNA Pol II), whereas 5S rRNA and transfer RNAs (tRNAs) are transcribed by RNA Polymerase III (RNA Pol III). Before export into the cytoplasm, the large 60S subunit is generated by assembling 5.8S, 28S, and 5S rRNAs with L ribosomal proteins (RPLs), and the small 40S subunit by assembling the 18S rRNA and S ribosomal proteins (RPSs). After export into the cytoplasm, the 40S and 60S subunits form the mature 80S ribosome complex, which is necessary for successful translation [131-133].

During the maturation of the large ribosomal subunit, one essential protein complex involved is the PeBoW complex. In humans, it is composed of pescadillo ribosomal biogenesis factor 1 (PES1), block of proliferation 1 (BOP1), and WD repeat domain 12 (WDR12); in yeast, they are called Nop7, Erb1, and Ytm1. Knockdown of any of these proteins resulted in blockage of pre-RNA processing [134-136]. Interestingly, its localization is restricted to the nucleolus, indicating that it must be released before transporting out of the nucleolus [135, 137, 138]. Indeed, the release from preribosomal particles is mediated by three different AAA-ATPases, Rea1/midasin, Rix7, and Drg1/Afg2 [139]. For example, Rea1 mediates the removal of Rsa4/Notchless homolog 1 (NLE1) and the Rix1 sub-complex by physically contacting these two factors and thereby promoting nuclear maturation and export to the pre-60S subunit [136, 140, 141]. When this interaction is disturbed by mutations, the 60S subunit export is defective; therefore, the ratio of 60S/40S mature ribosomal particles is out of balance. This leads to the development of "half-mer" polysomes in the cytoplasm [140]. Therefore, it represents a significant step during ribosome biogenesis.

In cancer cells, ribosome biogenesis is dysregulated [131-133]. For example, cancer cells can regulate Pol I activity to enhance rDNA transcription. Various oncogenic pathways are responsible for this. When PI3K and PKB are activated, c-MYC and mammalian target of rapamycin (mTOR) signaling are elicited. c-MYC then interacts with rDNA loci and recruits SL1, which triggers Pol I transcription [142-144]. Furthermore, c-MYC can enhance the synthesis of 5S rRNA via activation of the Pol III transcription factor TFIIIB [145, 146]. Nevertheless, not only c-MYC can promote rDNA transcription but also other proteins. When RAS-MAPK (mitogen-activated protein kinase) gets activated, UBTF and transcription initiation factor IA (TIF-IA) are phosphorylated, which then boosts rDNA transcription [147, 148]. The RNA Pol I activity can also be negatively regulated by tumor suppressor genes [132, 149]. TP53 is often lost in human cancer [150, 151]. If TP53 cannot stop RNA Pol I activity by hindering the pre-initiation complex (PIC) assembly at the rDNA gene promoter, transcription of RNA Pol I-driven genes becomes accelerated. In addition, TP53 can directly bind to TFIIIB and thereby repress RNA Pol III activity [152-154]. Other tumor suppressor proteins that control ribosomal biogenesis include phosphatase and tensin homolog (PTEN), CDKN2A, and retinoblastoma protein (RB) [155-157].

Besides upregulating RNA Pol I transcription, cancer cells can also stimulate ribosome biogenesis by altering rRNA modification [131, 133]. For instance, cancer cells acquire distance methylation patterns of their rRNAs under stress. This leads to the formation of specialized ribosomes that perform internal ribosome entry site (IRES)-mediated translation [158]. Furthermore, rRNAs are posttranscriptionally modified via pseudouridylation (Ω) or ribose 2'-O methylation (2'-O-Me) [159-161]. These modifications are mediated by box H/ACA and box C/D ribonucleoprotein complexes

[162, 163]. In breast cancer patients, Marcel *et al.* observed that the rRNA ribose 2'-O methylation is altered and correlated with subtype and tumor grade [164]. Another example of how rRNA modifications are altered is by TP53. TP53 directly regulates fibrillarin (FBL), an rRNA methyl transferase. If TP53 is lost or mutated, the uncontrolled FBL activity leads to altered 2'-O-Me on ribosomes and induction of IRES-dependent translation [165].

Furthermore, not only modifications to the processes of ribosome biogenesis are occurring, but also mutations in the ribosomal proteins, the so-called "onco-ribosomes". These specialized ribosomes preferentially translate oncogenic and pro-survival genes, promoting cancer progression [131, 133]. One example of this phenomenon was shown in chronic lymphocytic leukemia (CLL) and involves the *RPS15* gene. There, mutations in the *RPS15* gene led to ribosome defects and disturbed global protein synthesis [166].

In summary, ribosome biogenesis is required by both normal and cancer cells and is frequently dysregulated during cancer progression. To what extent these malignant alterations in ribosome biogenesis can be used for therapeutic targeting remains elusive.

1.6. Modeling of colorectal cancer (CRC) *in vivo*

Modeling CRC *in vivo* is still the gold-standard approach for understanding disease progression and developing new therapeutic options for patients. These models should recapitulate the different stages of CRC, ideally with metastasis, and reflect the inter-individual molecular diversity in patients. In addition, they should be timesaving, low-priced, and mammalian [167, 168].

The most commonly used organism to model CRC is *Mus musculus*, also called the mouse [168-170]. Its intestine is similar to that of humans in terms of development, structure, and functions [171, 172]. They are also low-priced and timesaving [173]. Although their cecum is relatively big relative to their complete gastrointestinal tract when compared to humans, rats are sometimes used. This is due to the high fiber content of their diet. Moreover, compared to humans, both models are missing adipose tissue in the submucosa [172, 174]. Still, they are the most accepted models for modeling CRC *in vivo* [175].

There are four different groups of CRC mouse models available. They can be divided into spontaneous, carcinogen-induced, genetically engineered, and transplantation models and are further described in the following paragraphs [167, 168].

Spontaneous models of CRC are not abundant due to their low reproducibility and unpredictability [175]. The incidence accounts for only 6-7% of C57BL/6J mice spontaneously developing cancer in the large intestine during their lifetime, but there was also one example with higher incidence. In 1989, a particular rat strain, called Wistar-

Furth/Osaka, was published, which developed adenocarcinomas spontaneously with an incidence of 30-40%. However, many of these tumors regress spontaneously [176, 177]. Therefore, other, more genetically defined, and controllable tumor models are necessary.

One possibility to generate tumor formation in a controlled way is by administration of chemical carcinogens, also called carcinogen-induced models. This can either be performed directly or indirectly. When the liver has to convert the carcinogen into its active form, it is called an indirect carcinogen; for example, 3,2'-dimethyl-4-aminobiphenyl (DMAB), 2-amino-1-methyl-6-phenylimidazo (4,5-b) pyridine (PhIP), 1,2-dimethylhydrazine (DMH), and azoxymethane (AOM). In contrast, the direct carcinogen induces cancer without being metabolized; for example, N-methyl-N-nitrosourea (MNU) and N-methyl-N-nitrosoguanidine (MNNG) [167, 168].

Among the carcinogens mentioned above, AOM is the most commonly used. In 1970, it was shown that AOM induces intestinal tumors in mice. Later, other studies confirmed its carcinogenic effect by provoking the same phenotype in rats [178, 179]. In detail, AOM is activated by N-oxidation through cytochrome P450 2E1, resulting in methylazoxymethanol and methyl-diazoxide, which promotes inflammation [180]. After 30 weeks, mice develop tumors in the small intestine and colon [181]. Histochemical analysis revealed strong similarities to human tumors, and even metastasis in liver and lymph nodes could be observed [182, 183].

In contrast, MNU and MNNG induce CRC via a different mode of action [184, 185]. They are direct DNA alkylating agents and transfer methyl groups to nucleobases, which provokes genetic mutations [168, 186]. These mutations lead to cancer development after 18 weeks. One advantage of this model is the selective induction in the distal colon and rectum because the carcinogen is only administered there. These models were one of the first inducible CRC models *in vivo* but are not so common anymore due to the uncontrolled molecular downstream effects [168, 184, 185].

To investigate the exact role of genetic events happening during CRC progression, genetically engineered mouse models (GEMM) are often used. The first GEMM of CRC was the APC^{Min} (Min, multiple intestinal neoplasia) mouse model. Originally, N-ethyl-N-nitrosourea was applied to mice, which led to nonsense mutations in the *Apc* gene. When breeding these mice, the first model for intestinal neoplasia was established [187]. After 120-140 days, they develop many adenomas in the small intestine and die from intestinal obstruction and anemia [187]. This model is mainly used to investigate familial adenomatous polyposis (FAP) syndrome because patients harbor the same *APC* mutations [188-190]. It is inappropriate to investigate sporadic CRC due to missing progression into carcinomas and metastasis [190]. Later, with the invention of the Cre-LoxP (Causes recombination-locus of X-over P1) system, these *Apc* mutations were combined with various other gene mutations [191-194]. The Cre-LoxP system is used to

perform insertions, deletions, inversions, and insertions at a specific DNA sequence in cells. It is based on the Cre recombinase, which recombines short target sequences called LoxP sites. The DNA is rearranged depending on the orientation and location of the loxP sites, resulting in the mutations indicated before [191, 192]. For example, when mutations in the *Kras* gene were introduced via Cre/LoxP system, tumor formation in the APC^{Min} mouse model was accelerated [193]. Also, when combining the *Apc* mutation with a dominant-negative *Tp53* mutation or *Smad4* mutation, an increase in malignancy and accelerated tumor growth of intestinal tumors could be observed [194-197]. Nowadays, there are even models containing all relevant compound mutations, showing that combined mutations in *APC*, *KRAS*, *TP53,* and *SMAD4* result in the worst survival. By doing so, CRC patients' genetic causes can be nicely reflected [55, 194]. These are just a few examples of how CRC can be genetically modeled, contributing enormously to understanding CRC initiation and progression underlying different molecular pathways.

The last possibility to investigate CRC *in vivo* is the transplantation model. Transplantation models are very diverse; they can either be syngeneic or xenogeneic. It is called syngeneic when the tumor tissue or cancer cell line is transplanted into the same mouse strain. In contrast, xenogeneic transplantations are defined as transplantations between different strains or species; for example, human cancer cells into immunodeficient mice. In the case of CRC, transplantations are also distinguished based on their application site. It is called orthotopic if cancer cells are applied into the cecum or rectum, and heterotopic if cancer cells are injected into the tail vein, spleen, or under the skin or renal capsule [167, 168].

One of the earliest transplantation models was subcutaneous injections into the mouse flank, also classified as a heterotopic tumor model. This tumor model can quickly be learned and allows tumor growth monitoring by eye [167, 198, 199]. Therefore, it can easily be scaled to perform high throughput sampling [200, 201]. In contrast, a significant disadvantage of this tumor model is the missing intratumor-heterogeneity and adequate tumor microenvironment because only a homogenous cell suspension is applied [167, 202]. In addition, other heterotopic application sites, such as intravenous or under the renal capsule, are not feasible when investigating CRC. The high vascularization in the renal capsule might promote the engraftment of cancer cells, but an adequate tumor microenvironment is also missing. Moreover, the injection under the renal capsule is complicated and requires many practical efforts [203, 204]. A significant limitation must be considered when injecting CRC cells intravenously or intrasplenic. The cancer cells circumvent crucial steps of metastasis (e.g., degradation of extracellular matrix (ECM), vascular invasion), thereby not reflecting disease progression observed in CRC patients. Thus, heterotopic tumor models are inappropriate for investigating CRC *in vivo* [167, 168].

Another transplantation model is the Patient-derived Xenograft (PDX) model. Tumor pieces from surgical resections or biopsies are transplanted into the flanks of immunodeficient mice [205]. The advantage here is that the heterogeneity of CRC patients is better reflected. Each donor is different [206]. Furthermore, the histology of transplanted PDX is similar to the original 'donor' [207, 208]. Compared to the previously mentioned heterotopic mouse model, the PDX model also contains stromal cells [209, 210]. Therefore the architecture of the tumor remains intact [211]. With these features, PDX models are often used for drug response studies [212, 213]. For example, it was shown that combined inhibition of EGFR and HER2 induces long-term tumor regression in metastatic CRC patient samples [212]. In contrast, the disadvantages of this tumor model are that testing of immunotherapy approaches is impossible due to the missing immune system, and the establishment of this tumor model is time-consuming [167, 205]. Engraftment is also not guaranteed. Sometimes multiple attempts are necessary [206, 214, 215]. Another problem of PDX models is the development of lymphomas at the implantation site [216]. Hence, PDX models are marvelous for predicting the patient's drug response to therapy, thereby contributing to developing personalized medicine in CRC.

Researchers established orthotopic models to overcome the limitations of the tumor models mentioned above. The first orthotopic transplantations were performed in the 1980s. For example, human colon cancer cells were injected into the cecal wall of young athymic nude mice, resulting in cancer growth [217]. Researchers could also observe lymph node and liver metastasis a few years later in these experimental approaches [218]. Recently, Cañellas-Socias *et al.* innovated this model to investigate metastatic recurrence. Cancer cells were injected into the caecum's tip, and the primary tumor was removed after a specific time. Interestingly, primary tumor resection shortly after implantation resulted in disease-free survival of mice, whereas removal after 4-5 weeks resulted in a metastatic relapse in the liver. The significant advantage of this model is that mice have more time to develop metastasis without dying due to the primary tumor [219]. However, this model also has some limitations. For example, it requires profound mouse surgical knowledge and experience. Usually, the abdomen is opened, and the cecum and ascending colon are pulled out. Next, the colon cancer cells are injected into the cecum wall. Finally, the cecum with the ascending colon is placed back into the abdomen, and the wound is closed with sutures [217, 218, 220]. The problem with this procedure is that it can cause inflammation and morbidity, and the abdominal cavity can be contaminated with cancer cells. Moreover, it is not a genuine orthotopic model because the tumor arises from the mucosa [167, 221]. Still, it is one of the most frequently applied models in the research community.

The orthotopic model has even further evolved to a less invasive method without surgery. In detail, the scope of a mouse endoscope is inserted into the mouse colon, and a needle

is inserted through the working channel to the scope's front (Figure 8). When the right application site is determined, the cancer cells are delivered by gently penetrating the mucosal epithelial layer. Usually, 50-100 ul volume is applied. Here, it is critical to observe if a bubble is formed which stays for some seconds. After a successful injection, the endoscope is pulled out, and the mice can wake up again. This procedure is a gentle way to generate metastatic CRC *in vivo* [222-224]. It is often used to investigate the effect of defined genetic events during the progression of CRC. For example, transplantation of human intestinal tumor organoids harboring different combinations of the adenoma-carcinoma sequence revealed a similar phenotype as observed in patients. In addition, the transplanted cancer cells can grow in an adequate microenvironment and even in combination with a functional immune system [55, 222, 223]. However, this technique is challenging and always requires two experimenters. One person has to navigate the colonoscopy, and the other has to inject the cancer cells into the mucosal wall [222, 224]. In summary, regarding clinical relevance and animal welfare, the endoscopy-guided orthotopic model is among the best CRC *in vivo* models today.

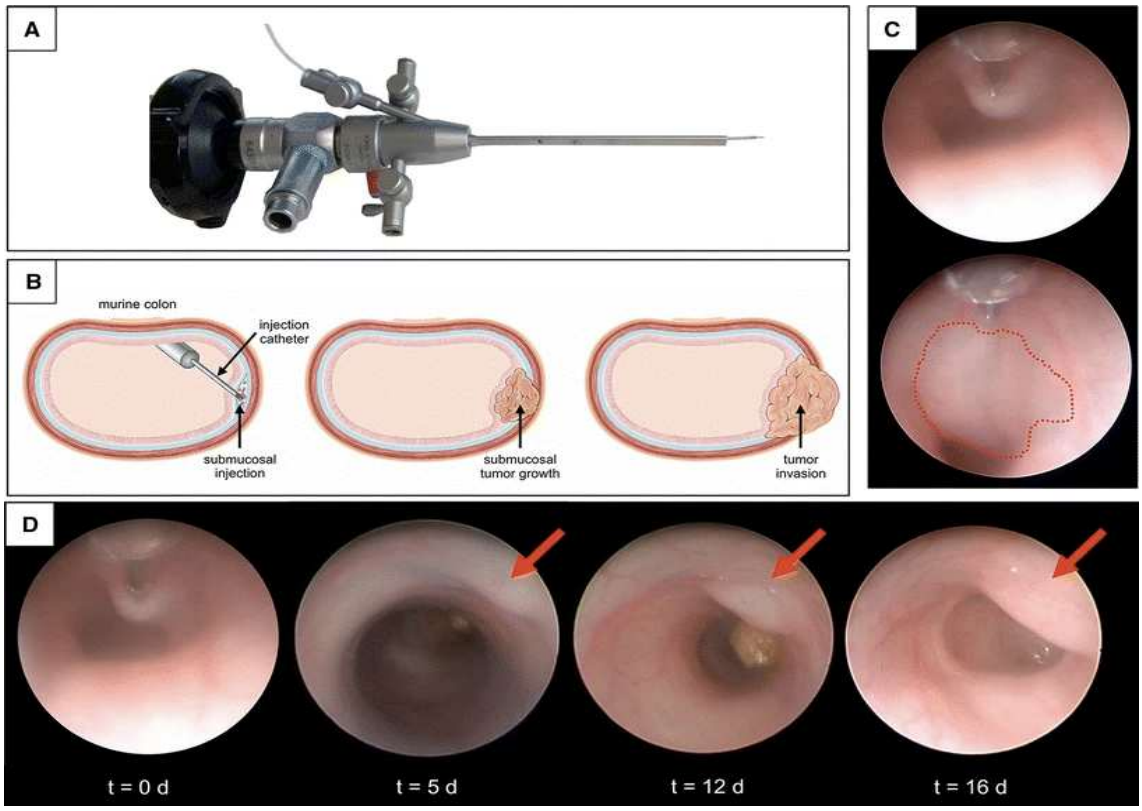

Figure 8: Endoscopy-guided orthotopic transplantation model of CRC
A) Image of the endoscope with the injection needle introduced via the working channel. B) Schematic representation of the endoscopy-guided orthotropic transplantation model. Cancer cells are injected submucosal into the mouse colon and then grow into an invasive tumor, which can protrude into the lumen. C) Red dotted line shows mucosal lifting after successful transplantation. D) Monitoring of tumor growth after successful transplantation. Follow-up was performed for 16 days [adapted from 225]. The reuse of figures was allowed by Springer Nature (license number: 5520850709423).

2. Aims

CRC patients often suffer from loss of functional TGF-β signaling, either by deletion of *SMAD4* or mutations in the *TGFBR2* gene. These mutations correlate with a poorer outcome of the disease. Hence, the first aim of this study was to investigate how the gene expression profile changes when CRC cells acquire a *SMAD4* deletion and are exposed to a TGF-β rich environment, as is usually the case in advanced CRC.

The second aim was to identify which deregulated genes in SMAD4-deficient Patient-derived tumor organoids (PDTOs) might confer an advantage for tumor cell fitness. To this end, clustered regularly interspaced short palindromic repeats/CRISPR-associated protein 9 (CRISPR/Cas9)-mediated genome editing of the target gene should be performed, and knockout cells should be analyzed concerning their functional relevance and downstream effects *in vitro*. Also, its functional relevance *in vivo* should be investigated. To that end, an endoscopy-guided transplantation mouse model should be established. Lastly, the upstream regulation of the target gene and the existence of a therapeutic window in CRC should be explored.

3. Materials

3.1. Laboratory equipment

Device	Supplier
AxioPlan 2 Microscope System	Carl Zeiss, Oberkochen, Germany
Agilent BioAnalyzer 2100	Agilent Technologies, Santa Clara, CA, USA
Berthold Orion II Microplate Luminometer	Titertek-Berthold, Pforzheim, Germany
Binder Incubator	Binder, Tuttlingen, Germany
BD Accuri™ C6 Flow Cytometer	BD Biosciences, San Jose, CA, USA
MACSQuant® X Flow Cytometer	Miltenyi Biotec, Bergisch Gladbach, Germany
Endoscope, 1.9 mm diameter, with linear Hopkins lens optics (ColoView System)	Karl Storz SE&Co.KG, Tuttlingen, Germany
Needle, custom-made, flexible, fine, 33-gauge, custom length of 16 inches, custom point style of 4 at 45°	Hamilton, Reno, NV, USA
GeneAmp® PCR System 9700	Applied Biosystems, Foster City, CA, USA
Hareus Megafuge 1.0R	ThermoFisher Scientific, Waltham, MA, USA
HTU Soni130 Sonicator	G. Heinemann, Schwäbisch Gmünd, Germany
Li-COR Odyssey Fc	Li-COR, Lincoln, NE, USA
Lightcycler® 480	Roche, Penzberg, Germany
LSM 700 Laser Scanning Confocal Microscope	Carl Zeiss, Oberkochen, Germany
Mini Trans-Blot™ Cell	Bio-Rad Laboratories, Munich, Germany

Mini-PROTEAN Tetra Vertical Electrophoresis Cell	Bio-Rad Laboratories, Munich, Germany
AZ100 Multizoom Microscope	Nikon, Amsterdam, Netherlands
Mr.Frosty™ Freezing Container	ThermoFisher Scientific, Waltham, MA, USA
ND 1000 NanoDrop Spectrophotometer	NanoDrop Products, Wilmington, DE, USA
NEPA21 Electroporator	Nepa Gene, Chiba, Japan
Neubauer Counting Chamber	Carl Roth, Karlsruhe, Germany
Nikon D5100 reflex camera	Nikon, Amsterdam, Netherlands
Qubit 3.0 Fluorometer	ThermoFisher Scientific, Waltham, MA, USA
T100™ Thermal Cycler	Bio-Rad Laboratories, Munich, Germany
Varioskan™ Multimode Microplate Reader	ThermoFisher Scientific, Waltham, MA, USA
VectraPolaris™ Automated Quantitative Pathology Imaging System	Akoya Biosciences, MA, USA
Ventana Benchmark	Ventana Medical System, Oro Valley, AZ, USA
xCELLigence Real-Time Cell Analyzer (RTCA)	Agilent Technologies, Santa Clara, CA, USA
HiSeq 2000 v4	Illumina, San Diego, CA, USA
Zeiss Stemi 2000-C Zoom Stereomicroscope with CL6000 LED illumination	Carl Zeiss, Oberkochen, Germany
Zeiss AxioCam ERc 5s	Carl Zeiss, Oberkochen, Germany

3.2. Chemicals and reagents

Application	Chemical compound	Supplier
Cell culture	Accutase	Sigma, Darmstadt, Germany
	Antibiotic-Antimycotic, 100x	Invitrogen, Karlsruhe, Germany
	Cell Recovery Solution	Corning, New York, NY, USA
	Collegenase IV	Biochrom AG, Berlin, Germany
	Cycloheximide (CHX)	Sigma, Darmstadt, Germany
	Chloroquine diphosphate salt	Sigma, Darmstadt, Germany
	Dimethylsulfoxide (DMSO)	Sigma, Darmstedt, Germany
	4',6-diamidino-2-phenylindole (DAPI)	Sigma, Darmstadt, Germany
	Dispase II	Stem Cell Technologies, Vancouver, BC, Canada
	Dithiothreitol (DTT)	Sigma, Darmstadt, Germany
	Doxycycline hydrochloride	Sigma, Darmstadt, Germany
	Dulbecco's phosphate-buffered saline (PBS)	Invitrogen, Karlsruhe, Germany
	Ethylenediaminetetraacetic acid (EDTA) disodium salt dihydrate	VWR International, Radnor, PA, USA
	FuGENE® HD transfection reagent	Promega, Madison, USA
	Lenti-X Concentrator	Takara, Kusatsu, Japan
	Lipofectamine LTX	Invitrogen, Karlsruhe, Germany
	Low melting Seaplaque™ Agarose	Lonza, Basel, Switzerland
	Matrigel® Basement Membrane Matrix, phenol red-free	Corning, New York, NY, USA
	Nutlin-3	TOCRIS, Avonmouth, Bristol, UK
	Opti-MEM™ Reduced Serum Medium	Invitrogen, Karlsruhe, Germany
	Polybrene	Sigma, Darmstadt, Germany
	Puromycin	Sigma, Darmstadt, Germany
	Polyethylenimine (PEI)	Sigma, Darmstadt, Germany

	Sodium chloride	Sigma, Darmstadt, Germany
	Triton X-100	AppliChem, Darmstadt, Germany
	TrypLE™ Select Enzyme	Invitrogen, Karlsruhe, Germany
	Trypsin-EDTA, 0.05 %	Invitrogen, Karlsruhe, Germany
Western blotting	Ammonium persulfate	AppliChem, Darmstadt, Germany
	Bromophenol blue	Th.Geyer, Renningen, Germany
	Bovine serum albumin (BSA)	Sigma, Darmstadt, Germany
	DTT	Sigma, Darmstadt, Germany
	Glycerol	Th. Geyer, Renningen, Germany
	Glycine	Sigma, Darmstadt, Germany
	Immobilon Western horseradish peroxidase (HRP) Substrate	Merck, Darmstadt, Germany
	Immobilon-P Polyvinylidene fluoride (PVDF), 0.45µm membrane	Merck, Darmstadt, Germany
	Methanol	Carl Roth, Karlsruhe, Germany
	PageRuler™ Prestained Protein Ladder	Invitrogen, Karlsruhe, Germany
	Phosphatase inhibitor cocktail 2	Sigma, Darmstadt, Germany
	Phosphatase inhibitor cocktail 3	Sigma, Darmstadt, Germany
	Polysorbate 20 (Tween20)	Th. Geyer, Renningen, Germany
	Radioimmunoprecipitation (RIPA) buffer, including protease inhibitor cocktail, phenylmethylsulfonyl fluoride (PMSF), sodium metavanadate (NaVO3)	Sigma, Darmstadt, Germany
	Sodium dodecyl sulfate (SDS)	Carl Roth, Karlsruhe, Germany
	Skim milk powder	Sigma, Darmstadt, Germany
	Sodium chloride (NaCl)	Sigma, Darmstadt, Germany
	SuperSignal™ West Femto Maximum Sensitivity Substrate	Thermo Scientific, Waltham, MA, USA

	Tetramethylethylenediamine (TEMED)	Carl Roth, Karlsruhe, Germany
	2-Amino-2-(hydroxymethyl)-1,3-propanediol (Tris)	Sigma, Darmstadt, Germany
	Tris-Bis Acrylamide (30 %)	Carl Roth, Karlsruhe, Germany
Cloning	Ampicillin sodium salt	AppliChem, Darmstadt, Germany
	Luria-Bertani agar (LB agar, powder mix)	Carl Roth, Karlsruhe, Germany
	Luria-Bertani medium (LB medium, powder mix)	Carl Roth, Karlsruhe, Germany
Immunohisto-chemistry	3,3`-diaminobenzidine (DAB, K3468)	Agilent Technologies, Santa Clara, CA, USA
	Hematoxylin Gill´s Formula (H-3401)	Vector Laboratories, Burlingame, CA, USA
	Target Retrieval Solution Citrate pH 6	Agilent Technologies, Santa Clara, CA, USA
Other	Paraformaldehyde (PFA, 4%)	Santa Cruz Biotechnology, Dallas, TX, USA
	Crystal Violet	Sigma, Darmstadt, Germany
	Formaldehyde solution (37%)	Sigma, Darmstadt, Germany
	Methanol	Carl Roth, Karlsruhe, Germany
	Acetic acid	ThermoFisher Scientific, Waltham, MA, USA
	Hank´s-balanced salt solution (HBSS)	ThermoFisher Scientific, Waltham, MA, USA
	ProLong Gold antifade DAPI mounting medium	Cell Signaling Technology, Danvers, MA, USA
	Agarose, universal	VWR International, Radnor, PA, USA

3.3. Cell Culture media

3.3.1. SW620, HT29 and HEK293 cell culture medium

Component	Concentration	Supplier
Dulbecco's modified eagle medium (DMEM) High Glucose, GlutaMAX		Invitrogen, Karlsruhe, Germany
Fetal bovine serum (FBS)	10 %	Invitrogen, Karlsruhe, Germany
Penicillin-Streptomycin	100 U/mL	Invitrogen, Karlsruhe, Germany

3.3.2. HCT116 cell culture medium

Component	Concentration	Supplier
McCoy's 5A medium		Sigma, Darmstadt, Germany
Fetal bovine serum (FBS)	10 %	Invitrogen, Karlsruhe, Germany
Penicillin-Streptomycin	100 U/mL	Invitrogen, Karlsruhe, Germany

3.3.3. HCEC-1CT cell culture medium

Component	Concentration	Supplier
Dulbecco's modified eagle medium (DMEM) High Glucose, GlutaMAX		Invitrogen, Karlsruhe, Germany
Fetal bovine serum (FBS)	2 %	Invitrogen, Karlsruhe, Germany
Penicillin-Streptomycin	100 U/mL	Invitrogen, Karlsruhe, Germany
N-2 Supplement	1x	Invitrogen, Karlsruhe, Germany
Epidermal Growth Factor (EGF)	20 ng/mL	Peprotech, Hamburg, Germany
Hydrocortisone	1 µg/mL	Sigma, Darmstadt, Germany

3.3.4. Tumor organoid culture (TOC) medium

Component	Concentration	Supplier
Advanced DMEM/F12		Invitrogen, Karlsruhe, Germany
HEPES	10 mM	Invitrogen, Karlsruhe, Germany
GlutaMAX	10 mM	Invitrogen, Karlsruhe, Germany

Normocin	50 µg/mL	Invitrogen, Karlsruhe, Germany
B27 Retinoic acid free supplement	1x	Invitrogen, Karlsruhe, Germany
N-Acetylcysteine	1 mM	Sigma, Darmstadt, Germany
Prostaglandine E2	15 nM	Sigma, Darmstadt, Germany
Noggin	25 ng/mL	Peprotech, Hamburg, Germany
LY2157299	500 nM	Selleckchem, Housten, TX, USA
EGF	50 ng/mL	Peprotech, Hamburg, Germany
SB202190	7.5 µM	Selleckchem, Housten, TX, USA
Y27632 (48 hours after seeding)	10 µM	Biozol Diagnostics, Eching, Germany
Recombinant TGF-β1 (for treatment or selection only)	20 ng/mL	Peprotech, Hamburg, Germany

3.4. Enzymes

Enzyme	**Supplier**
Gateway® BP Clonase II	ThermoFisher Scientific, Waltham, MA, USA
Gateway® LR Clonase II	ThermoFisher Scientific, Waltham, MA, USA
Phusion® High Fidelity Polymerase	NEB, Frankfurt a.M., Germany
Q5® High Fidelity 2x Master Mix	NEB, Frankfurt a.M., Germany
Fast-AP Thermosensitive Alkaline Phosphatase	Invitrogen, Karlsruhe, Germany

T4 Ligase	NEB, Frankfurt a.M., Germany
Quick Ligase	NEB, Frankfurt a.M., Germany
Taq DNA Polymerase	Biozym Scientific, Oldendorf, Germany
AgeI-HF	NEB, Frankfurt a.M., Germany
MfeI	NEB, Frankfurt a.M., Germany
SgrAI	NEB, Frankfurt a.M., Germany
EcoRI-HF	NEB, Frankfurt a.M., Germany

3.5. Antibodies

3.5.1. Antibodies for immunoblot antibodies

Target	**Supplier**	**Order ID**	**Origin**	**Dilution**
NLE1	Santa Cruz Biotechnology, Dallas, TX, USA	sc-377142	Mouse	1:500
p38α MAPK	Cell Signaling Technology, Danvers, MA, USA	9228	Mouse	1:1000
phospho-p38 MAPK	Cell Signaling Technology, Danvers, MA, USA	4511	Rabbit	1:1000
SMAD4	Cell Signaling Technology, Danvers, MA, USA	46535	Rabbit	1:1000
phospho-SAPK/JNK	Cell Signaling Technology, Danvers, MA, USA	4668	Rabbit	1:500
LC3A/B	Cell Signaling Technology, Danvers, MA, USA	12741	Rabbit	1:1000

Poly ADP-ribose polymerase (PARP)	Cell Signaling Technology, Danvers, MA, USA	9542	Rabbit	1:500
cleaved PARP	Cell Signaling Technology, Danvers, MA, USA	5625	Rabbit	1:500
Alpha-tubulin	Sigma, Darmstadt, Germany	T9026	Mouse	1:500
Beta-actin	Sigma, Darmstadt, Germany	A2066	Rabbit	1:500
c-MYC	Sigma, Darmstadt, Germany	10828-1-AP	Rabbit	1:1000
Cleaved Caspase-3	Cell Signaling Technology, Danvers, MA, USA	9661	Rabbit	1:500
Anti-mouse horseradish peroxidase (HRP)	Dianova, Hamburg, Germany	715-035-150	Donkey	1:10000
Anti-rabbit HRP	Dianova, Hamburg, Germany	711-035-152	Donkey	1:10000

According to the manufacturer, antibodies were diluted in 5 % milk or 5% BSA in TBS-T. HRP: horse radish peroxidase

3.5.2. Antibodies for ChIP

Target	**Supplier**	**Order ID**	**Origin**
c-MYC	Cell Signaling Technology, Danvers, MA, USA	9402	Rabbit
IgG Control	Cell Signaling Technology, Danvers, MA, USA	2729	Rabbit

3.5.3. Antibodies for immunohistochemical staining

Target	Supplier	Order ID	Origin	Dilution
MKI67	Agilent Technologies, Santa Clara, CA, USA	GA626	Mouse	1:100
Cleaved Caspase-3	Cell Signaling Technology, Danvers, MA, USA	9661	Rabbit	1:100

3.5.4. Antibodies for immunofluorescence

Target	Supplier	Order ID	Origin	Dilution
LC-3B	Cell Signaling Technology, Danvers, MA, USA	2775	Rabbit	1:200
Anti-Rabbit Cy3	Jackson Immuno-Research, West Grove, PA, USA	711-165-152	Donkey	1:500

3.6. DNA constructs and oligonucleotides

3.6.1. Plasmids

Name	Description	Distributor
pDONR™ 221	Gateway™ destination vector	ThermoFisher Scientific, Waltham, USA
pMD2.G	2nd generation envelope vector for virus production	A. Trumpp, DKFZ Heidelberg
psPAX2	2nd generation packaging vector for virus production	A. Trumpp, DKFZ Heidelberg

pSpCas9(BB)-2A-GFP	Cas9 from S. pyogenes with 2A-EGFP and cloning backbone for sgRNA	Addgene plasmid #48138
pSpCas9(BB)-2A-GFP SMAD4 guide	Cas9 from S. pyogenes with 2A-EGFP and guide RNA for *SMAD4* knockout	
pSpCas9(BB)-2A-GFP TP53 guide	Cas9 from S. pyogenes with 2A-EGFP and guide RNA for *TP53* knockout	
pLentiCRISPR-E	Lentiviral vector, LentiCRISPR V2 with eSpCas9 and puromycin cassette	Addgene plasmid #78852
pLentiCRISPR-E NLE1 g1	LentiCRISPR V2 with eSpCas9, puromycin cassette, and guide RNA1 for *NLE1* knockout	
pLentiCRISPR-E NLE1 g2	LentiCRISPR V2 with eSpCas9, puromycin cassette, and guide RNA2 for *NLE1* knockout	
pTRIPZ	Doxycycline inducible lentiviral vector	ThermoFisher Scientific, Waltham, USA
pTRIPZ NLE1	Doxycycline inducible lentiviral vector for *NLE1* overexpression	
pTRIPZ c-MYC	Doxycycline inducible lentiviral vector for *c-MYC* overexpression	

pLenti CMV Puro DEST	Gateway destination vector cassette for pTz gateway vector	Addgene plasmid #17452
NLE1 ORF	In pENTR221 Gateway full ORF clone	
c-MYC ORF	In pENTR221 Gateway full ORF clone	

3.6.2. Primer

3.6.2.1.qPCR (SYBR green fluorescence)

ACTB fw	5'-TGACATTAAGGAGAAGCTGTGCTAC-3'
ACTB rv	5'-GAGTTGAAGGTAGTTTCGTGGATG-3'
GAPDH fw	5'-GACAGTCAGCCGCATCTTCT-3'
GAPDH rv	5'-GCGCCCAATACGACCAAATC-3'
PPIA fw	5'-AGCATGTGGTGTTTGGCAAA-3'
PPIA rv	5'-TCGAGTTGTCCACAGTCAGC-3'
LGR5 fw	5'-AATCCCCTGCCCAGTCTC-3'
LGR5 rv	5'-CCCTTGGGAATGTATGTCAGA-3'
SMOC2 fw	5'-AACTGGTCTGCGTGCATAA-3'
SMOC2 rv	5'-CTCTCAGACTGTCCTCCAAATG-3'
PMEPA1 fw	5'-AGAACACTCCGCGCTTCTTA-3'
PMEPA1 rv	5'-GCTTGTGCATTCAGACCAGA-3'
NLE1 fw	5'-CACAGGCTATCTTCAGAGTCCG-3'
NLE1 rv	5'-GTGAAATGTGGTGTCTCTGTGC-3'

3.6.2.2.ChIP qPCR (SYBR Green)

16q22 control fw	5'-CTACTCACTTATCCATCCAGGCTAC-3'
16q22 control rv	5'-ATTTCACACACTCAGACATCACAG-3'
NLE1 promoter fw	5'-ACGGCCTCAGGGATTAGAAA-3'
NLE1 promoter rv	5'-GGCAAGAATCCCTGTTGTGA-3'

NLE1 control fw	5’-AGTTTTACGTGAGGGGACAAGA-3’
NLE1 control rv	5’-TGACAGCTTTTCTGACACCAAG-3’
DKC1 fw	5’-TGTTTTCTCGCTTACCTACGGAT-3’
DKC1 rv	5’-AAATCGCCTAACGACCCATTTC-3’
NPM1 fw	5’-CTCGTGAGCCAGGGATGCT-3’
NPM1 rv	5’-CCCTAGTGCTACCAGCCTCTTAAC-3’

3.6.2.3.qPCR (Taqman™ Gene Expression Assay, Applied Biosystems)

ACTB	Hs99999903_m1
PPIA	Hs99999904_m1
MYC	Hs00153408_m1
NLE1	Hs00216436_m1
CDKN1A/p21	Hs00355782_m1

3.6.2.4.Genotyping

SMAD4 mutation assay fw	5’-TGGAGTGCAAGTGAAAGCCT-3’
SMAD4 mutation assay rv	5’-AGCACTCCATCTTAATTGTCGGT-3’

3.6.2.5.Cloning

SMAD4 guide fw	5’-CACCGGATGGATACGTGGACCCTTC-3’
SMAD4 guide rv	5’-AAACGAAGGGTCCACGTATCCATCC-3’
NLE1 guide 1 fw	5’-CACCGCGGTTGCTAGTGCAGTTCC-3’
NLE1 guide 1 rv	5’-AAACGGAACTGCACTAGCAACCGC-3’
NLE1 guide 2 fw	5’-CACCGCTAGTGCAGTTCCAGGATG-3’
NLE1 guide 2 rv	5’-AAACCATCCTGGAACTGCACTAGC-3’
TP53 guide fw	5’-CACCGGGATGATTTGATGCTGTCCC-3’
TP53 guide rv	5’-AAACGGGACAGCATCAAATCATCCC-3’
attB universal fw	5’-GGGGACAATTTGTACAAAAAGCAGGCTTCAC-3’
attB universal rv	5’-GGGGACCACTTTGTACAAGAAAGCTGGGTG-3’
M13 fw	5’- TGTAAAACGACGGCCAGT-3’
M13 rv	5’- CATGGTCATAGCTGTTTCCTG-3’

3.7. Kits

Application	Kit	Supplier
DNA isolation	GenElute Mammalian Genomic DNA Miniprep Kit	Sigma, Darmstadt, Germany
RNA isolation	High Pure RNA Isolation Kit	Roche, Penzberg, Germany
RNA concentration	Qubit RNA HS Assay	Invitrogen, Karlsruhe, Germany
Complementary DNA (cDNA) Transcription	High-Capacity cDNA Reverse Transcription Kit	Invitrogen, Karlsruhe, Germany
qRT-PCR	primaQUANT CYBR qPCR master mix	Steinbrenner, Wiesenbach, Germany
	primaQUANT Probe qPCR master mix	Steinbrenner, Wiesenbach, Germany
Genotyping	CloneJET PCR cloning Kit Phusion High Fidelity PCR Master Mix	Invitrogen, Karlsruhe, Germany
	Alt-R® Genome Editing Detection Kit	IDT Inc., Coralville, IA, USA
Plasmid purification	NucleoSpin Plasmid EasyPure	Macherey Nagel GmbH, Düren, Germany
Chromatin-Immunoprecipitation (ChIP)	SimpleChIP® Enzymatic Chromatin IP Kit	Cell signaling technology, Danvers, MA, USA
Mycoplasma detection	LookOut Mycoplasma PCR detection Kit	Sigma, Darmstadt, Germany

Cell viability	CellTiter-Glo® 2.0	Promega, Madison, USA
	CellTiter-Glo® 3D	Promega, Madison, USA
Cell cycle distribution	Click-iT™ EdU Alexa Fluor™ 488 Flow Cytometry Assay Kit	Invitrogen, Karlsruhe, Germany
	FxCycle™ Far Red Stain	Invitrogen, Karlsruhe, Germany
Protein concentration	Micro BCA™ Protein Assay Kit	Thermo Scientific, Waltham, MA, USA
Immunohistochemistry	Ventana UltraView DAB IHC Detection Kit	Ventana Medical Systems, AZ, USA
	Cell Conditioning Solution	Ventana Medical Systems, AZ, USA
	ImmPRESS anti-rabbit IgG Polymer Kit (MP-7401)	Vector Laboratories, Burlingame, CA, USA
	3,3`-diaminobenzidine (DAB, K3468)	Agilent Technologies, Santa Clara, CA, USA
	Hematoxylin Gill´s Formula	Vector Laboratories, Burlingame, CA, USA
	Target Retrieval Solution Citrate pH 6	Agilent Technologies, Santa Clara, CA, USA
Apoptosis	FITC Annexin V Apoptosis Detection Kit I	BD Biosciences, NJ, USA

De novo protein synthesis	Click-iT® Plus OPP Alexa Fluor™ 488 Protein Synthesis Assay Kit	ThermoFisher Scientific, Waltham, MA, USA
ROS detection	CellROX® Green Flow Cytometry Assay Kit	ThermoFisher Scientific, Waltham, MA, USA
RNA sequencing	TrueSeq Stranded mRNA Library Prep Kit for Illumina	NEB, Frankfurt a. M., Germany

3.8. Bacteria

Bacteria strain	**Supplier**
Endura Chemically Competent Cells (DUOS)	BioCat, Heidelberg, Germany

3.9. Mice

Mouse strain	**Supplier**
NOD.Cg-PrkdcscidIl2rgtm1Wjl/SzJ (NSG)	Charles River Laboratories, Sulzfeld, Germany

3.10. Solutions and buffers

Laemmli buffer, 2x

- 125 mM tris/HCl, pH 6.8
- 4 % SDS
- 20 % glycerol
- 0.05% bromophenol blue
- 2 % DTT

Lower tris buffer

- 1.5 M Tris, pH 8.8
- 0.2 % SDS

Upper tris buffer

- 1.0 M Tris, pH 6.8
- 0.2 % SDS

Resolving gel, 10%, 10 mL

- 4 mL ddH_2O
- 3.3 mL 30 % acrylamide solution
- 2.5 mL lower tris buffer
- 0.1 mL 10 % SDS
- 0.1 mL 10 % ammonium persulfate
- 0.004 mL TEMED

Resolving gel, 12%, 10 mL

- 3.3 mL ddH_2O
- 4 mL 30 % acrylamide solution
- 2.5 mL lower tris buffer
- 0.1 mL 10 % SDS
- 0.1 mL 10 % ammonium persulfate
- 0.004 mL TEMED

Running buffer for SDS-PAGE, 10x

- 30 g tris
- 140 g glycine
- 100 mL 10% SDS
- Add 1 L ddH_2O

Stacking gel, 10 mL

- 6.8 mL ddH2O
- 1.7 mL 30 % acrylamide solution
- 1.25 mL upper tris buffer
- 0.1 mL 10 % SDS
- 0.1 mL 10 % ammonium persulfate
- 0.01 mL TEMED

TBS-T buffer, 1x

- 1x TBS
- 0.2 % Tween20

Transfer buffer, 10x

- 30 g tris
- 140 g glycine
- Add 1 L ddH_2O

Transfer buffer, 1x

- 100 mL 10x transfer buffer
- 200 mL methanol
- 700 mL ddH_2O

Tris-buffered saline (TBS) buffer, 10x

- 24.2 g tris
- 80 g NaCl
- Add 1 L ddH_2O
- pH: 7.6

TAE buffer, 10x

- 48.1 g tris
- 20 mL EDTA (0.5 M)
- 11.4 mL Acetic Acid
- Add 1 L ddH_2O
- pH: 8.0

TAE buffer, 1x

- 100 mL 10x TAE buffer
- 900 mL ddH_2O

3.11. Software

Software	Supplier
Affinity Designer 1.10.5.1342	Serif (Europe) Ltd, Nottingham, UK
FlowJo v10.7.1	FlowJo LLC, Ashland, OR, USA
Grammarly 6.8.263	Grammarly Inc., SF, CA, USA

GSEA 3.0 Desktop Application	Broad Institute, Inc., Massachusetts Institute of Technology, and Regents of the University of California
GraphPad Prism 7.01	GraphPad Software Inc., La Jolla, CA, USA
Image Studio Ver 5.2.5	Li-COR, Lincoln, NE, USA
ImageJ	Rasband, W.S., ImageJ, U. S. 282 National Institutes of Health, Bethesda, Maryland, USA
Microsoft Office 2016	Microsoft, Redmond, WA, USA
Microsoft 365	Microsoft, Redmond, WA, USA
NIS Elements D Imaging Software, Version 5.00.00 NIS	Nikon Instruments Inc., Melville, NY, USA
Phenochart 1.0.8	Akoya Biosciences, Marlborough, MA, USA
RTCA 1.2.1.1002 Software	Roche, Penzberg, Germany
Simplicity 4.20	Titertek-Berthold, Pfortzheim, Germany
SkanIt Software 2.4.3 Research Edition Varioskan	Thermo Scientific, Waltham, MA, USA

4. Methods

4.1. Cloning

To achieve CRISPR/Cas9-mediated gene deletion of *SMAD4* or *TP53*, guide RNA sequence for targeting *SMAD4* in exon 8 or *TP53* in exon 3 from previously published Drost *et al.* was used and cloned into the pSpCas9(BB)-2A-GFP vector (Addgene #48138) [226]. In brief, oligonucleotides encoding the 20-nt guide RNA (listed in 3.6.2.5) were phosphorylated and annealed, and the pSpCas9(BB)-2A-GFP vector was linearized by digestion with Esp3I according to Ran *et al.* [227]. Next, vector backbone and oligo pairs were ligated using quick ligase (NEB) according to the manufacturer's protocol and subsequently transformed into the *Escherichia coli* strain Endura. Finally, insertions were verified by Sanger sequencing (Eurofins).

Knockout of *NLE1* in CRC cell lines and PDTOs was performed using the CRISPR/Cas9 system. To that, two different guide RNAs (listed in 3.6.2.5) targeting *NLE1* in Exon 2 were designed using the CRISPR design tool from www.synthego.com and cloned into the lentiviral eCas9 expressing vector pLentiCRISPR-E (gift from Phillip Abbosh, Addgene plasmid #78852). Cloning was performed as described in the previous section.

To ectopically express *c-MYC* or *NLE1* in PDTOs, a doxycycline-inducible system via a lentiviral pTz gateway vector was used, as previously described [228]. First, an empty pTRIPz vector was generated by digestion with EcoRI-HF and AgeI-HF (NEB). Then, de-phosphorylation by Fast-AP (ThermoFisher Scientific) was performed. At the same time, the pLenti CMV Puro DEST vector (Addgene #17452) was restricted with SgrAI and MfeI (NEB) and ligated into the pTRIPz backbone, creating the pTz gateway vector. Afterward, an NLE1 or c-MYC open reading frame (ORF) was PCR amplified from human cDNA with attB overhang primers and then re-amplified using attB universal primers (Gateway® Technology protocol, Invitrogen by life technologies) via Phusion® High Fidelity Polymerase (NEB). The attB-flanked NLE1-ORF or MYC-ORF was cloned into pDONR221 using Gateway® BP Clonase® II (ThermoFisher Scientific), and sequences were validated using Sanger Sequencing (Eurofins). Finally, confirmed cDNAs were transferred from pDONR221 to pTz gateway vector using Gateway® LR Clonase® II (ThermoFisher Scientific). Transduced cells were treated for at least 48 hours with 500 ng/mL doxycycline to induce induction.

4.2. Bacterial cell culture

Plasmid transformation was carried out into *Escherichia coli* strain Endura. In detail, chemically competent cells were incubated with plasmid DNA for 30 minutes on ice. Cells were placed on ice for 2 minutes after 45 seconds of heat shock at 42°C. Next, cells

were resuspended in 500 µl LB-medium without antibiotics and incubated for 60 minutes at 37°C while shaking. Finally, the cell suspension was centrifuged, and the pellet was resuspended in 200 µl LB-medium before plating on LB-agar plates with the appropriate antibiotic at 37°C overnight.

The following day, single colonies were used to inoculate 5 mL LB medium supplemented with the appropriate antibiotic and cultured at 37°C overnight. Plasmid DNA was then isolated using NucleoSpin Plasmid EasyPure Kit (Macherey-Nagel) according to the manufacturer's protocol.

4.3. Mammalian cell culture

4.3.1. Cell line culture

SW620 and HT29 cell lines were purchased from ATCC (Wesel, Germany) and cultured in Dulbecco's Modified Eagle Medium (DMEM) supplemented with 10% fetal bovine serum (FBS) and 1x penicillin/streptomycin. The immortalized human colonic epithelial cell line HCEC-1CT (Evercyte GmbH, Vienna, Austria) was cultured in DMEM supplemented with 2% FBS, 1x N2 Supplement (contains insulin, apo-transferrin, and sodium-selenite), 20 ng/ml Epidermal Growth Factor (EGF), 1 µg/ml hydrocortisone and 1x penicillin/streptomycin. HCT116 cells were cultivated in McCoy's 5A Medium with 10% FBS and 1x penicillin/streptomycin Cultures were kept at 37°C with 5% CO_2. Once the cells reached a density of 80-90 %, they were split. After that, cells were rinsed with PBS and incubated with 0.25% Trypsin-EDTA for 5 minutes at 37°C. Digestion was halted by the addition of culture media. Then cells were transferred into new flasks by diluting them 1:5 to 1:20 in fresh medium.

To freeze cells for long-term storage, cells were incubated with 0.25% Trypsin-EDTA, washed as previously described, and resuspended in an appropriate volume of freezing medium (50% DMEM, 40% FBS, 10% DMSO). Approximately 1.5 ml cell suspension was poured into each cryovial and then placed into a Mr.Frosty™ Freezing Container. These containers ensure a rate of cooling of -1°C/minute. After 48 hours at -80°C, the cells were transferred into liquid nitrogen.

The LookOut Mycoplasma PCR detection kit (Sigma) was regularly used to test cell lines for mycoplasma contamination. Cell lines were only used for experiments when tested negative.

4.3.2. Culture of patient-derived tumor organoids

To isolate PDTOs, fresh tissue fragments from primary CRC or liver metastasis were sliced into small pieces and incubated for 15 minutes at room temperature with

Antibiotic-Antimycotics and Normocin. After washing with PBS, tumor pieces were chopped with a scalpel and incubated for 30 minutes at 37°C in disaggregation solution (Advanced DMEM/F12, supplemented with 75 U/mL Collagenase IV, 5 U/mL Dispase II and 10 µM Y-27632). Next, the cell suspension was passed through a 1.2 mm needle with a syringe and washed in PBS. The cell suspension was subsequently passed through a 70 µm cell strainer and incubated in ammonium chloride buffer for 5 minutes at room temperature. After twice washing cells with Advanced DMEM/F12, cells were embedded in Matrigel® at varying cell densities and covered with tumor organoid culture medium (TOC). TOC medium was exchanged every two to three days.

For serial passaging, PDTOs were disaggregated using 0.025% Trypsin-EDTA and passed through a 0.8 mm needle to obtain small or single-cell aggregates. After washing with Advanced DMEM/F12, cells were counted, and 2,000 to 15,000 cells were embedded in 50 µl Matrigel® drops. As before, TOC medium was added to drops after solidification.

For cryopreservation, organoids were harvested using Cell Recovery Solution for 30 minutes on ice and washed with Advanced DMEM/F12 twice. Next, organoids were resuspended in freezing medium (50% Advanced DMEM/F12, 40% FBS, 10% DMSO) and placed into Mr.Frosty™ Freezing Container for slow cooling to -80°C. After 48 hours, organoids were transferred into liquid nitrogen.

The LookOut Mycoplasma PCR detection kit (Sigma) was regularly used to test organoids for mycoplasma contamination. Organoids were only used for experiments when tested negative.

4.3.3. CRISPR/Cas9-mediated knockout of *SMAD4* in PDTOs using electroporation

To achieve CRISPR/Cas9-mediated knockout of *SMAD4* in PDTOs, organoids were electroporated with the pSpCas9(BB)-2A-GFP vector (Addgene #48138) containing a guide RNA for targeting *SMAD4* in exon 8 [226]. Cloning was described previously. In detail, PDTOs were incubated with 0.025% Trypsin-EDTA for 5 minutes at 37°C and passed through a 0.8 mm needle with a syringe to dissociate them. $2x10^5$ single cells were resuspended in 100 µl Opti-Minimal Essential Medium (Opti-MEM) containing 10 µM Y-27632 and 2 µg vector. The suspension was then transferred to an electroporation cuvette (EC-002S, 2-mm gap width, Nepa Gene) and electroporated using the NEPA21 electroporator (Nepa Gene). The following parameters were used: two poring pulses of 160 V, 5 ms, with a pulse interval of 50 ms, followed by 5 transfer pulses of 20 V, for 50 ms, with an interval of 50 ms. After that, 300 µl Advanced DMEM/F-12 was added to the cells, and the cell suspension recovered for 15 minutes at room temperature. Lastly,

cells were embedded in Matrigel® and overlaid with TOC medium containing 10 µM Y27632. After 48 hours, selection with recombinant TGF-β1 (20 ng/ml) was started.

4.3.4. CRISPR/Cas9-mediated knockout of *NLE1* in CRC cell lines and PDTOs using transduction

Twenty-four hours before transfection, HEK293T cells were seeded into T25 flasks to reach a density of 90-95% the next day. For the transfection mix, 500 µl of 150 mM NaCl was mixed with 50 ng/µl polyethylenimine (PEI), 2.5 µg of 2nd generation packaging vectors (0.75 µg pMD2.G, 1.75 µg sPAX2) and 2.5 µg of the lentiviral vector encoding the *NLE1* guide RNA. Following the manufacturer's instructions, virus-containing supernatant was collected 24 and 48 hours after transfection, passed through 0.45 µm filters (Millipore), and concentrated 20-fold using Lenti-X Concentrator solution (Clontech, Takara Bio). Three volumes of concentrator were added, and the mixture was incubated for 3 hours on ice. The mixture was then centrifuged at 1,500 x g for 45 minutes at 4°C, and the supernatant was discarded. Finally, the pellet was resuspended in 500 µl PBS to receive a 20x concentrated virus, and aliquots were prepared. Virus-containing aliquots were stored at -80°C.

Stable transduction of CRC cell lines was performed by incubating cells with 8 µg/ml polybrene and a 20-fold dilution of the concentrated lentivirus particles. In the case of PDTOs, a single cell suspension, as previously described, was generated, and then cells were plated on a Matrigel®-coated 24-well plate. After incubation for 2 hours at 37°C, PDTOs cultures were supplemented with 8 µg/ml polybrene and concentrated virus particles. After 16 hours, the transduced PDTO cells were embedded in Matrigel® drops. For selection, CRC cell lines and PDTOs were cultivated in medium containing 1-2 µg/ml puromycin, starting 24-48 hours post-infection. The selection procedure was accompanied by an appropriate killing control and lasted at least 4-5 days for cell lines and 8–12 days for PDTOs.

4.3.5. CRISPR/Cas9-mediated knockout of *TP53* in CRC cell lines using transfection

Knockout of *TP53* in HCT116 cells was achieved using the CRISPR/Cas9 system. As previously described, guide RNA targeting TP53 in exon 3 was cloned into the pSpCas9(BB)-2A-GFP vector (Addgene #48138). Next, HCT116 were transfected with FuGENE® HD transfection reagent (Promega) according to the manufacturer's protocol, and TP53-deficient HCT116 cells were selected with 20 µM nutlin-3. Nutlin-3 is a known Mouse double minute 2 homolog (MDM2) antagonist, leading to senescence in TP53 wild-type cells [229].

4.4. Protein analysis

4.4.1. Cell lysis

Sub-confluent cell lines were washed with PBS, scraped into ice-cold RIPA buffer containing protease inhibitor, $NaVO_3$, PMSF, and Phosphatase Inhibitor Cocktails 2 and 3, and incubated for 30 minutes on ice.

For PDTOs, the Matrigel® was dissolved using Cell Recovery Solution (Corning) for 30 minutes on ice. After washing the cell pellet twice with cold PBS, cells were lysed with RIPA buffer containing protease inhibitor, $NaVO_3$, PMSF, and Phosphatase Inhibitor Cocktails 2 and 3 for 30 minutes on ice.

After incubation, cell line or PDTO lysates were sonicated for 3x5 seconds with 75% amplitude (HTU Soni130, G. Heinemann) and spun for 20 minutes at 12,000 x g and 4°C. Finally, the supernatant was transferred to new tubes and kept at -80°C for further investigation.

4.4.2. Protein concentration determination

To determine the protein concentration of a sample, the Micro BCA™ Protein Assay Kit was used, and samples were quantified using a Varioskan™ multimode microplate reader (ThermoFisher Scientific).

4.4.3. Immunoblot analysis

Before sodium dodecyl sulfate-polyacrylamide gel electrophoresis (SDS-PAGE), 35 µg whole cell lysates were boiled for 5 minutes at 95°C in Laemmli buffer. After a quick spin, samples were analyzed on 10-12% SDS-acrylamide gels in 1x tris-glycine gel running buffer. Next, proteins were transferred to PVDF membranes for 90 minutes at 100 V with a maximum current of 350 mA in 1x Transfer Buffer using the Mini-Protean-electrophoresis system. Membranes were blocked with either 5% milk in TBS-T or 5% BSA in TBS-T for 1 hour at room temperature to prevent the unspecific binding of antibodies. After that, membranes were incubated with the diluted primary antibody (see 3.5.1) while shaking. The following day, membranes were washed three times for 10 minutes and incubated with the HRP-coupled secondary antibody (see 3.5.1) for 1 hour at room temperature. After incubation, membranes were washed three times with TBS-T, except in the last step, only TBS. Finally, chemiluminescence signals from HRP-coupled secondary antibodies were generated using SuperSignal West Femto Maximum Sensitivity Substrate (ThermoFisher Scientific) or Immobilon Western HRP Substrate (Merck) and detection via the LI-COR Odyssey FC imaging system (LI-COR).

4.5. RNA isolation, cDNA transcription, and qRT-PCR

The High Pure RNA Isolation Kit (Roche) was used to isolate total RNA. Afterward, RNA was transcribed into complementary DNA (cDNA) using the High-Capacity cDNA Reverse Transcription Kit (ThermoFisher Scientific). Both kits were used according to the manufacturer's protocol. For qRT-PCR, the primaQuant CYBR qPCR master mix (Steinbrenner Laborsysteme GmbH) was used and measured on a LightCycler® 480 (Roche). Relative expression values were normalized to *PPIA*, *ACTB,* and/or *GAPDH* expression and calculated using the delta delta cycle threshold (ΔΔCt) method. Primers used for CYBR green-based qRT-PCR reactions are listed in 3.6.2.1.

In addition, qRT-PCR was done using the primaQuant Probe qPCR master mix (Steinbrenner Laborsysteme GmbH) and Taqman^{TM}Gene Expression Assays (ThermoFisher Scientific, see 3.6.2.3) according to the manufacturer's instructions and quantified on a LightCycler® 480 (Roche). Relative expression values were normalized to *PPIA* and *ACTB* expression and calculated using the ΔΔCt method.

4.6. Quantitative chromatin immunoprecipitation (qChIP) analysis

SW620 cells were subjected to ChIP analysis following the manufacturer's instructions (SimpleChIP® Plus Enzymatic Chromatin IP Kit, #9005, Cell Signaling Technologies). In brief, cells were cross-linked with 37% formaldehyde, scraped, and cell nuclei were digested with *Micrococcal Nuclease*. After sonification on ice to 150-900 bp fragments length, 10 µg of fragmented DNA were incubated with 1.6 µg c-MYC (Cell Signaling Technology, #9402S) or 1.6 µg control rabbit IgG (Cell Signaling Technology, #2729S) antibody overnight. After Proteinase K treatment for 2 hours, chromatin fragments were purified, and samples were measured using qRT-PCR. Primers are listed in 3.6.2.2.

4.7. T7EI mismatch cleavage assay

To detect CRISPR/Cas9-mediated genome editing, genomic DNA was extracted using the GenElute Mammalian Genomic Kit (Sigma-Aldrich), and a polymerase chain reaction (PCR) amplification using the Q5 HF Master Mix (NEB) was performed. Primers for PCR amplification are listed in 3.6.2.4. Amplicons were analyzed using the Alt-R® Genome Editing Detection Kit (IDT) according to the manufacturer's instructions.

4.8. Colony Formation assay

To assess colony formation, 500 cells per well were seeded in 6-well plates and cultivated for 2 weeks. The medium was replaced twice a week. For staining, colonies were rinsed

with PBS and then fixed with 4% PFA for 20 minutes at room temperature. Afterward, cells were rinsed with PBS twice and incubated for 20 minutes at room temperature in 5 mg/mL crystal violet solution in 20% methanol. Next, cells were washed with PBS until the background staining was removed and dried for one week. For analysis, pictures were taken with a Nikon D5100 reflex camera, and the crystal violet staining was destained with acetic acid. In particular, 1 ml of 10% acetic acid in ddH_2O was added to each well and incubated on an orbital shaker for 20 minutes. Finally, the destained solution was diluted 1:10 in ddH_2O and analyzed at 595 nm using a Berthold Orion II Microplate Luminometer (Titertek-Berthold).

4.9. Soft Agar assay

To analyze anchorage-independent growth, 12-well plates were coated with 750 µl 0.8% agar (low melting SeaPlaque™ Agarose, Lonza) in medium supplemented with 10% FBS and 1x penicillin/streptomycin. The plates were then allowed to dry for 45 minutes at room temperature. Next, 1,500 cells per well were resuspended in 0.4% agar (low melting SeaPlaque™ Agarose, Lonza) supplemented with medium, 10% FBS, and 1x penicillin/streptomycin (V=700 µl) and seeded on top of the first layer. After drying for 45 minutes at room temperature, plates were cultivated at 37°C and 5% CO_2 in the incubator. The following day, 500 µl medium was added. This medium was replaced twice a week, and colonies were stained and fixed after 14-16 days. To that, 500 µl of 0.005% Crystal Violet solution in 20% methanol was added to each well, and colonies were stained for 1 hour. Lastly, colonies were rinsed with PBS three times and photographed using an AZ100 multizoom microscope (Nikon).

4.10. Transwell migration and invasion assay

Cells were washed four times with PBS the day before seeding and serum-starved for 24 hours. To analyze the migratory capacity of CRC cell lines, 150,000 cells were plated in transwells (8.0 µm pore size membrane; Greiner Bio-One) in serum-free medium. For analysis of the invasion capacity of CRC cell lines, transwells (8.0 µm pore size membrane; Greiner Bio-One) were first coated with 300 µg/mL Matrigel® in coating buffer (0.01 M Tris, pH 8.0, 0.7% NaCl) for 2 hours at 37 °C, according to the Matrigel® (Corning Life Sciences, MA, USA) manufacturer´s protocol. Afterward, 150,000 cells were plated into the coated transwells in serum-free medium. Medium enriched with 10% FBS was placed in the bottom chamber as a chemo-attractant. Analysis was performed 48 hours later. Therefor, cells on the upper side of the transwell membrane were removed, and transwells were rinsed with PBS. Cells were then fixed for 10 minutes at -20°C in ice-cold methanol. After air drying, cells were stained with 100 ng/ml DAPI in PBS and

examined using a Zeiss LSM 700 confocal microscope (Carl Zeiss AG). ImageJ was used to count migrated/invaded cells after capturing three random fields per membrane.

4.11. Immunofluorescence detection of LC3B

CRC cell lines were cultured on glass cover slides (12 mm in diameter) and treated for 24 hours with 50 µm chloroquine (CQ) before analysis. For staining, cells were rinsed with PBS and fixed with 4% PFA for 10 minutes at room temperature. Cells were then rewashed with PBS and permeabilized for 20 minutes at room temperature with 0.2% Triton X-100 in PBS. After that, cover slides were washed twice with PBS and blocked for 30 minutes at room temperature in 100% FBS. The primary antibody (anti-LC3B, pAb #2775, Cell Signaling) was diluted 1:200 in 50% FBS and 0.05% Tween 20 (PanReac Applichem) and added on top on the cover slides after the cover slides were placed onto parafilm. After incubation at 4°C overnight, cover slides were rinsed with 0.05% Tween 20 (PanReac Applichem) in PBS and then incubated with the secondary antibody (anti-Rabbit-Cy3, #711-165-152, Jackson Immuno-Research Europe LTD.). Therefor, the secondary antibody was diluted 1:500 in 50% FBS and 50% of 0.05% Tween 20 in PBS and added on top of the cover slides. After incubation for 30 min at room temperature, cover slides were washed three times with 0.05% Tween 20 in PBS and stained for 5 minutes at room temperature with 100 ng/ml DAPI in PBS. Finally, cover slides were covered with ProLong Gold antifade DAPI mounting medium (#8961S, Cell Signaling), and pictures were captured using a Zeiss LSM700 confocal microscope (Carl Zeiss AG) with a 63x oil immersion objective.

4.12. Next-Generation sequencing (NGS)

The High Pure RNA Isolation Kit (Roche) was used to isolate total RNA according to the manufacturer's instructions. Next, Agilent BioAnalyzer 2100 (Agilent Technologies) was used to assess the quality of isolated RNA. Afterward, isolated RNA was sent to the DKFZ Genomics and Proteomics Core Facility in Heidelberg, Germany, for library preparation and sequencing. In brief, according to the manufacturer's protocol, sequencing libraries were prepared using the TrueSeq Stranded mRNA Library Prep Kit for Illumina (NEB). 50 bp single-read sequencing was done on a HiSeq 2000 v4 (Illumina) according to the manufacturer's instructions. For data analysis, base calling was performed with bcl2fastq 2.19.0.316, and low-quality bases were deleted with Fastq_quality_filter from the FASTX Toolkit 0.0.13 (http://hannonlab.cshl.edu/fastx_toolkit/index.html) with 90 percent of the read requiring a quality phred score >20. PolyA-tail trimming was done using Homertools 4.7 and reads with a length <17 were eliminated [230]. Genomic mapping was implemented with TOPHAT2 for filtered reads with human genome assembly 38 and PicardTools 1.78

CollectRNASeqMetrics (https://broadinstitute.githu.io/picard/) [231]. htseq-count created count data by annotating the gencode.v31.annotation.gtf (https://www.gencodegenes.org/) file [232]. A custom perl script constructed the input tables containing the replicates for the groups to compare for comparison with DESeq2 [233]. Rows in the count matrix having an average count number of <10 were eliminated. After that, using the default parameters, DESeq2 (Version 1.4.1) was run, and the results tables were annotated with gene information (gene symbol, gene type) generated from the gencode.v31.annotation.gtf file.

4.13. Cohort expression data, molecular subtypes, and geneset enrichment analysis

GDC-TCGA datasets were used to collect gene expression data (upper quartile (UQ) normalized fragments per kilobase of exon per million mapped fragments (FPKM)) of colon adenocarcinoma (COAD) and rectum adenocarcinoma (READ) [234]. The NCBI Gene Expression Omnibus (GEO; www.ncbi.nlm.nih.gov/geo) was utilized to download expression data from cohorts used for Consensus molecular subtypes (CMS) and CRC intrinsic subtypes (CRIS) analysis. Five hundred fifteen transplanted human tumor samples (PDX) from 244 patients were also included in the CRIS classification from the Isella *et al*. data set (GSE76402) [235]. Guinney *et al.* provided the information needed to assign samples to CMS subtypes, while Isella *et al.* described the CRIS categories [235, 236]. To acquire expression and clinical data for cohorts used in relapse-free survival analyses, the National Center for Biotechnology Information (NCBI) Gene Expression Omnibus (GEO) (www.nb.nlm.nih.gov/geo) was utilized. The Survminer R-package (https://CRAN.R-project.org/package/survminer) was used to identify suitable cut-off values for the binary classification of cases (high/low expression). Furthermore, the regulation of *NLE1* expression by c-MYC was assessed using gene expression profiling datasets from NCBI GEO (www.nb.nlm.nih.gov/geo) of cell lines/tissues with *c-MYC* ectopic expression or knockdown.

Gene Set Enrichment Analysis (GSEA) was performed using the GSEApreRanked tool of the GSEA 4.1.0 Desktop Application (Broad Institute, http://www.gsea-msigdb.org/gsea/index.jsp) and the Molecular Signatures Database (MSigDB) hallmark gene set, as previously reported in Subramanian *et al.* [237, 238]. GDC-TCGA COAD and READ datasets (n = 638 CRC tissue samples and 591 patients with available survival data) were used to generate *NLE1* gene signatures [234].

4.14. Immunohistochemistry

Whole-tissue sections (2 µm) of formalin-fixed and paraffin-embedded (FFPE) tumor tissues were stained for MKI67 immunohistochemistry using a Ventana Benchmark (Ventana Medical Systems) according to the manufacturer's instructions. As a pre-treatment, Cell Conditioning 1 (CC1) Solution was utilized, and antibody binding was visualized using the Ventana UltraView DAB IHC Detection Kit (all Ventana Medical System). The MKI67 antibody (Clone MIB-1, Agilent Technologies (Dako)) was employed at a dilution of 1:100. To detect cleaved caspase 3 on FFPE sections (2 µm), antigen-retrieval was accomplished using Target Retrieval Solution Citrate pH 6 (Agilent Technologies, Cat. No. S2369), and slides were incubated with a 1:100 dilution of the primary antibody (cleaved caspase-3, #9661, Cell Signaling) for 1 hour at room temperature. The ImmPRESS anti-rabbit IgG Polymer Kit (MP-7401, Vector Laboratories) was used as a detection system. For development, samples were exposed to 3,3`-diaminobenzidine (DAB, K3468, Agilent Technologies) and counterstained with hematoxylin Gill´s Formula (H 3401, Vector Laboratories).

4.15. Flow cytometry-based assays

4.15.1. Cell cycle analysis

For cell cycle analysis, the Clickt-iT™ EdU Alexa Fluor™ 488 Flow Cytometry Assay Kit was combined with the FxCycle™ Far Red Stain for Fluorescence-activated cell sorting (FACS). In brief, cells were labeled with 10 µM 5-ethynyl-2′-deoxyuridine (EdU) for 2 hours at 37°C before being processed according to the manufacturer's instructions. After resuspension of cells in 400 µl 1x Click-iT saponin-based permeabilization and wash reagent, 200 nmol/L FxCycle Far Red Stain and 100 µg/ml RNase was added. Finally, samples were measured on a BD Accuri™ C6 (BD Biosciences) flow cytometer or a MACS Quant® X Flow Cytometer (Miltenyi Biotec).

4.15.2. Apoptosis detection

The Fluorescein isothiocyanate (FITC) Annexin V Apoptosis Detection Kit I (BD Biosciences) was used to quantify cells actively undergoing apoptosis. Before staining, the cell culture medium was collected in 15 ml tubes, and 1 ml Accutase was applied to each well (6-well plate). After 2 minutes of incubation at room temperature, 2 ml medium was added to each well, and the cells were carefully resuspended and transferred to the same 15 ml tubes. The cells were then centrifuged, and the supernatant was removed. Finally, staining was conducted according to the manufacturer's instructions. In brief, cells were washed twice with ice-cold PBS, and the pellet was resuspended in 500-1000 µl (depending on the cell number) 1x Binding buffer. 100 µl of each sample was then

incubated with 5 µl Annexin V and 5 µl propidium iodide for 15 minutes at room temperature in the dark. Finally, 400 µl 1x Binding buffer for each sample was added, and the samples were analyzed on a BD Accuri™ C6 (BD Biosciences) flow cytometer.

4.15.3. *De novo* Protein Synthesis analysis

To detect nascent protein synthesis in cells, CRC cell lines were labeled for 30 minutes with 20 µM O-propargyl-puromycin (OPP, ThermoFisher Scientific) and PDTOs for 1 hour. Before staining with OPP, cells were treated with 50 µg/ml cycloheximide (CHX), a translation inhibitor, for 20 minutes as a positive control for *de novo* protein synthesis suppression. Following OPP labeling, PDTOs were incubated for 5 minutes at 37°C with 0.025% Trypsin-EDTA before carefully passing through a 0.8 mm needle by a syringe to receive single cells. CRC cell lines were also harvested with Accutase. After washing with 1% BSA in PBS, single-cell suspensions were fixed and stained using the Click-IT® Plus OPP Alexa Fluor™ 488 Protein Synthesis Assay Kit (ThermoFisher Scientific). After the Click-IT® reaction, cells were rinsed with 1x Click-IT® Reaction Rinse Buffer (ThermoFisher Scientific). Finally, cells were resuspended in PBS and examined on a BD Accuri™ C6 Flow Cytometer (BD Biosciences).

4.15.4. ROS detection assay

CRC cell lines were stained with the CellROX® Green Flow Cytometry Assay Kit (ThermoFisher Scientific) to detect reactive oxygen species (ROS). In short, according to the manufacturer's instructions, CRC cell lines were labeled for 45 minutes with 1 µM CellROX® reagent (ThermoFisher Scientific). As a positive control for ROS production, cells were treated with 400 µM Tert-butyl hydroperoxide (TBHP) for 1 hour before labeling with the CellROX® reagent. 5 nM SYTOX® Red Dead Cell stain solution was added during the last 15 minutes of CellROX® labeling. Following labeling, CRC cell lines were detached with Accutase and washed in DMEM containing 10% FBS and 1x penicillin/streptomycin. Lastly, cells were resuspended in DMEM medium and examined on a MACSQuant® X Flow Cytometer (Miltenyi Biotec).

4.16. Cell viability assay

4.16.1. xCELLigence™ Proliferation Assay

CRC cell lines ($2x10^3$ cells in 200 µl medium/well) were plated in E16-plates (Acea Biosciences, Inc) according to the manufacturer's protocol for the xCELLigence Real-Time Cell Analyzer (RTCA) DP (Roche/Acea Biosciences). Monitoring of cell growth was performed with one sweep/hour for 145 hours and analyzed via the RTCA 1.2.1.1002 software (Roche). In detail, this machine monitors changes in the electrical impedance of

the gold electrodes on the well surface, yielding the so-called cell index. Over time, an increase in the cell index is a surrogate for active cell proliferation.

4.16.2. CellTiter-Glo® 3D Cell Viability Assay

To investigate how *SMAD4* wild-type or *SMAD4* knockout PDTOs respond to TGF-β treatment, 4,000 cells of each genotype were seeded in 20 µl Matrigel® droplets and covered with TOC medium containing 0.5 µM LY2157299, a TGF-β inhibitor or 20 ng/ml recombinant human TGF-β1. In the first two days, the medium was supplemented with Y27632 to avoid anoikis. Then, the TOC medium was refreshed every 2-3 days.

The CellTiter-Glo® 3D Cell Viability Assay (Promega) was used to measure the ATP content as a surrogate for cell viability at the indicated time points. To summarize, the TOC medium was removed before resuspending Matrigel® droplets in 35 µl Advanced DMEM/F-12 medium and 85 µl CellTiter-Glo® 3D (Promega). After 5 minutes of incubation on a shaker, the cell lysate was resuspended 3-5 times using a pipette and incubated on an orbital shaker for another 15 minutes. Lastly, 100 µl of cell lysate was analyzed on a Berthold Orio II Microplate Luminometer (Berthold). For analysis, the TGF-β treated cells were normalized to their respective, untreated controls, and cell viability was expressed in percent (%).

4.17. Mouse strain and handling of animals

NSG (NOD.Cg-PrkdcscidIl2rgtm1Wjl/SzJ) immunodeficient mice were bought from Charles River Laboratories (Sulzfeld, Germany) and used for xenotransplantation when approximately 12 weeks old. Mice were housed in individually ventilated cages (IVC) in the animal facility at the Pathology Institute of the Ludwig-Maximilians-University (Munich, Germany). A laminar flow hood was used for mice identifications, health controls (scoring), and cage changings. The Institutional Animal Care and Use Committee of the Government of Upper Bavaria, Germany (approval number: ROB-55.2-2532.Vet_02-20-136) approved all animal experiments.

4.18. Endoscopy-guided orthotopic organoid transplantation

Orthotopic transplantation of CRC organoids was performed according to Roper *et al.* [224]. First, tumor organoids were incubated with 1x TrypLE™-Select (ThermoFisher Scientific) for 5 minutes at 37°C before being mechanically dissociated into five- to ten-cell clusters with a syringe (0.8 mm needle). After washing, pellets were resuspended in PBS, 10% Matrigel®, 10 µM Y-27632, and 150 dissociated organoids in 100 µL for each injection (1-2 per mouse) were prepared. Following isoflurane anesthesia, a straight gavage needle flushed the colon with Hank's-balanced salt solution (HBSS). When the

colon was clean, the colonoscopy with a rigid endoscope from Karl Storz (1.9 mm in diameter) with a linear Hopkins lens optics (ColoView System) was started. A custom-made flexible fine needle (33-gauge, custom length of 16 inches, custom point style of 4 at 45°, Hamilton) was utilized to inject the organoid suspensions into the submucosa of the colon. The injection into the submucosa must form a bubble that closes the intestinal lumen and lasts for at least 15 seconds. Only transplanted animals that had fulfilled this quality criteria were considered for further examination.

4.19. Patient-derived fresh tissues for organoid culture and FFPE tissues

Fresh normal and cancerous tissue specimens were collected from patients undergoing curative colectomy or partial hepatectomy at the University Hospital Großhadern at the Ludwig-Maximilians-University (LMU) Munich, Germany. A pathologist obtained samples from remaining resected tissue that was not required for diagnostic purposes, and samples were anonymized irrevocably. The LMU Munich's ethics council characterized this procedure as uncritical and was explicitly allowed for our projects (project-No. 591-16-UE and 17-771-UE).

4.20. Imaging

An AZ100 multizoom microscope (Nikon) and the NIS Elements Imaging Software (Version 5.00.00, Nikon) was used to image PDTOs.

For imaging of dissected mouse organs and tumor burden, a Zeiss Stemi 2000-C Zoom Stereomicroscope with CL6000 LED illumination and a Zeiss AxioCam ERc 5s (Carl Zeiss AG) was used.

The Vectra® Polaris™ Automated Quantitative Pathology Imaging System (Akoya Biosciences) was used to scan FFPE tissue slides from immunohistochemical staining for MKI67 and cleaved caspase 3.

4.21. Statistical analysis

Statistical analysis was performed using GraphPad Prism software (V7.01). Student's t-test (unpaired, two-tailed, Holm-Sidak method, with alpha level=0.05) was used to analyze significant differences between two groups of biological replicates from *in vitro* studies. In contrast, in biological replicates from CRC organoid xenotransplantation experiments (Figure 37), an unpaired t-test with Welch's correction was utilized to account for different unequal standard deviations between groups. A multiple comparison one-way analysis of variance (ANOVA) test was employed when comparing three or

more groups. In the case of unpaired data, one-way ANOVA combined with Tukey's multiple comparisons test was performed. A Dunnett's test was also performed if more than one sample was compared to the untreated control. To compare data with two different parameters, a two-way ANOVA with either Tukey's (when all samples were compared with each other) or Sidak's (when only specific treatments were compared with each other) multiple comparison test was used. Asterisks (*: P-value ≤ 0.05, **: P-value ≤ 0.01, ***: P-value ≤ 0.001, ****: P-value ≤ 0.0001) indicate statistical significance and are annotated in the figure legends.

5. Results

5.1. Effect of *SMAD4* deletion on tumor growth and gene expression in CRC organoids

To distinguish transcriptional changes in *SMAD4* wild-type and *SMAD4*-knockout PDTOs under TGF-β treatment, we first generated two syngeneic PDTO lines with a *SMAD4* deletion in exon 8. For this, we employed a CRISPR/Cas9 approach using electroporation in PDTO4 and PDTO2. According to whole exome sequencing, both lines were wild-type for *SMAD4*. After electroporation, PDTOs were selected with TGF-β for three weeks. TGF-β leads to growth arrest in *SMAD4* wild-type cells, whereas *SMAD4*-knockout derivatives keep growing. To prove that our PDTOs contained a loss of *SMAD4*, we analyzed both lines and their derivatives on the genomic and protein level. For analysis of on-target genome editing, the T7 endonuclease I (T7EI) mismatch cleavage assay was used (see Material and Methods). In brief, the targeted genomic region was PCR amplified, then denatured and reannealed to allow the formation of heteroduplexes between wild-type and CRISPR/Cas9-mutated DNA. Then, PCR products were digested with T7EI and analyzed via agarose gel electrophoresis. After successful CRISPR/Cas9-mediated gene editing, the T7EI endonuclease was able to cleave mismatched heteroduplexes. After cleavage, a band of around 200 bp arose (Figure 9A). In addition, SMAD4 expression was examined in immunoblot analysis and confirmed loss of SMAD4 in both *SMAD4*-knockout PDTO lines (referred to as PDTO S4-KO, Figure 9B).

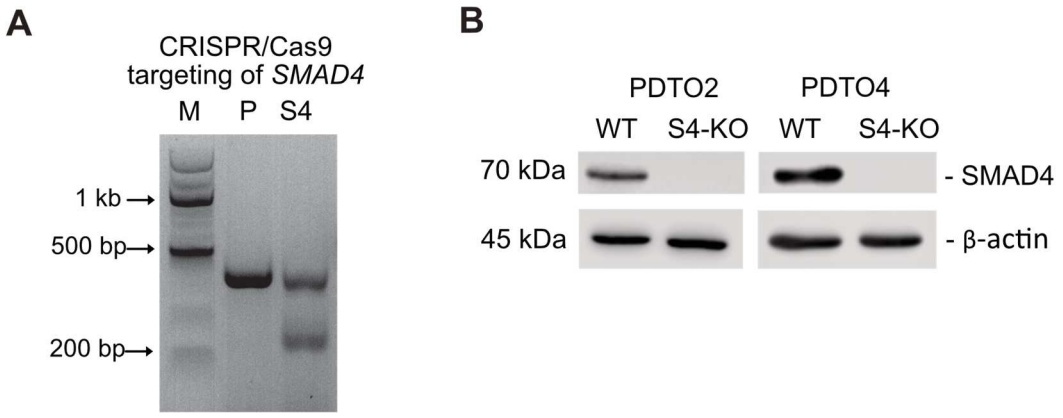

Figure 9: Deletion of *SMAD4* in CRC organoids using CRISPR/Cas9
A) T7EI mismatch cleavage assay performed on genomic DNA from CRISPR/Cas9 edited *SMAD4*-knockout (S4) PDTOs or *SMAD4* wild-type parental PDTOs (P). M, marker. B) Protein expression levels of SMAD4 in *SMAD4* wild-type (WT) and *SMAD4*-knockout (S4-KO) PDTO lines 2 and 4 were detected by immunoblotting. Housekeeping protein ß-Actin was used as a loading control [adapted from 239]. The reuse of figures was allowed by AACR (Creative Commons CC-BY-NC-ND license).

To elucidate the effect of TGF-β treatment on *SMAD4* wild-type and their *SMAD4*-knockout derivatives, cells were seeded in either TOC medium with LY, a known TGF-β inhibitor, or in TOC medium supplemented with TGF-β. In both lines, the parental PDTO2 and PDTO4 under TGF-β treatment showed much smaller organoids than the control cells in the medium with LY. In contrast, the *SMAD4*-knockout derivatives (PDTO2 S4-KO, PDTO4 S4-KO) grew normally in TGF-β containing medium (Figure 10A). This was also reflected in the ATP-based CellTiter-Glo® 3D assay, where TGF-β significantly reduced cell viability in parental PDTOs, whereas *SMAD4*-knockout derivatives cell viability remained stable (Figure 11B).

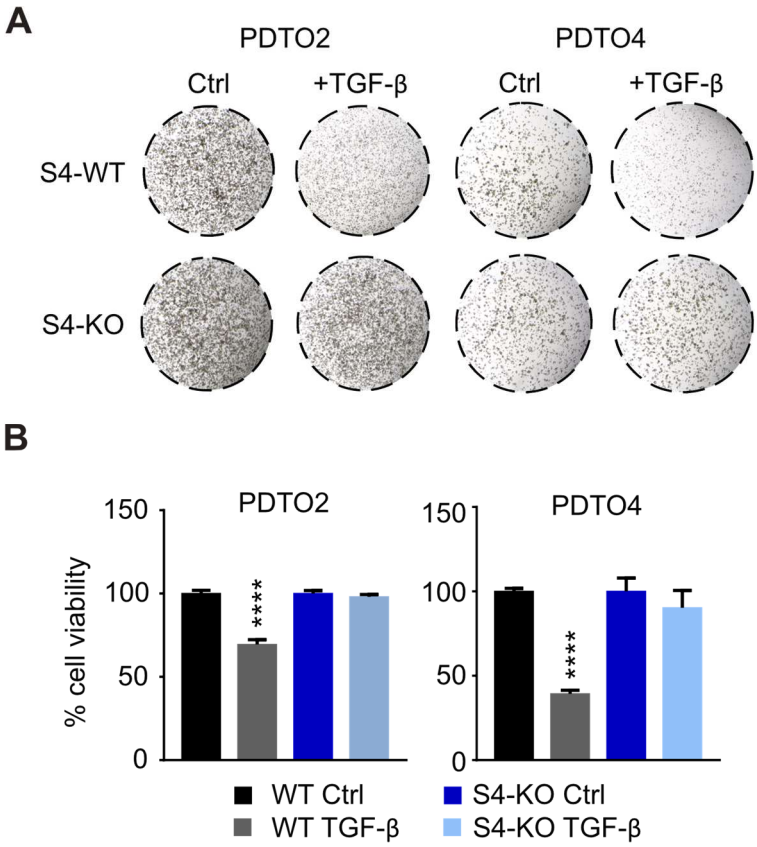

Figure 10: Effect of *SMAD4* deletion on tumor growth in CRC organoids
A) Enhanced focal images of *SMAD4* wild-type (S4-WT) or *SMAD4*-knockout (S4-KO) PDTO lines 2 and 4 cultivated in tumor organoid culture (TOC) medium containing recombinant TGF-β1 (20 nM) or without (Ctrl). PDTO2 was cultivated for 7 days, respectively PDTO4 for 10 days. B) Cell viability of *SMAD4* wild-type (WT) and *SMAD4*-knockout (S4-KO) organoid lines cultivated in TOC medium containing 20 nM recombinant TGF-β1 or without (Ctrl) was determined by measuring ATP levels (CellTiter-Glo® 3D). PDTO2 was cultivated for 7 days, respectively PDTO4 for 10 days. Asterisks (****: P-value ≤ 0.0001) indicate statistical significance between samples as determined by one-way ANOVA plus Tukey's multiple comparisons test. Data are represented as mean ± SD (n = 4) [modified from 239]. The reuse of figures was allowed by a Creative Commons CC-BY-NC-ND license.

Next, we investigated the spectrum of de-regulated genes in *SMAD4*-knockout derivatives under TGF-β treatment. To answer this, next-generation sequencing (RNA-Seq) on PDTO S4-KO versus parental PDTO lines after TGF-β treatment for 72 hours

was performed. Gene set enrichment analysis (GSEA) revealed a positive correlation with proliferation gene sets (c-MYC and E2F targets [237, 238]) and human colonic stem cell gene sets [240] in TGF-β-exposed PDTO S4-KO lines (Figure 11, left panels). Furthermore, de-regulated genes negatively correlated with TGF-β signaling and differentiation (Figure 11, right panels). This agrees with our observations on organoid growth, where PDTO S4-KO lines under TGF-β treatment proliferated faster than parental counterparts and past literature showing that loss of SMAD4 correlates with a more stem cell-like phenotype [117].

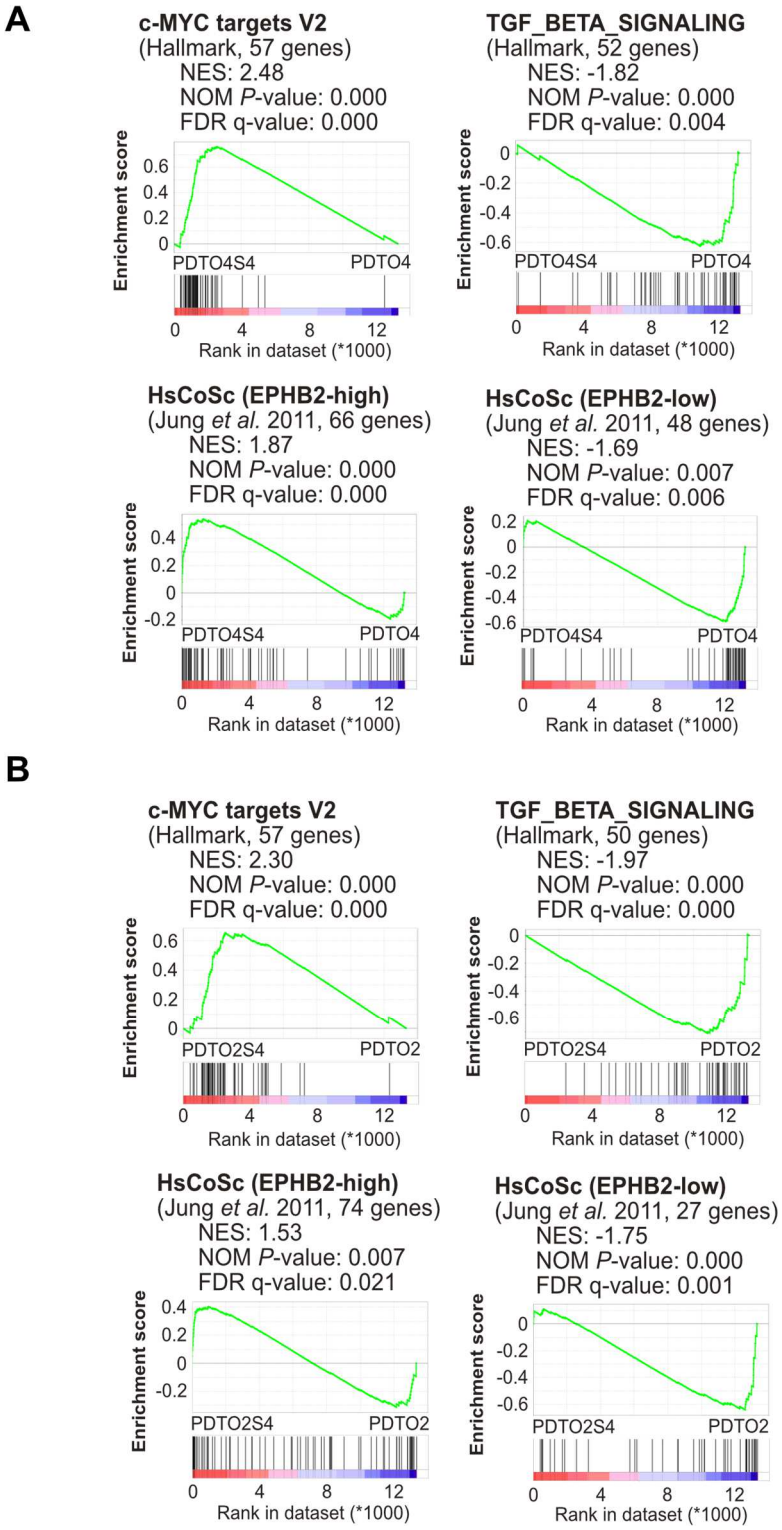

Figure 11: Gene set enrichment analysis of *SMAD4*-knockout (S4-KO) and *SMAD4* wild-type (WT) CRC organoids under TGF-β treatment

A) Gene set enrichment analysis (GSEA) of PDTO4 S4-KO vs. PDTO4 WT cultivated in TGF-β-containing TOC medium. B) Gene set enrichment analysis (GSEA) of PDTO2 S4-KO vs. PDTO2 WT cultivated in TGF-β-containing TOC medium. Enrichments of the following gene sets are shown: c-MYC targets V2, TGF-β signaling (MSigDB Collections, Broad Institute), EPBH2^{high} and EPBH2^{low} human colonic stem cells (HsCoSC, from [240]). NES: normalized enrichment score. NOM P-value: nominal P-value. FDR-q: False discovery rate q-value [adjusted from 239]. The reuse of figures was allowed by AACR (Creative Commons CC-BY-NC-ND license).

To confirm our next-generation sequencing (RNA-Seq) results, quantitative real-time PCR (qRT-PCR) was performed. Loss of *SMAD4* reduced the strong induction of prostate transmembrane protein, androgen induced 1 (*PMEPA1*), a known TGF-β target gene [241]. In addition, downregulation of intestinal stem cell marker genes such as leucine-rich repeat-containing G protein-coupled receptor 5 (*LGR5*) and SPARC-related modular calcium binding 2 (*SMOC2*) was prevented in PDTO S4-KO lines, indicating a more stem cell-like phenotype (Figure 12).

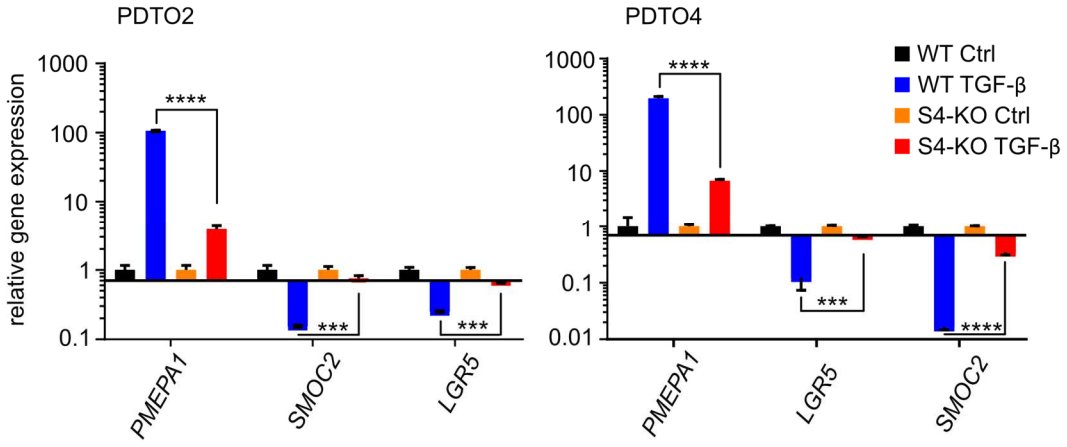

Figure 12: Confirmation of next-generation RNA sequencing results via qRT-PCR
Gene expression levels of *LGR5*, *SMOC2*, and *PMEPA1* were analyzed in *SMAD4* wild-type (WT) and *SMAD4*-knockout (S4-KO) PDTO lines cultivated in TOC medium containing recombinant TGF-β1 (20 nM) for 72 hours or without (Ctrl) via qRT-PCR. Asterisks (***: P-value <0.001 ****: P-value ≤ 0.0001) indicate statistical significance between PDTO S4-KO and PDTO WT in the presence of recombinant TGF-β1 as determined by ordinary two-way ANOVA plus Tukey's multiple comparison test. Data are represented as mean ± SD (n = 3) [adapted from 239]. The reuse of figures was allowed by AACR (Creative Commons CC-BY-NC-ND license).

These data show that *SMAD4* was successfully deleted in two PDTO lines using a CRISPR/Cas9-based approach, and *SMAD4*-knockout derivatives were not responding to TGF-β anymore. Moreover, according to next-generation sequencing, S4-KO lines under TGF-β treatment enriched proliferation and stem cell gene sets.

5.2. TGF-β-mediated downregulation of vulnerability genes is prevented by *SMAD4* mutation

Since *SMAD4* mutations correlate with poorer overall survival in CRC patients, we wondered which de-regulated genes in our RNA-seq list conferred an advantage on cancer cells in a TGF-β rich environment and might represent a new therapeutic target in advanced CRC [242]. To this end, we combined our list with 284 genes, showing a log2-fold enrichment of >0.6 in both PDTO S4-KO lines under TGF-β treatment, with the Cancer Dependency Map (DepMap) project. The DepMap project systematically

identifies genetic dependencies and small molecule sensitivities in a tumor-specific manner [[243, 244], DepMap, https://depmap.org/portal/home/#/]. To that, a large number of genome-scale RNA interference (RNAi)-based loss-of-function screens in 501 cell lines was performed and subsequently analyzed to quantify the on- and off-target effects of each RNAi reagent. This data was then combined with the genomic characteristics of these cell lines. Thus, the authors were able to predict cancer dependencies. If the dependency score was close to 0, the gene was defined as non-essential. The gene was essential when the dependency score was close to 1 [[244], DepMap, https://depmap.org/portal/home/#/]. Later, the same approach was applied to data derived from CRISPR/Cas9-based loss-of-function studies in 324 cell lines [[243], DepMap, https://depmap.org/portal/home/#/]. In the last years, the DepMap database continuously evolved further. The CRISPR/Cas9 screens are based on 1078 cell lines, and the RNAi screens are based on 553 cell lines [DepMap, https://depmap.org/portal/home/#/].

In our approach, a cut-off < -0.8 in two independent CRISPR/Cas9 screens was chosen to identify genes that show a strong, negative effect on cell viability. Surprisingly, only 11 of the 284 genes (*c-MYC,* Interferon-Induced Transmembrane Protein 3 *(IFITM3), NLE1,* N-Acetyltransferase 10 *(NAT10), FBL,* RNA Polymerase III Subunit K *(POLR3K),* Proteasome Assembly Chaperone 4 *(PSMG4),* Ribosomal RNA processing 1 *(RRP1),* U6 snRNA-associated Sm-like protein LSm6 *(LSM6),* GINS Complex Subunit 2 *(GINS2),* and Protein Arginine Methyltransferase 1 *(PRMT1*)) fulfilled these criteria. One example was the proto-oncogene *c-MYC,* which has already been described to promote CRC progression in multiple ways [245]. Surprisingly, 4 of the 11 essential genes (*FBL, NAT10*, *NLE1*, and *RRP1*) are part of the ribosome biogenesis and functionality. This fits previously published data showing that *SMAD4* mutations lead to high biosynthetic capacity in CRC, but which genes contribute to this phenotype remains unknown [246]. We decided to focus our studies on *NLE1* because it displayed the most consistent enrichment within this functional group and was identified as an essential gene in CRC cell lines (Figure 13).

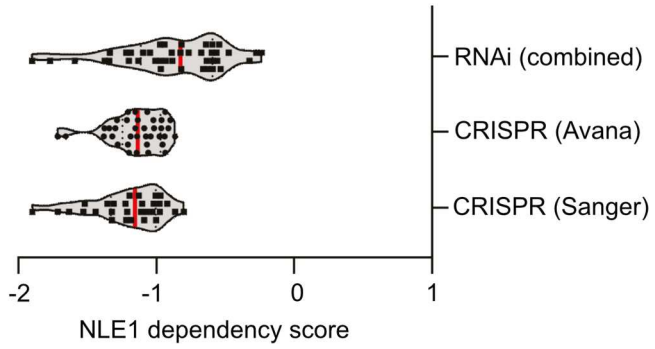

Figure 13: Dependency score of NLE1 in CRC cell lines by the DepMap project
Violin plots demonstrating the dependency score of NLE1 in CRC cell lines derived from the DepMap project. Black squares represent the viability score of a cancer cell line upon small interfering RNA (siRNA)-mediated downregulation of *NLE1* (RNAi combined) or CRISPR/Cas9-mediated *NLE1* knockout in two different screens (Avana and Sanger). A negative effect on cell viability is defined by a score lower than 0. Data was provided by Dr. Matjaz Rokavec [modified from 239]. Reuse of the figure was allowed by AACR (Creative Commons CC-BY-NC-ND license).

To confirm that TGF-β/SMAD signaling regulates *NLE1* gene expression, quantitative real-time PCR in our PDTO and PDTO S4-KO lines was performed in the presence of TGF-β. A much lower *NLE1* expression in PDTOs compared to PDTO S4-KO lines could be observed (Figure 14). This is in line with *c-MYC* gene expression, which was also much lower in wild-type PDTOs than in their *SMAD4*-deficient counterparts (Figure 14).

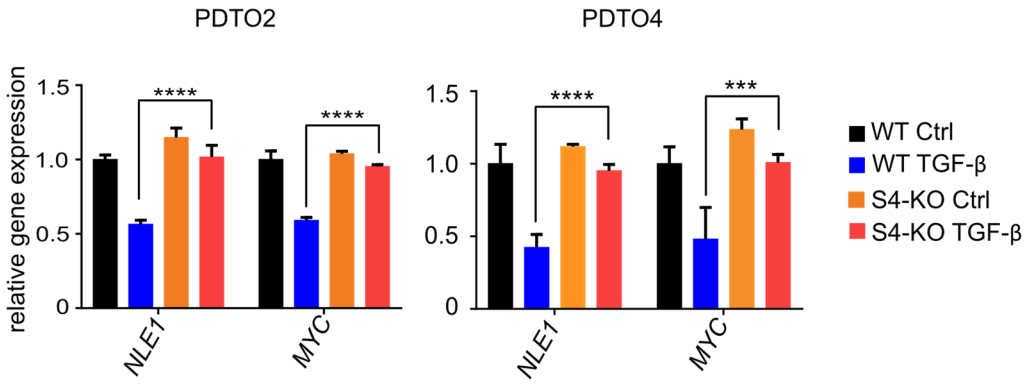

Figure 14: qRT-PCR analysis of vulnerability genes in *SMAD4*-knockout (S4-KO) and *SMAD4* wild-type (WT) CRC organoids under TGF-β treatment
Gene expression levels of *NLE1* and *c-MYC* were analyzed in *SMAD4* wild-type (WT) and *SMAD4* knockout (S4-KO) PDTO lines cultivated in TOC medium containing recombinant TGF-β1 (20 nM) for 72 hours or without (Ctrl) via qRT-PCR. Asterisks (***: P-value <0.001 ****: P-value ≤ 0.0001) indicate statistical significance between PDTO S4-KO and PDTO WT in the presence of recombinant TGF-β1 as determined by ordinary two-way ANOVA plus Tukey's multiple comparison test. Data are represented as mean ± SD (n = 3) [adjusted from 239]. The reuse of figures was allowed by AACR (Creative Commons CC-BY-NC-ND license).

Collectively, these results show that *SMAD4* mutations prevent TGF-β mediated downregulation of vulnerabilities genes.

5.3. c-MYC and TGF-β signaling regulates NLE1 expression in CRC

Previous studies showed that c-MYC could modify ribosomal functionality. In detail, c-MYC binds to promoters of dyskerin pseudouridine synthase 1 (*DKC1*) and nucleophosmin 1 (*NPM1*), thereby altering ribosomal RNA pseudouridylation and 2-O´ methylation [247-250]. Therefore, we wondered if c-MYC can also modify the expression of *NLE1*. We examined publicly available datasets from experiments where c-MYC has been silenced via siRNAs or ectopically overexpressed in different cancer cell lines. It was observed that *NLE1* expression increased upon c-MYC overexpression (indicated in red, Figure 15) and decreased after the knockdown of c-MYC (indicated in blue, Figure 15).

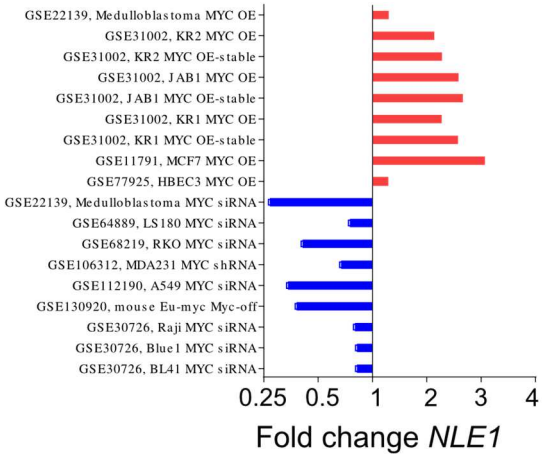

Figure 15: Meta-analysis of *NLE1* mRNA expression in public data sets reveals a link to c-MYC expression
Fold change of *NLE1* mRNA Expression upon c-MYC overexpression (OE, red bars) or c-MYC knockdown by RNA interference (siRNA, blue bars) in different cell lines from publicly available data sets (NCBI Gene Expression Omnibus, GEO) is shown. Each experiment is assigned to its corresponding GEO accession number. Data was provided by Dr. Matjaz Rokavec [adapted from 239]. Reuse of the figure was allowed by AACR (Creative Commons CC-BY-NC-ND license).

Furthermore, we investigated if ectopically expressed c-MYC could rescue the TGF-β-mediated downregulation of *NLE1*. To this end, a TGF-β-responsive CRC organoid line (PDTO4) was stably transduced with lentiviruses encoding for a doxycycline-inducible *c-MYC* open reading frame (referred to as PDTO4 pTz-MYC) or an empty virus (referred to PDTO4 pTz-Empty). Then stably transduced CRC organoids were treated with recombinant TGF-β for 72 hours to decrease NLE1 expression. After these 72 hours, CRC organoids were either kept under TGF-β treatment or doxycycline was added for 48 hours on top. As expected, ectopic c-MYC completely rescued NLE1 mRNA and protein expression, whereas NLE1 levels in cells without ectopic c-MYC expression were still downregulated (Figure 16A, B). In comparison, *LGR5*, a known stem cell marker and not

a c-MYC target gene, was not significantly changed (Figure 16A). Interestingly, overexpression of c-MYC did not lead to higher NLE1 levels relative to non-treated control PDTOs (Figure 16A, B). This indicates that the NLE1 expression mediated by c-MYC had already reached a plateau in this cellular context.

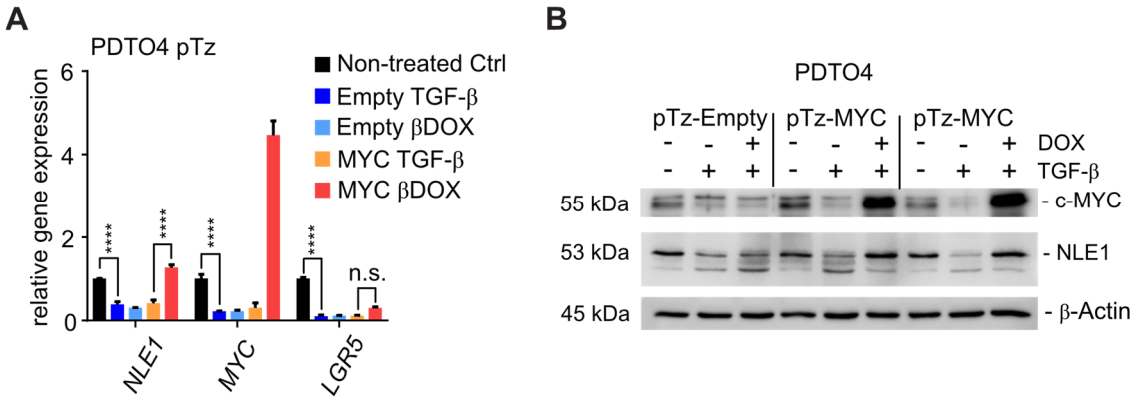

Figure 16: Overexpression of c-MYC can rescue TGF-β-mediated downregulation of NLE1
Stable transduction of PDTO4 (*SMAD4* wild-type) cells with lentiviral particles encoding for a doxycycline-inducible *c-MYC* allele (pTz-MYC) or with a control virus (pTz-Empty) was performed. Cells were treated with recombinant TGF-β1 (20 nM) for 5 days alone, or recombinant TGF-β1 (20 nM) was combined with doxycycline (500 ng/ml) 48 hours prior to analysis (βDOX). Control cells were left untreated. A) Gene expression levels of *NLE1*, *c-MYC*, and *LGR5* were analyzed in PDTO4 cell lines described before. Asterisks (****: P-value ≤ 0.0001) indicate statistical significance between samples as determined by two-way ANOVA plus Tukey's multiple comparisons test. Data are represented as mean ± SD (n = 3). B) Protein expression levels of c-MYC and NLE1 in PDTO4 cell lines described before were detected by immunoblotting. Two independent experiments for PDTOs transduced with the pTz-MYC virus are shown. Housekeeping protein ß-actin was used as a loading control [modified from 239]. The reuse of figures was allowed by AACR (Creative Commons CC-BY-NC-ND license).

Analysis of different c-MYC ChIP-seq data sets from different cancer cell lines (available via the Encyclopedia of DNA Elements, ENCODE) indicated that c-MYC binds to the promoter region of *NLE1* (Figure 17A). Therefore, we decided to perform chromatin immunoprecipitation with subsequent qRT-PCR analysis (qChIP) (Figure 17B) [251]. Primers were designed in the E-box (CACGTG)-containing promoter region of the *NLE1* gene (*NLE1p*) in CRC cells and ~5 kb downstream of the possible c-MYC binding site (*NLE1_ctrl*). Indeed, qRT-PCR analyses of the *NLE1* promoter region in the pulldown enriched for c-MYC bound DNA elements revealed higher levels than the pulldown with the isotype control. Furthermore, qRT-PCR analyses of the control region in both pulldowns showed no differences. As a positive control for already described c-MYC target genes, the promoter regions of *DKC1* and *NPM1* were analyzed [247, 250]. Here, the pulldown enriched for c-MYC bound DNA elements revealed higher levels than the pulldown isolated with the isotype control antibody. These data prove that c-MYC directly binds to the promoter region of *NLE1*.

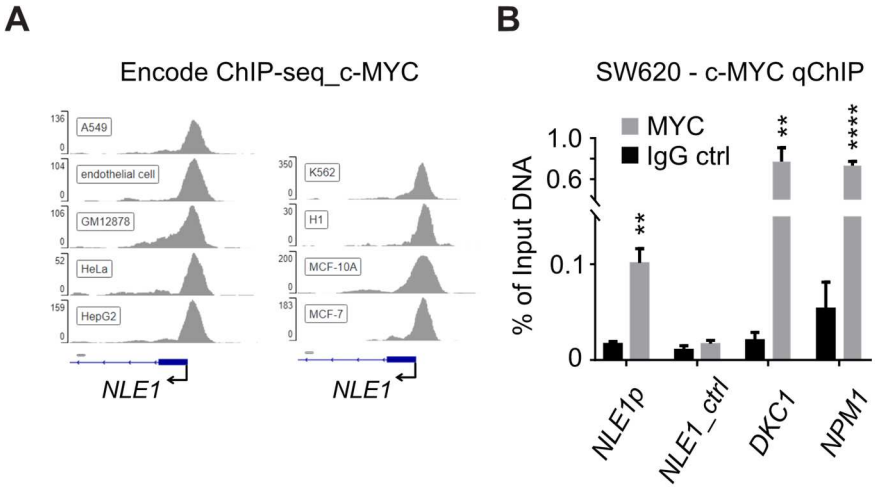

Figure 17: c-MYC directly binds to the *NLE1* promoter region
A) c-MYC ChIP-seq data of different cell lines indicate that c-MYC binds to the *NLE1* promoter region. Only one consensus c-MYC binding sequence (E-box, CACGTG) in the genomic NLE1 sequence is covered by ChIP-seq peaks. The number of ChIP-seq reads is indicated on the y-axis. The Encyclopedia of DNA Elements (ENCODE) Consortium provided the data, and the Integrative Genome Browser (IGV, Broad Institute) was used to visualize the ChIP-seq peaks in the *NLE1* promoter region. Data was provided by Dr. Matjaz Rokavec. B) Chromatin immunoprecipitation combined with qRT-PCR (qChIP) analysis was performed on genomic DNA from SW620 cells. The percentage of chromatin input defines the amount of DNA immunoprecipitated with an anti-MYC antibody or rabbit IgG control. As expected, the *NLE1* gene promoter (*NLE1p*) amplicon is enriched compared to an amplicon located approximately 5 kb downstream within *NLE1* (*NLE1_ctrl*). In addition, the promoter regions for *DKC1* and *NPM1*, containing known c-MYC binding sites, were also enriched and served as a positive control. Asterisks (** P-value < 0.01; **** P-value < 0.0001) indicate statistical significance between c-MYC IgG and rabbit control IgG groups as determined by multiple t-tests corrected for multiple comparisons using the Holm-Sidak method. Data are represented as mean ± SD (n = 3) [adjusted from 239]. The reuse of figures was allowed by AACR (Creative Commons CC-BY-NC-ND license).

In line with the previous results, gene set enrichment analysis of a CRC patient cohort resulting from the GDC-TCGA-COAD plus GDC-TCGA-READ RNA-Seq data sets (n=638 CRC samples, see Materials and Methods) revealed a positive correlation between *NLE1* expression and c-MYC target genes and a negative correlation with TGF-β signaling (Figure 18). Therefore, these data/analyses prove that c-MYC and TGF-β regulate NLE1 levels in CRC patients.

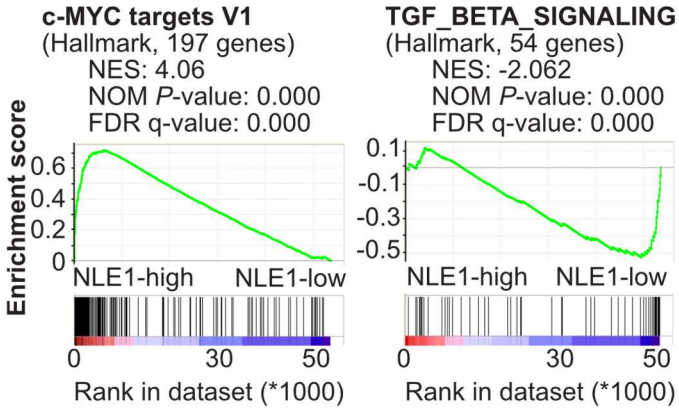

Figure 18: *NLE1* expression correlates with c-MYC targets and TGF-β signaling gene sets in CRC patient cohorts
Gene set enrichment analysis (GSEA) of *NLE1*^{high} and *NLE1*^{low} expressing tumors generated from the GDC-TCGA-COAD plus GDC-TCGA-READ RNA-Seq data sets (n = 638 CRC samples, see Materials and Methods). Enrichments of the following gene sets are shown: c-MYC targets V1, TGF-β signaling (MSigDB collections, Broad Institute). NES: normalized enrichment score. NOM P-value: nominal P-value. FDR-q: False discovery rate q-value [adapted from 239]. The reuse of figures was allowed by AACR (Creative Commons CC-BY-NC-ND license).

In summary, the downregulation of NLE1 is mediated by TGF-β in a *SMAD4*-dependent manner, and the proto-oncogene c-MYC, which can also be repressed by TGF-β/SMAD signaling, can rescue NLE1 expression in the context of active TGF-β signaling. Therefore, NLE1 levels in CRC cells are regulated by a TGF-β/SMAD4/c-MYC axis.

5.4. NLE1 is essential for *de novo* protein biosynthesis in CRC cell lines and organoids

In the past, NLE1 was already described as necessary during ribosomal maturation and function [136, 140, 141]. To this end, we investigated the effect of NLE1 loss on *de novo* protein biosynthesis capacity in CRC cells. We first generated CRC cell lines and PDTOs with an *NLE1* loss using CRISPR/Cas9. In detail, CRC cell lines and PDTOs were stably transduced with lentiviral particles encoding a *Streptococcus pyogenes* Cas9 derivative and a guide RNA targeting exon 2 of *NLE1*. To exclude possible off-target effects, two different guide RNAs were utilized (Figure 19A, Figure 20A). To determine *de novo* protein biosynthesis rates, CRC cell lines and PDTOs were labeled with the Click-iT® Plus OPP Protein Synthesis Assay Kit and analyzed via flow cytometry. The Click-iT® Plus OPP Protein Synthesis Assay Kit is based on O-propargyl-puromycin (OPP), a puromycin analog that incorporates into nascent polypeptide chains and thereby terminates translation. When the Alexa Fluor® picolyl azide and the Click reaction reagent are added, a chemo-selective ligation occurs, also called “click” reaction. This then allows the detection of the modified proteins [252].

Analysis of SW620 and HT29 cells revealed that control cells (referred to as Empty) showed a much higher OPP signal compared to their *NLE1* knockout derivatives (referred

to as NLE1g1, NLE1g2) (Figure 19B, C). In addition, a substantial decrease in OPP signal was observed in control cells treated with cycloheximide (CHX), a translation elongation inhibitor, proofing that OPP incorporation was almost completely prevented (Figure 19B, C). When comparing *NLE1* knockout derivatives with the cycloheximide-treated control cells (Empty+CHX), we concluded that ablation of *NLE1* leads to lower *de novo* protein biosynthesis rates.

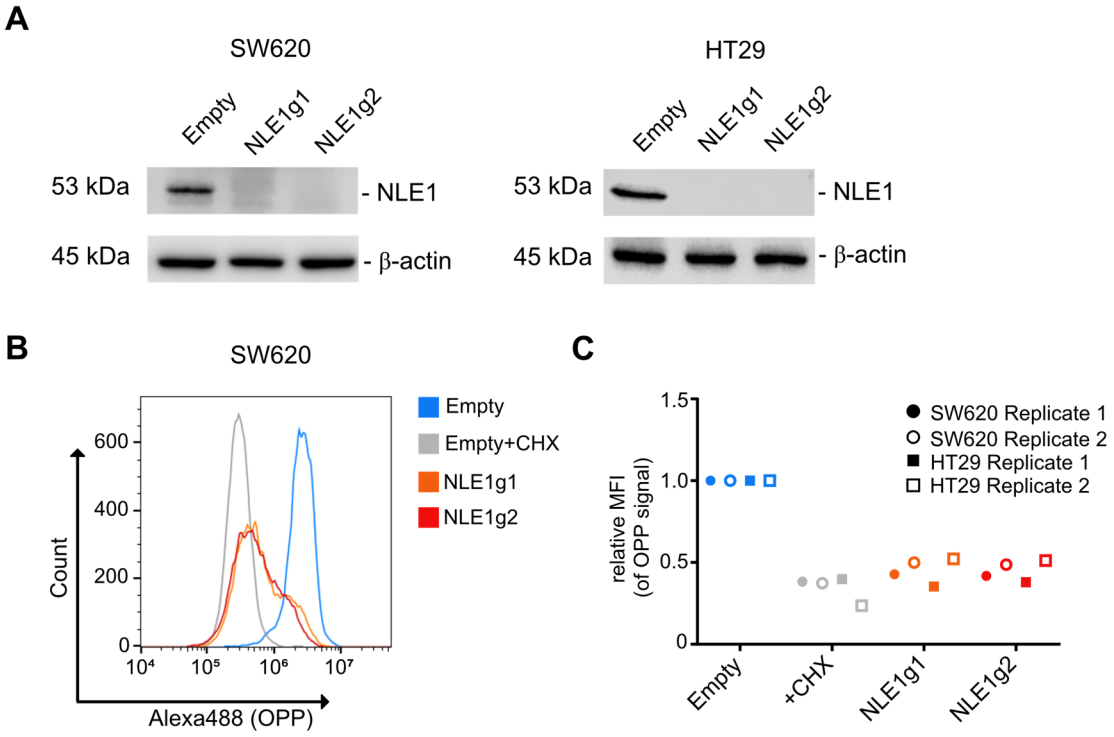

Figure 19: NLE1 is essential for *de novo* protein biosynthesis in CRC cell lines
A) Protein expression levels of NLE1 in SW620 (left panel) and HT29 (right panel) cells edited via CRISPR/Cas9 to achieve *NLE1* knockout were detected by immunoblotting. Two different guide RNAs (NLE1g1, NLE1g2) were used. Control cells were transduced with the same vector but without guide RNAs (Empty). Housekeeping protein β-actin was used as a loading control. B) Flow cytometry analysis of OPP incorporation in SW620 Empty cells (blue), SW620 Empty cells treated with cycloheximide (CHX) (grey), and SW620 *NLE1* knockout cells (NLE1g1 in orange, NLE1g2 in red). C) Mean fluorescence intensity (MFI) levels of SW620 and HT29 control cells (Empty, blue), Empty cells treated with CHX (grey), and *NLE1* knockout cells (NLE1g1 in orange, NLE1g2 in red) labeled with OPP. MFI levels were normalized to Empty cells and used as a reference (relative MFI=1.0). Two replicates (n = 2) of each cell line are shown [modified from 239]. The reuse of figures was allowed by AACR (Creative Commons CC-BY-NC-ND license).

In addition, we investigated if *NLE1* ablation also reduced *de novo* protein biosynthesis rates in PDTOs reflecting a 3D hierarchy. After the knockout of *NLE1* in PDTO4 S4-KO (Figure 20A), cells were analyzed via Click-iT® Plus OPP Protein Synthesis Assay (Figure 20A, B). PDTOs containing the empty vector were also treated with cycloheximide (similar to cell lines) as a control. During cycloheximide treatment, a substantial reduction in OPP signal could be observed (compared to Empty only). For the *NLE1* knockout derivative NLE1g2, a substantial decrease in the OPP signal was visible,

although the shift was moderate. This may be due to the 3D hierarchy of PDTOs, showing a mixture of cells with high and low protein biosynthesis rates. However, *NLE1* deletion in PDTOs reduces *de novo* protein biosynthesis rates.

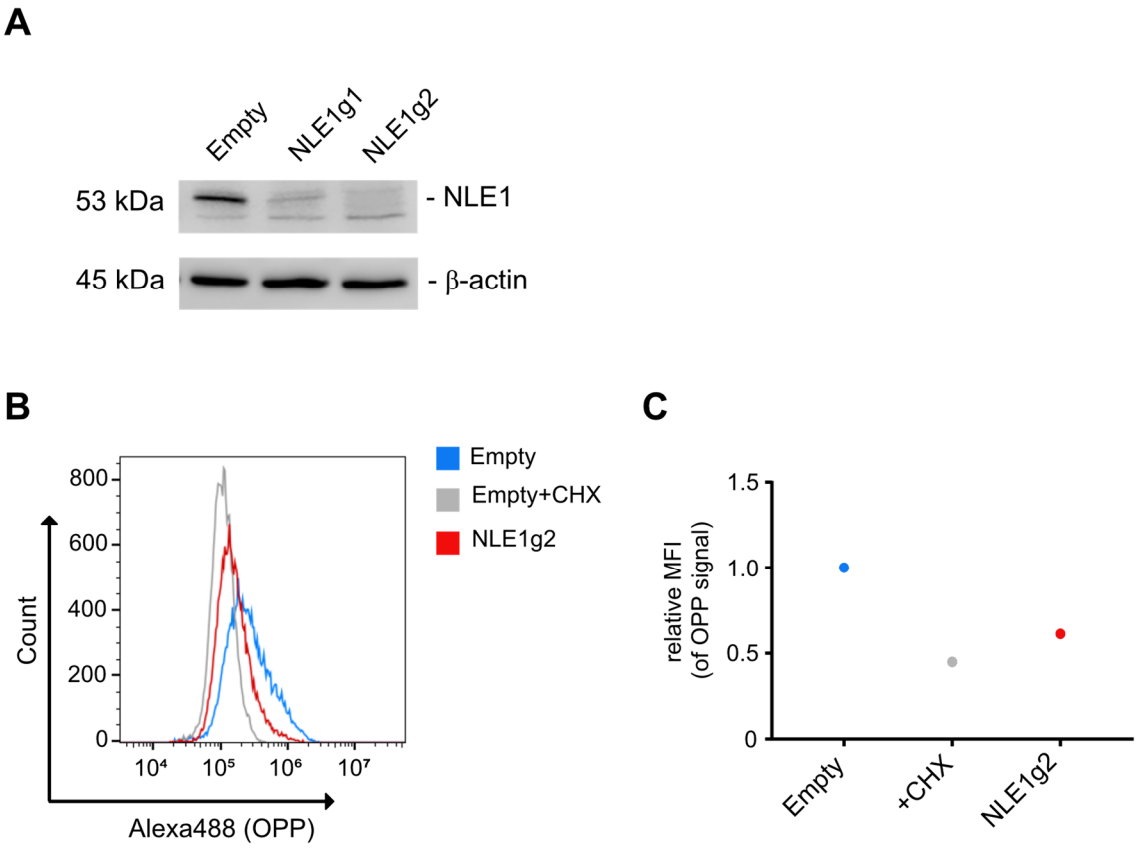

Figure 20: NLE1 is essential for *de novo* protein biosynthesis in PDTOs
A) Protein expression levels of NLE1 in PDTO4 S4-KO cells edited via CRISPR/Cas9 to achieve *NLE1* knockout were detected by immunoblotting. Two different guide RNAs (NLE1g1, NLE1g2) were used. Control cells were transduced with the same vector but without guide RNAs (Empty). Housekeeping protein β-actin was used as a loading control. B) Flow cytometry analysis of OPP incorporation in PDTO4 S4-KO control organoids (Empty, blue), PDTO4 S4-KO Empty organoids treated with cycloheximide (CHX) (grey), and PDTO4 S4-KO *NLE1* knockout organoids (NLE1g2 in red). C) Mean fluorescence intensity (MFI) levels of PDTO4 S4-KO Empty (blue), Empty treated with CHX (grey), and *NLE1* knockout organoids (NLE1g2 in red) labeled with OPP. MFI levels were normalized to Empty cells and used as a reference (relative MFI=1.0) [adjusted from 239]. The reuse of figures was allowed by AACR (Creative Commons CC-BY-NC-ND license).

Taken together, we could show that knockout of *NLE1* leads to reduced *de novo* protein biosynthesis rates in different CRC cell lines and PDTOs.

5.5. Deletion of *NLE1* suppresses proliferation, migration/invasion, and survival of CRC cells

Based on the diminished *de novo* protein biosynthesis rates in *NLE1* knockout cells, we wondered what effect *NLE1* ablation had on proliferation, apoptosis, cell cycle, colony

formation, migration/invasion, and anchorage-independent growth in soft agar in CRC cell lines and PDTOs.

After CRISPR/Cas9-mediated knockout of *NLE1* in SW620 and HT29, the proliferation rate, also called cell index, was investigated (Figure 21A, B). Both cell lines responded with a substantial reduction in cell index for *NLE1* knockout derivatives (NLE1g1 in red, NLE1g2 in blue). Interestingly, SW620 *NLE1* knockout cells showed a slower proliferation rate, whereas HT29 *NLE1* knockout cells showed a complete growth arrest.

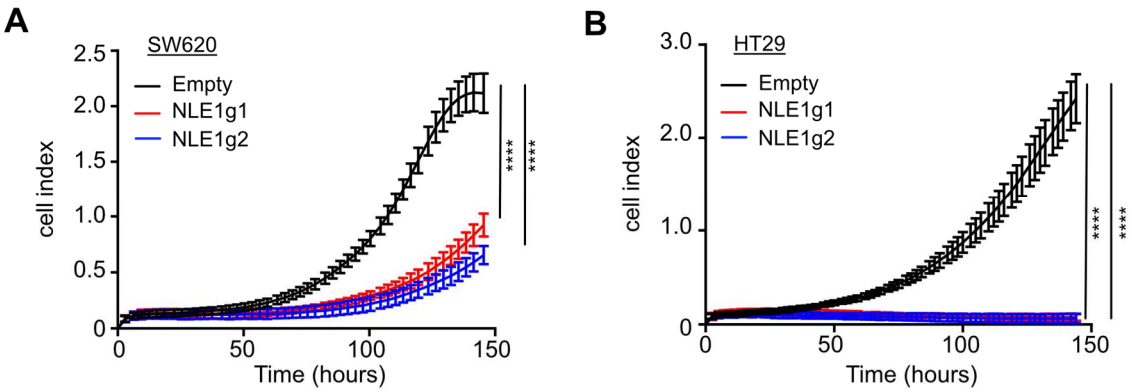

Figure 21: *NLE1* ablation leads to slower proliferation kinetics of CRC cell lines
A) Proliferation kinetics of SW620 Empty (black), NLE1g1 (red), and NLE1g2 (blue) cells were monitored using the xCELLigence system. B) Proliferation kinetics of HT29 Empty (black), NLE1g1 (red), and NLE1g2 (blue) cells were monitored using the xCELLigence system. Asterisks (****: P-value ≤ 0.0001) indicate statistical significance between samples for the latest time point as determined by two-way ANOVA plus Tukey's multiple comparisons test. Data are represented as mean ± SD (n = 8 for SW620, n = 7 for HT29) [adapted from 239]. The reuse of figures was allowed by AACR (Creative Commons CC-BY-NC-ND license).

Next, the colony formation assay was performed to test a single cell's ability to grow into a colony. Therefor, *NLE1* wild-type and knockout derivatives of HT29 and SW620 cells were plated in 6-well plates at a low density and cultured for two weeks. After staining with crystal violet and quantification, we observed a substantial decrease in colony formation efficiency in *NLE1* knockout derivatives (Figure 22A, B). HT29 cells responded stronger than SW620 cells. These results imply that *NLE1* knockout cells are less capable of forming colonies.

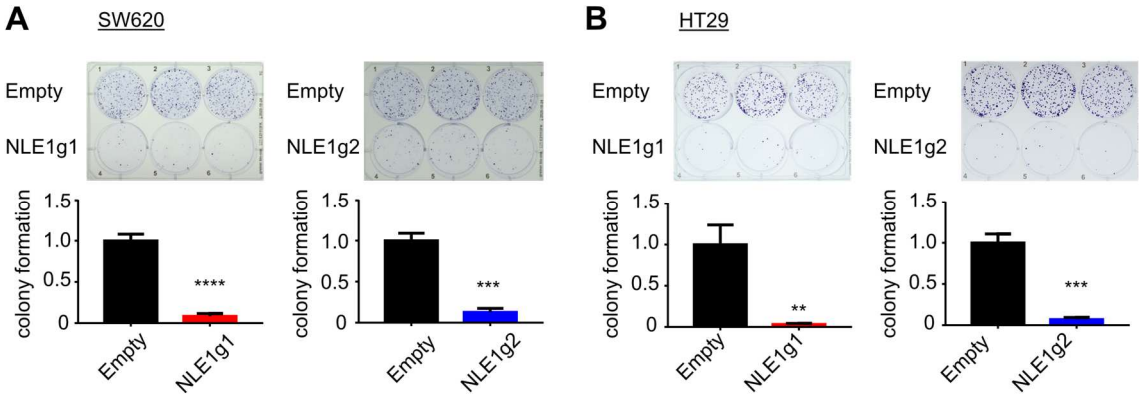

Figure 22: *NLE1* knockout cells are less capable of growing into colonies
A) Colony formation assay was performed in SW620 Empty, NLE1g1, and NLE1g2 cells. Top panel: Representative images from stained culture wells. Bottom panel: Colony formation ratios were calculated and normalized to Empty cells. B) Colony formation assay was performed in HT29 Empty, NLE1g1, and NLE1g2 cells. Top panel: Representative images from stained culture wells. Bottom panel: Colony formation ratios were calculated and normalized to Empty cells. Asterisks (**: P-value ≤ 0.01, ***: P-value ≤ 0.001, ****: P-value ≤ 0.0001) indicate statistical significance between samples as determined by an unpaired t-test. Data are represented as mean ± SD (n = 3) [modified from 239]. The reuse of figures was allowed by AACR (Creative Commons CC-BY-NC-ND license).

To assess whether deletion of *NLE1* influenced anchorage-independent growth, a strong indicator of malignant transformation, HT29 and SW620 wild-type and *NLE1* knockout cells were analyzed via soft agar colony formation assay (Figure 23). For that, a high concentration of agar mixed with medium, the so-called bottom layer, was seeded in 12-well plates. After solidification, the top layer was prepared by mixing a low agar concentration with medium and cells [253]. When the top layer was also solidified, fresh medium was added. Two weeks later, plates were stained with crystal violet and counted. A substantial reduction in the number of colonies in *NLE1* knockout cells was observable. Again, HT29 cells showed a more robust phenotype.

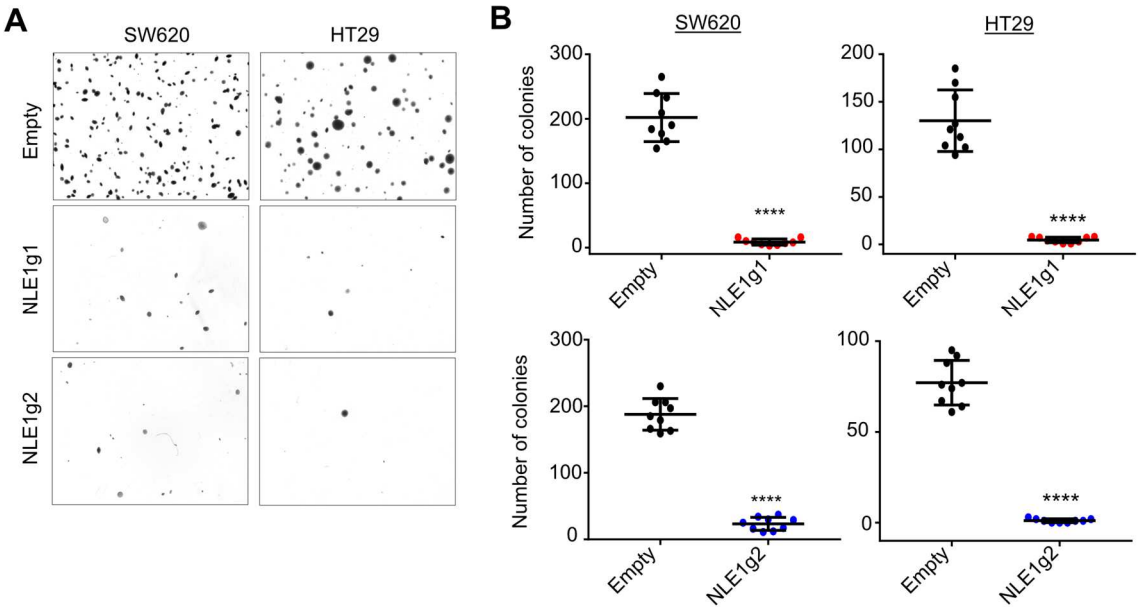

Figure 23: Ablation of *NLE1* impairs anchorage-independent growth of CRC cell lines
Soft agar assay was performed in SW620 and HT29 cells edited via CRISPR/Cas9 to achieve *NLE1* knockout. Two different guide RNAs (NLE1g1, NLE1g2) were used. Control cells were transduced with the same vector but without guide RNAs (Empty). A) Representative images from stained cultures. B) Number of colonies per image (from panel A). Asterisks (****: P-value ≤ 0.0001) indicate statistical significance between samples as determined by an unpaired t-test. Data are represented as mean ± SD (9 images obtained from n = 3 replicates) [adjusted from 239]. The reuse of figures was allowed by AACR (Creative Commons CC-BY-NC-ND license).

We also investigated how the cell cycle was affected in *NLE1* knockout HT29 and SW620 cells. Therefore, we stained the cells' *de novo* synthesized DNA content with the Click-iT™ EdU Alexa Fluor™ 488 Flow Cytometry Assay Kit combined with the FxCycle™ Far Red Stain and analyzed them via flow cytometry. Both cell lines substantially reduced the S-phase (Figure 24). Interestingly, NLE1-deficient HT29 cells responded with an increase in G1-phase, whereas NLE1-deficient SW620 cells responded with an increase in G2/M-phase. This shows that NLE1-deficient cells are blocked during cell cycle progression.

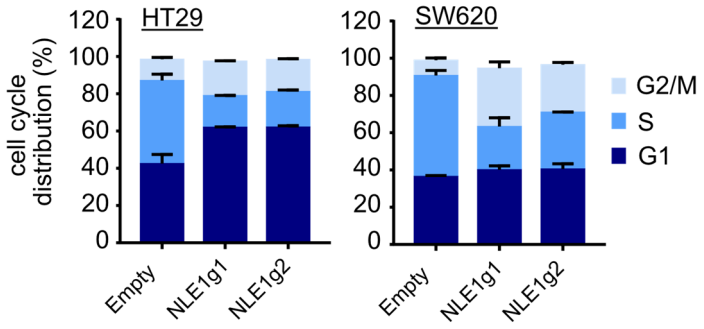

Figure 24: CRC cell lines respond with cell cycle arrest after ablation of *NLE1*
Cell-cycle analysis was performed in SW620 and HT29 cells edited via CRISPR/Cas9 to achieve *NLE1* knockout. Two different guide RNAs (NLE1g1, NLE1g2) were used. Control cells were transduced with the same vector but without guide RNAs (Empty). Left panel: Stacked bar chart showing the percentage of cell-cycle distribution in HT29 Empty, NLE1g1, and NLE1g2 cells. Right panel: Stacked bar chart showing the percentage of cell-cycle distribution in SW620 Empty, NLE1g1, NLE1g2 cells. Data are represented as mean ± SD (n=2) [adapted from 239]. The reuse of figures was allowed by AACR (Creative Commons CC-BY-NC-ND license).

We also determined the effect of *NLE1* ablation on apoptosis. In detail, HT29 and SW620, either wild-type or knockout for *NLE1*, were seeded and examined using the FITC Annexin V Apoptosis Detection Kit I (BD Biosciences). Here, cells are stained with Annexin V and propidium iodide (PI) to distinguish between viable cells (negative for Annexin V/PI), early apoptotic cells (positive for Annexin V/ negative for PI), and late apoptotic cells (positive for Annexin V/PI). We found that *NLE1* ablation in both cell lines led to a 5-fold increase in late apoptosis compared to their controls (Figure 25A), which might at least partially account for their impaired growth. In addition, immunoblot analysis revealed much higher levels of PARP in *NLE1* knockout cells than their wild-type counterparts (Figure 25B).

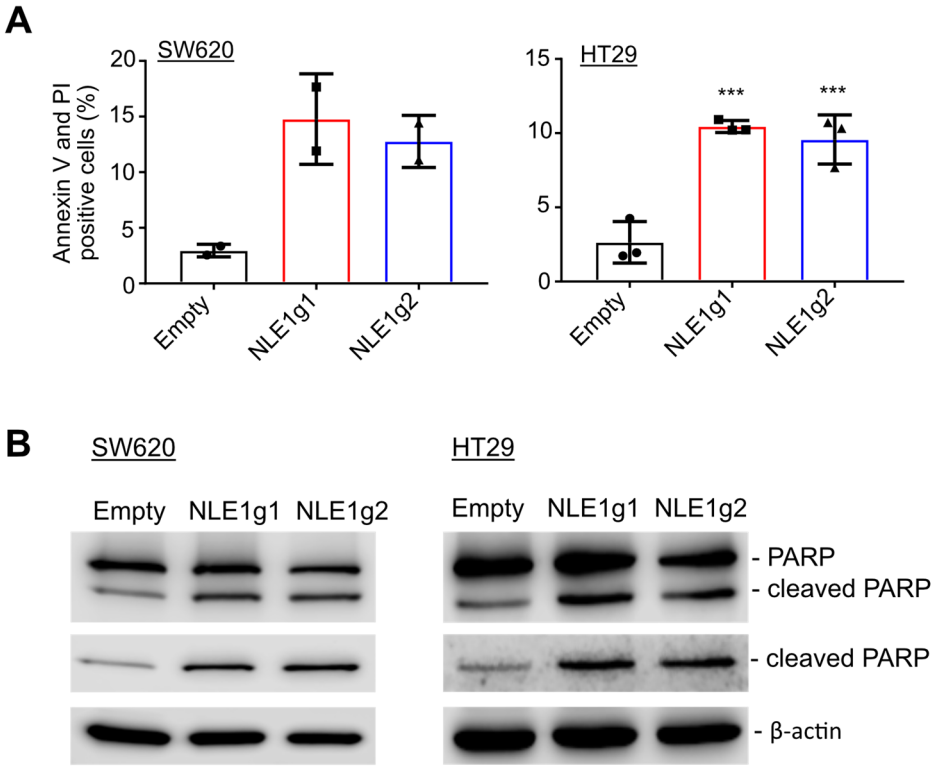

Figure 25: *NLE1* knockout cells are more sensitive undergoing apoptosis
A) Flow cytometry analysis of Annexin-V and propidium iodide (PI) staining in SW620 (left panel) and HT29 (right panel) cells edited via CRISPR/Cas9 to achieve *NLE1* knockout. Two different guide RNAs (NLE1g1, NLE1g2) were used. Control cells were transduced with the same vector but without guide RNAs (Empty). Bar charts show the percentages of Annexin-V and PI double-positive cells. Data are represented as mean ± SD (n=2 for SW620, n=3 for HT29). Asterisks (***: P-value ≤ 0.001) indicate statistical significance between samples in HT29 cells as determined by one-way ANOVA plus Dunnets's multiple comparisons test. B) Protein expression levels of PARP and cleaved PARP in SW620 (left panel) and HT29 (right panel) cells edited via CRISPR/Cas9 to achieve NLE1 knockout were detected by immunoblotting. Two different guide RNAs (NLE1g1, NLE1g2) were used. Control cells were transduced with the same vector but without guide RNAs (Empty). Housekeeping protein β-actin was used as a loading control [modified from 239]. The reuse of figures was allowed by AACR (Creative Commons CC-BY-NC-ND license).

A critical feature of CRC metastasis is the ability of CRC cells to migrate and invade the liver and/or lung tissue. We performed transwell migration and invasion assays to analyze this cellular feature critical for this *in vivo* process in an *in vitro* setting. CRC cell lines were seeded on top of uncoated (migration) and Matrigel®-coated (invasion) transwell membranes and 48 hours later fixed and stained for quantification. Both cell lines showed a substantial reduction in the migration and invasion capacity of *NLE1* knockout cells *in vitro* (Figure 26). Therefore, we hypothesize that the knockout of *NLE1* may reduce the metastatic capability of CRC cells.

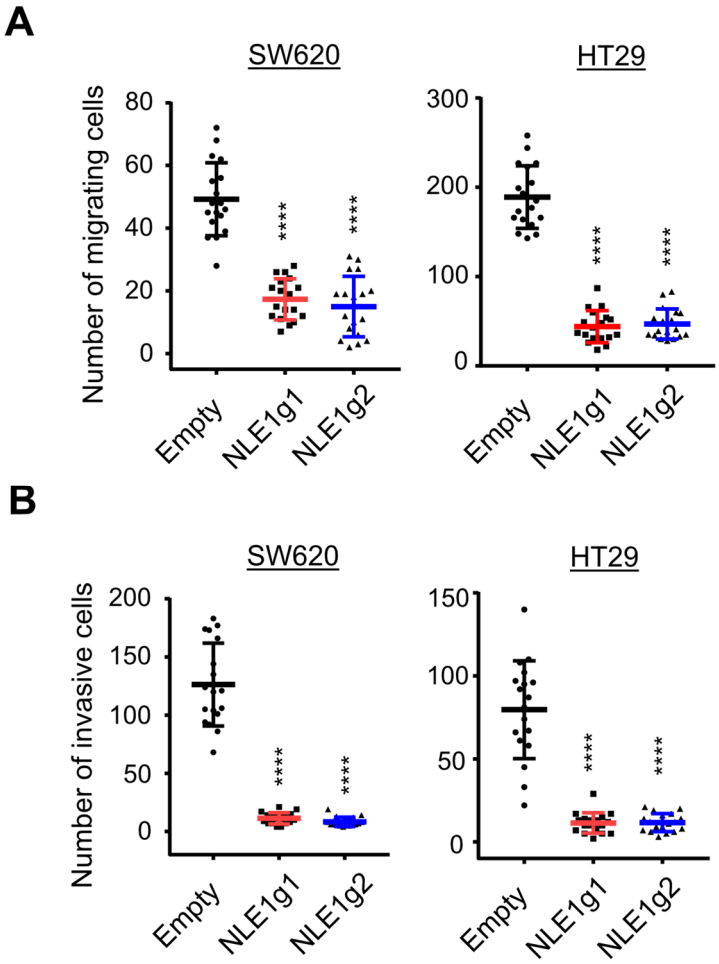

Figure 26: Loss of NLE1 inhibits migration and invasion in CRC cell lines
A) Transwell migration assay (uncoated membrane) was performed in SW620 (left panel) and HT29 (right panel) cells edited via CRISPR/Cas9 to achieve *NLE1* knockout. Two different guide RNAs (NLE1g1, NLE1g2) were used. Control cells were transduced with the same vector but without guide RNAs (Empty). Grouped dot plot shows the number of migrating cells. Data are represented as mean ± SD (18 pictures obtained from n = 6 replicates. B) Transwell invasion assay (Matrigel®-coated membrane) was performed in SW620 (left panel) and HT29 (right panel) cells edited via CRISPR/Cas9 to achieve *NLE1* knockout. Two different guide RNAs (NLE1g1, NLE1g2) were used. Control cells were transduced with the same vector but without guide RNAs (Empty). Grouped dot plot shows the number of invasive cells. Data are represented as mean ± SD (18 pictures obtained from n = 6 replicates). Asterisks (****: P-value ≤ 0.0001) indicate statistical significance between samples in A and B as determined by one-way ANOVA plus Dunnets's multiple comparison test [adjusted from 239]. The reuse of figures was allowed by AACR (Creative Commons CC-BY-NC-ND license).

To test whether *NLE1* ablation affected organoid size and re-seeding capacity, we performed CRISPR/Cas9-mediated *NLE1* knockout in two different *SMAD4* knockout lines (Figure 27, Figure 28). In both lines, PDTO2 S4 and PDTO4 S4, a shift towards smaller diameter PDTOs could be observed (Figure 27B, Figure 28C). In addition, after seeding the same cell number of control (Empty) and *NLE1* knockout (NLE1g1, NLE1g2) cells, *NLE1* knockout cells showed a decreased organoid formation capacity (Figure 27C, Figure 28D). Overall, the effect in three-dimensional cultured PDTOs seemed less pronounced compared to two-dimensional cultured CRC cell lines.

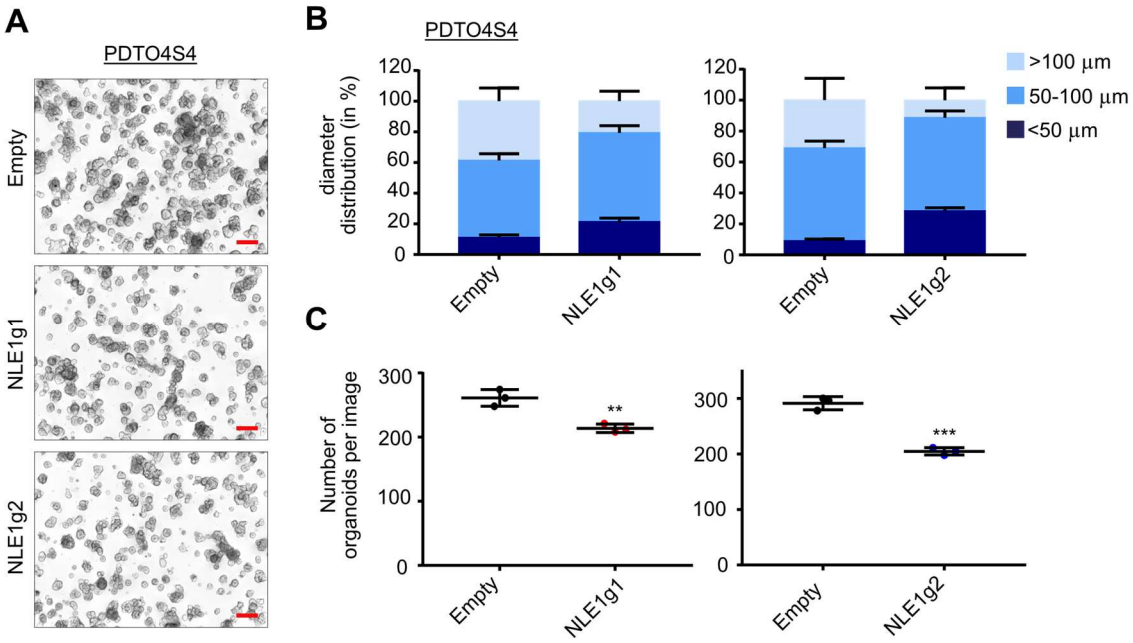

Figure 27: *NLE1* ablation reduces organoid size and clonogenicity in PDTO4 S4
A) Enhanced focal images of PDTO4 S4-KO organoids edited via CRISPR/Cas9 to achieve *NLE1* knockout. Two different guide RNAs (NLE1g1, NLE1g2) were used. Control cells were transduced with the same vector but without guide RNAs (Empty). Images were obtained 7 days after plating in 3-D Matrigel®. The scale bar represents 200 µm. B) Diameter distributions (in percent) of PDTO4 S4-KO Empty, NLE1g1, and NLE1g2 organoids were analyzed. n = 300 organoids per genotype (n = 100 in three different Matrigel® droplets) were measured and classified into three groups based on organoid diameter: less than 50 µm, between 50 and 100 µm, and bigger than 100 µm. Data are represented as a stacked bar chart. C) A grouped dot plot shows the number of PDTO4 S4-KO Empty, NLE1g1, and NLE1g2 organoids per image. Asterisks (**: P-value ≤ 0.01, ***: P-value ≤ 0.001) indicate statistical significance as determined by an unpaired t-test. Data are represented as mean ± SD (n = 3) [adapted from 239]. The reuse of figures was allowed by AACR (Creative Commons CC-BY-NC-ND license).

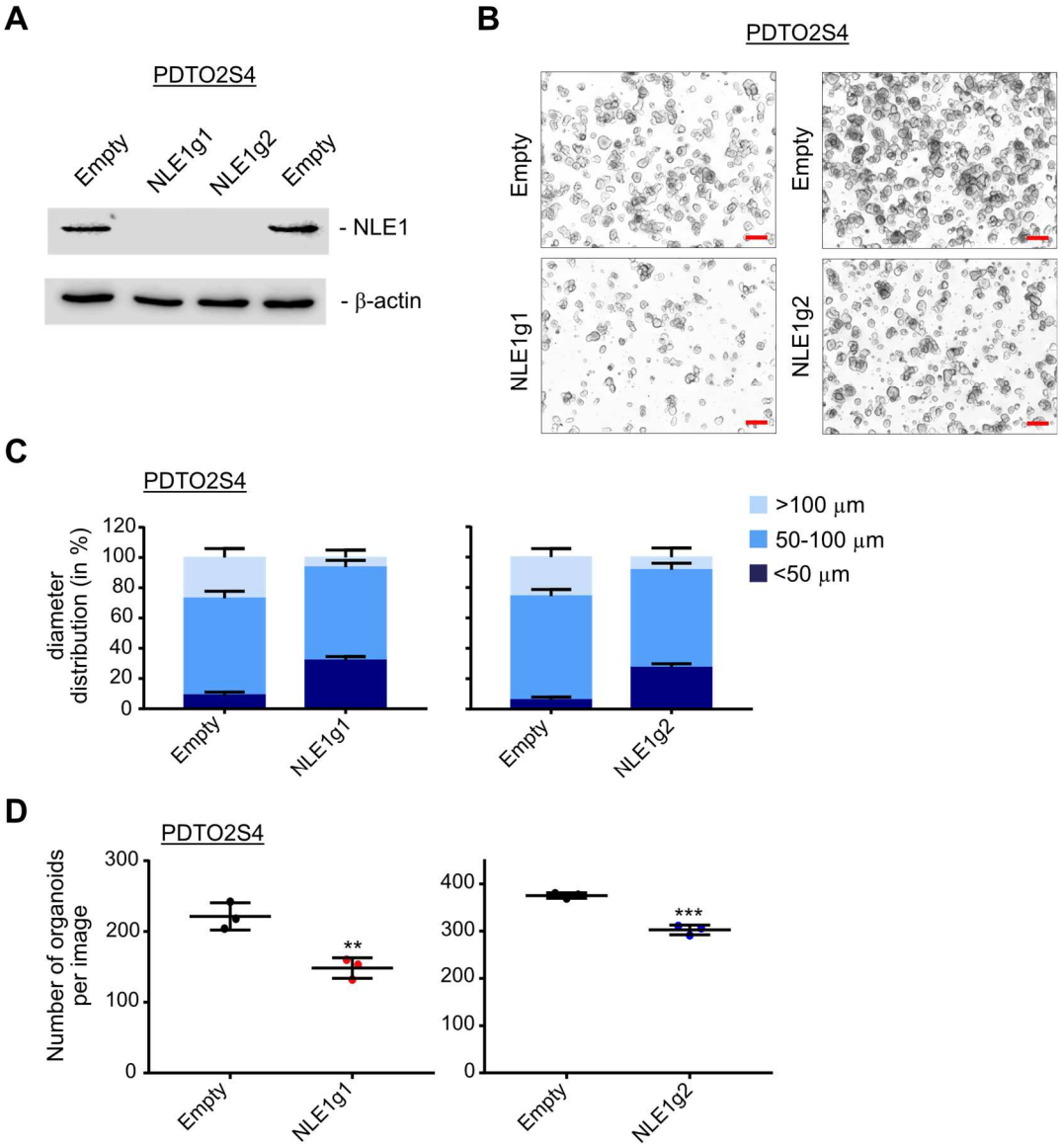

Figure 28: *NLE1* ablation reduces organoid size and clonogenicity in PDTO2 S4
A) Protein expression levels of NLE1 in PDTO2 S4-KO organoids edited via CRISPR/Cas9 to achieve *NLE1* knockout were detected by immunoblotting. Two different guide RNAs (NLE1g1, NLE1g2) were used. Control cells were transduced with the same vector but without guide RNAs (Empty). Housekeeping protein β-actin was used as a loading control. B) Enhanced focal images of PDTO2 S4-KO Empty, NLE1g1, and NLE1g2 organoids. Images were obtained 7 days after plating in 3-D Matrigel®. The scale bar represents 200 µm. C) Diameter distributions (in percent) of PDTO2 S4-KO Empty, NLE1g1, and NLE1g2 organoids were analyzed. n = 300 organoids per genotype (n = 100 in three different Matrigel® droplets) were measured and classified into three groups based on organoid diameter: less than 50 µm, between 50 and 100 µm, and bigger than 100 µm. Data are represented as a stacked bar chart. D) Number of PDTO2 S4-KO Empty, NLE1g1, and NLE1g2 organoids per image is shown in a grouped dot plot. Asterisks (**: P-value ≤ 0.01, ***: P-value ≤ 0.001) indicate statistical significance as determined by an unpaired t-test. Data are represented as mean ± SD (n = 3) [modified from 239]. The reuse of figures was allowed by AACR (Creative Commons CC-BY-NC-ND license).

After having observed these strong effects in our loss of function studies, we decided to complement our data with gain of function studies. Hence, a doxycycline-inducible overexpression vector of *NLE1* was generated and investigated in a normal human colonic cell line (HCEC-1CT) and one tumor organoid line (PDTO4) (Figure 29).

Immunoblot analysis in both lines with doxycycline showed successful overexpression of ectopic NLE1 (Figure 29A, C). No differences were observed when seeding cells and organoids for proliferation curves permanently kept in the presence of doxycycline (Figure 29B, D). This shows that overexpression of NLE1 alone does not augment proliferation in normal colon cells or PDTOs.

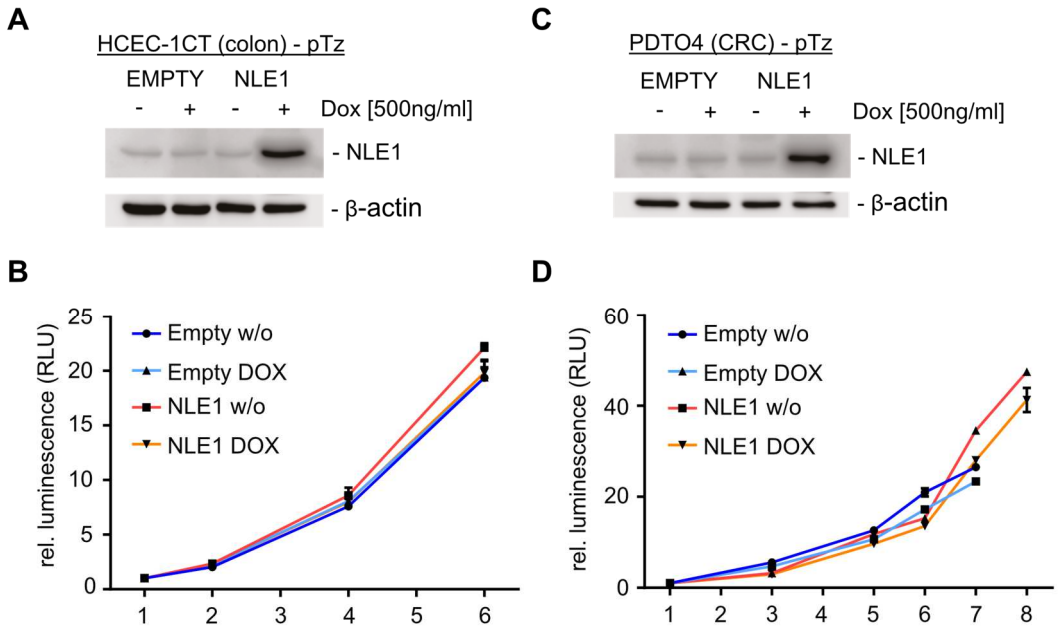

Figure 29: Overexpression of NLE1 does not promote proliferation in immortalized human colonic epithelial cells (HCEC-1CT) and PDTOs
A) Protein expression levels of NLE1 in immortalized human colonic epithelial cells (HCEC-1CT) stably transduced with lentiviral particles encoding for a doxycycline-inducible *NLE1* allele (pTz-NLE1) or with a control virus (pTz-Empty) were detected by immunoblotting. Housekeeping protein β-actin was used as a loading control. B) Proliferation curves of stably transduced HCEC-1CT cells from panel A as determined by measuring the ATP content at the indicated time points. Cells were either left untreated or treated with doxycycline (DOX). Data were normalized to day 1 and are represented as mean ± SD (n = 3). C) Protein expression levels of NLE1 in PDTO4 organoids stably transduced with lentiviral particles encoding for a doxycycline-inducible *NLE1* allele (pTz-NLE1) or with a control virus (pTz-Empty) were detected by immunoblotting. Housekeeping protein β-actin was used as a loading control. D) Proliferation curves of stably transduced PDTO4 organoids from panel C as determined by measuring the ATP content at the indicated time points. Cells were either left untreated or treated with doxycycline (DOX). Data were normalized to day 1 and are represented as mean ± SD (n = 3) [adjusted from 239]. The reuse of figures was allowed by AACR (Creative Commons CC-BY-NC-ND license).

Moreover, we wondered if overexpression of NLE1 also affects *de novo* protein biosynthesis. Hence, we measured OPP incorporation via flow cytometry in HCEC-1CT cells overexpressing NLE1 (Figure 30). Here we could not observe an induction in the OPP signal, which fits the proliferation curves from figure 29. Hence, elevated expression of NLE1 alone cannot augment *de novo* protein biosynthesis in normal colon cells or PDTOs.

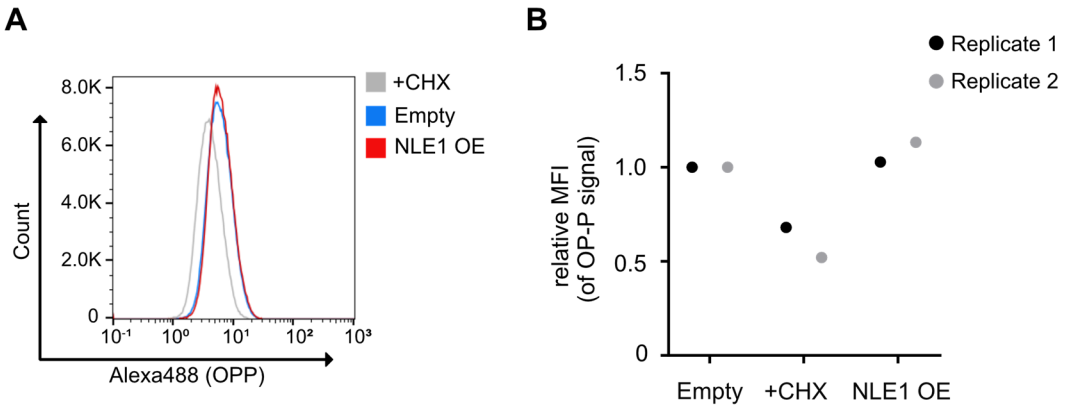

Figure 30: Overexpression of NLE1 does not induce *de novo* protein biosynthesis in immortalized human colonic epithelial cells (HCEC-1CT)
A) Flow cytometry analysis of OPP incorporation in HCEC-1CT pTz-Empty cells (Empty, blue), HCEC-1CT pTz-Empty cells treated with cycloheximide (+CHX, grey), and HCEC-1CT pTz-NLE1 conditionally overexpressing NLE1 cells (NLE1 OE, red). Before analysis, cells were treated with 500 ng/ml doxycycline (DOX) for 96 hours. B) Mean fluorescence intensity (MFI) levels of HCEC-1CT pTz-Empty cells (Empty), HCEC-1CT pTz-Empty cells treated with cycloheximide (+CHX), and HCEC-1CT pTz-NLE1 conditionally overexpressing NLE1 cells (NLE1 OE) labeled with OPP. MFI levels were normalized to Empty cells and used as a reference (relative MFI=1.0). Two replicates (n = 2) are shown [adapted from 239]. The reuse of figures was allowed by AACR (Creative Commons CC-BY-NC-ND license).

To investigate if ectopic expression of NLE1 could rescue the growth-inhibitory effect of recombinant TGF-β on PDTOs, the PDTO4 (*SMAD4* wild-type) organoids stably transduced with the conditional NLE1 overexpression were seeded in TOC medium with four different conditions: 1. without TGF-β/doxycycline (control), 2. with TGF-ß and without doxycycline, 3. with TGF-ß and with doxycycline, 4. without TGF-β but with doxycycline (Figure 31). As previously described, PDTO4 responded nicely with growth inhibition under TGF-β treatment. When cells were additionally treated with doxycycline to overexpress NLE1 under TGF-ß treatment, no difference was observable to the TGF-β only treated cells. Cells treated with doxycycline showed no decrease in cell viability, proofing that the here used doxycycline concentration had no toxic effect on cell viability. These results show that NLE1 alone cannot rescue the growth-inhibitory effect of recombinant TGF-β1 on PDTOs.

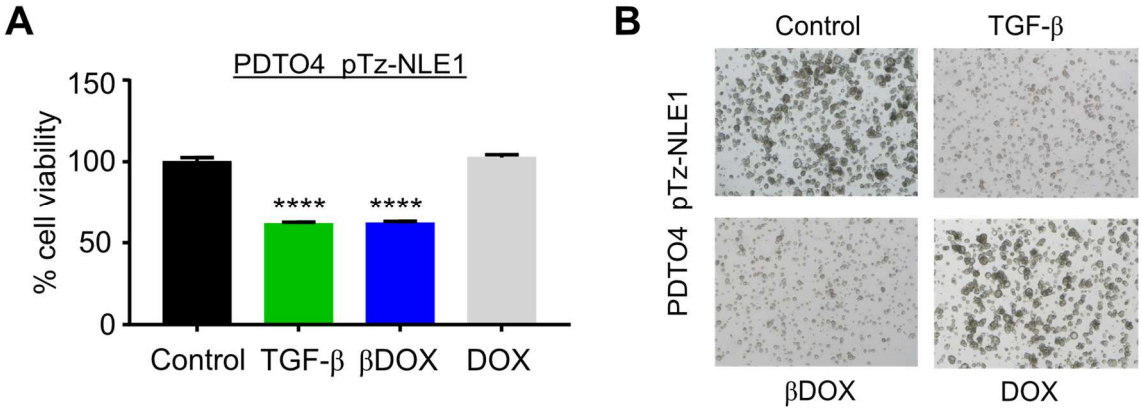

Figure 31: Overexpression of NLE1 cannot rescue TGF-β mediated growth arrest in PDTOs
A) Cell viability of PDTO4 pTz-NLE1 organoids was analyzed 9 days after seeding by measuring the ATP content. Organoids were cultured in different media conditions: TOC medium alone (Control), TOC medium supplemented with 20 ng/ml TGF-β (TGF-β), TOC medium supplemented with 20 ng/ml TGF-β and 500 ng/ml doxycycline (βDOX), and TOC medium supplemented with 500 ng/ml doxycycline (DOX). Data are represented as mean ± SD (n = 4 replicates). B) Enhanced focal images of PDTO4 pTz-NLE1 organoids 9 days after seeding in the indicated media from panel A [modified from 239]. The reuse of figures was allowed by AACR (Creative Commons CC-BY-NC-ND license).

In conclusion, loss of NLE1 limits *de novo* protein biosynthesis and diminishes the growth, clonogenicity, migration/invasion, and survival of CRC cells *in vitro*. In contrast, overexpression of NLE1 alone could not augment growth and *de novo* protein biosynthesis, suggesting that other factors besides NLE1 are also required to induce proliferation and *de novo* protein biosynthesis in normal colon cells. Moreover, TGF-β-mediated growth inhibition of PDTOs could not be rescued by overexpressing NLE1.

5.6. NLE1 deficiency causes p38/MAPK-phosphorylation, impaired autophagy, and increased ROS levels in CRC cells

Previous studies showed that drugs such as doxorubicin or cycloheximide, efficiently inhibiting protein biosynthesis, can provoke ribotoxic stress responses (RSR) by activating p38/MAPK and JNK signaling and thereby causing apoptotic cell death [254, 255]. Since NLE1 is part of the ribosomal machinery, we decided to elucidate if the above signaling pathways could be responsible for our observed phenotype. Indeed, immunoblot analysis of the p38/MAPK and JNK signaling pathway components revealed phosphorylation of p38/MAPK (Thr180/Tyr182) in *NLE1* knockout CRC cell lines (Figure 32). In contrast, JNK was not phosphorylated.

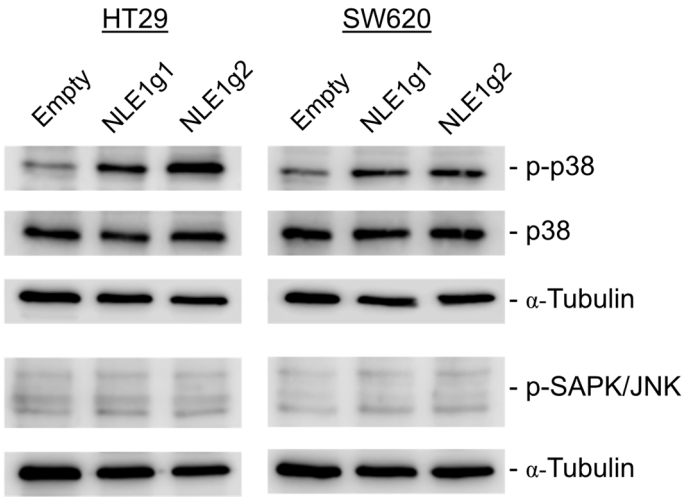

Figure 32: NLE1 deficiency causes activation of p38/MAPK but not JNK signaling in CRC cell lines
Protein expression levels of p38/MAPK, phospho-p38 (p-38), and phospho-SAPK/JNK in HT29 (left panel) and SW620 (right panel) cells edited via CRISPR/Cas9 to achieve *NLE1* knockout were detected by immunoblotting. Two different guide RNAs (NLE1g1, NLE1g2) were used. Control cells were transduced with the same vector but without guide RNAs (Empty). Housekeeping protein α-tubulin was used as a loading control [adjusted from 239]. The reuse of figures was allowed by AACR (Creative Commons CC-BY-NC-ND license).

Since we had observed activation of p38/MAPK signaling and a higher fraction of apoptotic cells in *NLE1* knockout derivatives, and it is well known that p38/MAPK signaling controls the balance of autophagy and apoptosis in response to cellular stress in cancer cells, we decided to investigate if autophagy was also affected [256]. Therefore, we performed immunofluorescence microscopy and immunoblot analysis in *NLE1* knockout SW620 and HT29 cells (Figure 34). *NLE1* knockout cells displayed elevated levels of the autophagy receptor and substrate p62/sequestosome 1 (SQSTM1) and higher levels of the autophagosomal marker microtubule-associated protein 1 light chain 3 beta (LC3B) (Figure 33A). In addition, staining of LC3B for immunofluorescence microscopy revealed an overall increase in the number and area of LC3B positive subcellular structures (Figure 33B) [256, 257]. As a positive control for a state of compromised autophagy, Empty cells were treated with chloroquine (CQ), an autophagy inhibitor blocking the autophagolysosome formation and thereby provoking an increase in LC3B positive subcellular structures [257, 258]. The treated control cells showed the same effects as *NLE1* knockout cells but were even more robust.

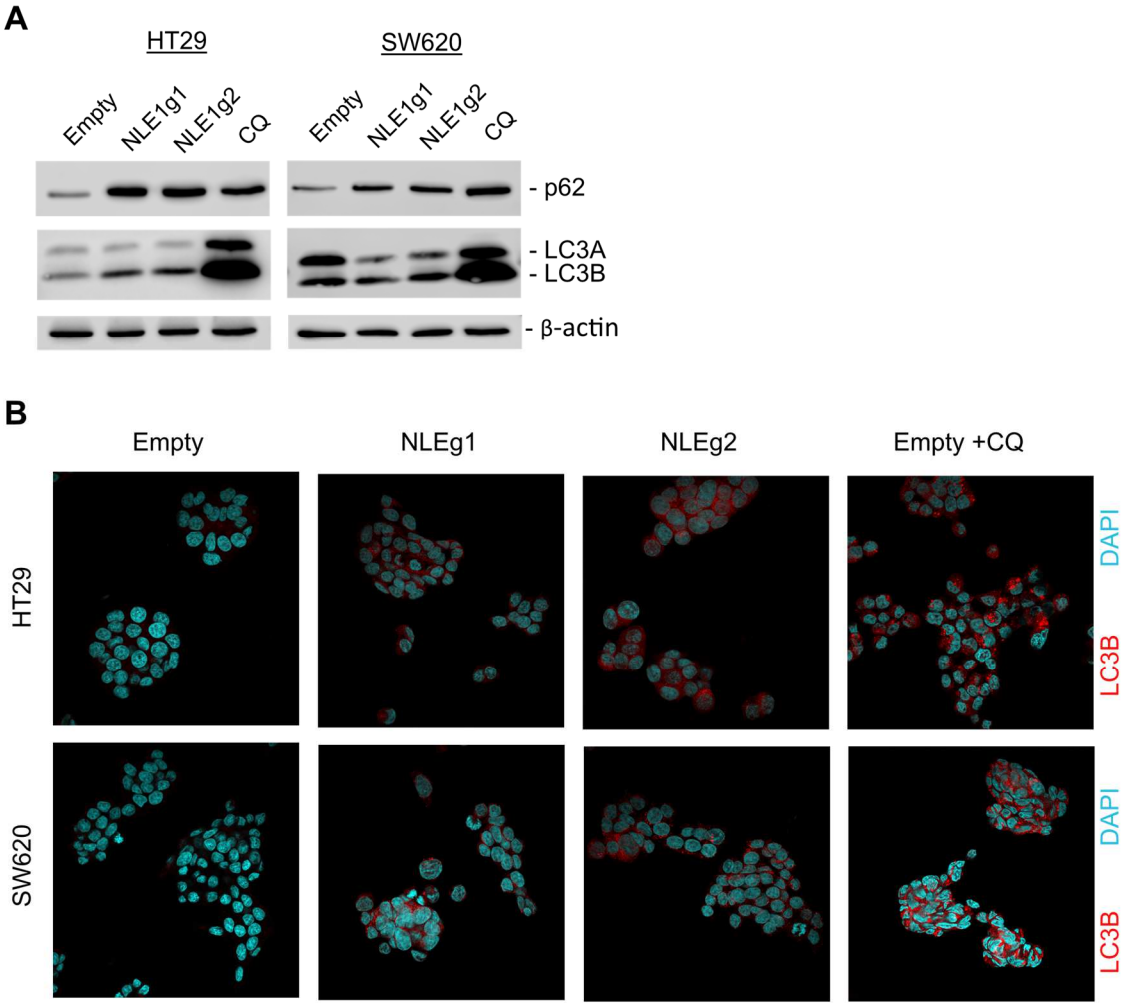

Figure 33: Ablation of *NLE1* leads to impaired autophagy in CRC cell lines
A) Protein expression levels of the autophagy receptor protein p62 and autophagosome proteins LC3A/B in HT29 (left panel) and SW620 (right panel) cells edited via CRISPR/Cas9 to achieve *NLE1* knockout were detected by immunoblotting. Two different guide RNAs (NLE1g1, NLE1g2) were used. Control cells were transduced with the same vector but without guide RNAs (Empty). As a positive control for impaired autophagy, cells were treated with 50 µM chloroquine (CQ), an autophagy inhibitor, 24 hours before analysis. Housekeeping protein β-actin was used as a loading control. B) Representative immunofluorescence images showing LC3B staining (red signal) in *NLE1* wild-type (Empty) and *NLE1* knockout (NLE1g1 and NLE1g2) HT29 and SW620 cells. As a positive control for impaired autophagy, cells were treated with 50 µM chloroquine (CQ), an autophagy inhibitor, 24 hours before analysis [adapted from 239]. The reuse of figures was allowed by AACR (Creative Commons CC-BY-NC-ND license).

Since previous literature described a connection between impaired autophagy, elevated ROS level, and apoptosis, we investigated if *NLE1* knockout cells showed different levels of reactive oxygen species (ROS) [259, 260]. *NLE1* wild-type and *NLE1* knockout cells were labeled with CellROX® Green Flow Cytometry Assay Kit and analyzed via flow cytometry. The CellROX® Green reagent is cell-permeable and non-fluorescent while in a reduced state. When oxidized, a strong fluorogenic signal can be measured with flow cytometry (see Materials and Methods). As a positive control for ROS induction, *NLE1* wild-type cells were treated with tert-butyl hydroperoxide (+THBP) 1 hour before analysis [261, 262]. A clear shift in the FITC signal was observable (Figure 34A).

Interestingly, ROS levels in *NLE1* knockout cells were also increased but to a lower extent (Figure 34A, B). Still, HT29 cells showed an even stronger phenotype than SW620 cells. These data fit the previous observations of p38/MAPK activation and impaired autophagy during NLE1 loss.

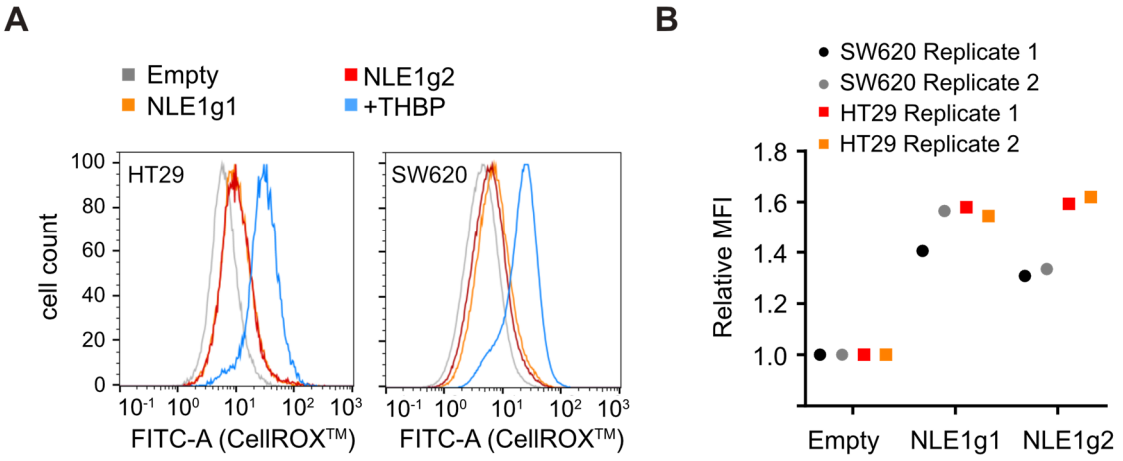

Figure 34: Reactive oxygen species are increased in *NLE1* knockout CRC cell lines
A) Flow cytometry analysis of reactive oxygen species (ROS) generation in HT29 (left panel) and SW620 (right panel) cells edited via CRISPR/Cas9 to achieve *NLE1* knockout. Two different guide RNAs (NLE1g1, NLE1g2) were used. Control cells were transduced with the same vector but without guide RNAs (Empty). One hour before analysis, cells were treated with the ROS-inducing agent tert-butyl hydroperoxide (+THBP) as a positive control. Histograms illustrate cell count (normalized to mode) at different fluorescence intensities originating from ROS-oxidized CellROX™ Green Reagent. B) Mean fluorescence intensity (MFI) levels of HT29 and SW620 control cells (Empty) and *NLE1* knockout cells (NLE1g1 and NLE1g2) labeled with ROS-oxidized CellROX™ Green Reagent. MFI levels were normalized to Empty cells and used as a reference (relative MFI=1.0). Two replicates (n = 2) of each cell line are shown [modified from 239]. The reuse of figures was allowed by AACR (Creative Commons CC-BY-NC-ND license).

Collectively, these results show that loss of NLE1 leads to activation of p38/MAPK signaling, impaired autophagy, and higher ROS levels in CRC cell lines. However, future studies must address how and if these molecular events triggered by NLE1 loss are responsible for reduced tumor cellular fitness and lead to higher apoptosis levels.

5.7. Knockout of *NLE1* reduces tumor burden and metastasis in an orthotopic mouse transplantation model

To elucidate if NLE1 is also an essential factor for CRC growth and distant metastasis *in vivo*, the ablation of *NLE1* in an endoscopy-guided orthotopic transplantation model was investigated. Therefore, a highly aggressive human CRC organoid line that efficiently provokes liver metastasis (CRC-R7, kindly provided by Moritz Jesinghaus, Technical University of Munich, TUM) was genetically modified via CRISPR/Cas9 to delete *NLE1*. After selection with puromycin, *NLE1* wild-type and *NLE1* knockout tumor organoids were prepared for transplantation into NSG mice. These genetically engineered mice are

immunodeficient and lack B cells, Natural killer cells (NK cells), and mature T cells [263, 264]. In preparation for transplantation, tumor organoids were quantified by microscopy and then released from Matrigel®. The ATP content of the different organoid suspensions was also determined to perform an additional normalization. Finally, 150 viable organoids were injected per injection site, with 1-2 submucosal injections per animal. Only mice that fulfilled our quality criteria for injections were used for further analysis. An overview of the experimental setup is shown in figure 35.

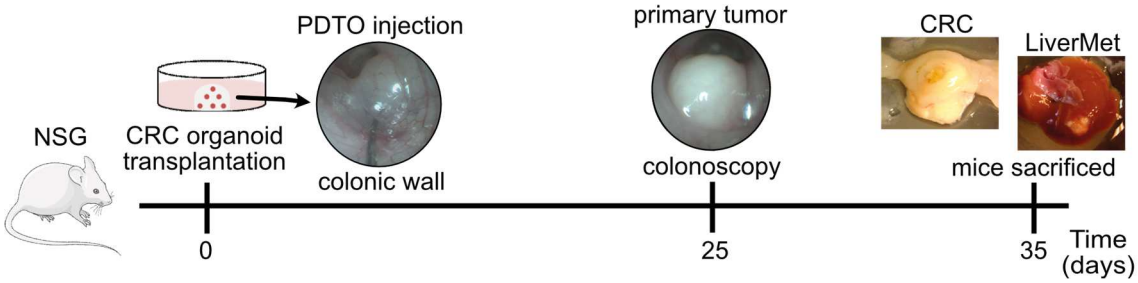

Figure 35: Timeline and schematic overview of endoscopy-guided orthotopic transplantation model
On day 0, the process of PDTO needle injection seen via an endoscopic camera is shown while the injection bubble is about to form. A control endoscopy was conducted on day 25 to control for the presence and size of primary tumors and to estimate the experimental endpoint when mice should be sacrificed due to excessive tumor burden. Thirty-five days after orthotopic transplantation of PDTOs, mice were sacrificed. Colon tumors were scored, and livers were examined for macroscopically visible metastatic foci [adjusted from 239]. Reuse of the figure was allowed by AACR (Creative Commons CC-BY-NC-ND license).

Twenty-five days after transplantation, two mice with *NLE1* wild-type transplanted tumor organoids, and two mice with *NLE1* knockout transplanted tumor organoids were investigated by colonoscopy. A massive tumor formation could be observed in both *NLE1* wild-type PDTO transplanted mice, whereas, in both *NLE1* knockout PDTO transplanted mice, a notably smaller tumor was visible (Figure 36).

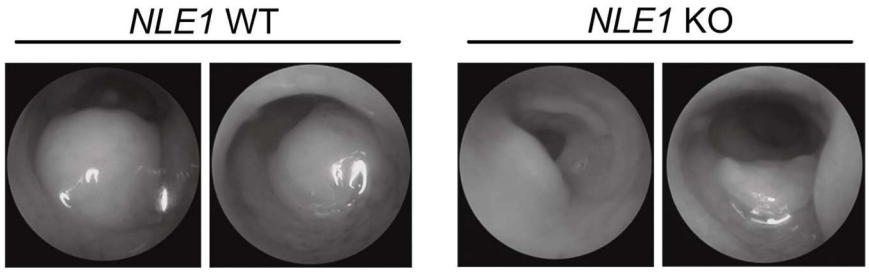

Figure 36: Colonoscopy follow-up after orthotopic transplantation of *NLE1* wild-type (WT) and *NLE1* knockout (KO) organoids in immunodeficient mice
Twenty-five days after orthotopic transplantation of *NLE1* wild-type (WT) or *NLE1* knockout (KO) PDTOs into the colonic wall of immunodeficient mice, a control endoscopy was conducted. *NLE1* WT tumors showed a more pronounced protrusion into the colonic lumen than those grown from *NLE1* KO PDTOs [adapted from 239]. Reuse of the figure was allowed by AACR (Creative Commons CC-BY-NC-ND license).

On day 35, three out of four *NLE1* wild-type PDTO transplanted mice showed non-tolerable weight loss. Since we aimed to compare tumor and metastasis burden between genotypes at the same time point after the initial transplantation of organoids, we sacrificed all animals. As expected, *NLE1* wild-type PDTOs had formed larger primary tumors than their *NLE1* knockout derivatives (Figure 37A, B).

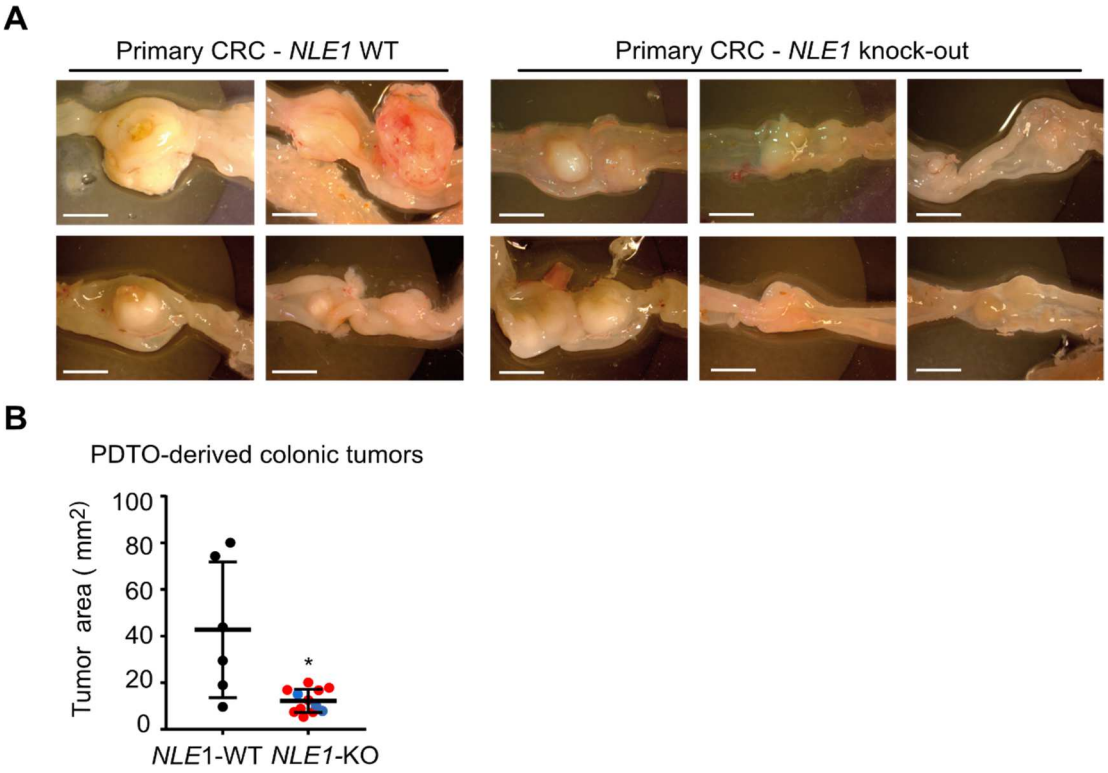

Figure 37: Knockout of *NLE1* in CRC organoids reduces tumor burden *in vivo*
A) Macroscopic pictures of primary tumors grown in the colon of immunodeficient mice after orthotopic transplantation with *NLE1* wild-type (WT) PDTOs or *NLE1* knockout (KO) PDTOs. Five weeks after xenotransplantation, all mice were sacrificed for analysis. The scale bar represents 0.5 cm. B) Tumor area of primary tumors grown in the colon of xenotransplanted mice were analyzed. *NLE1* wild-type (WT, black) PDTOs had been transplanted into four mice (n = 6 primary tumors), and *NLE1* knockout (KO, NLE1g1 in red, NLE1g2 in blue) PDTOs had been transplanted into six mice (n = 12 primary tumors). Five weeks after xenotransplantation, all mice were sacrificed for analysis. Asterisks (* P-value < 0.05) indicate statistical significance between the *NLE1*-WT and *NLE1*-KO groups as determined by an unpaired t-test plus Welch's correction. Welch's correction was applied due to unequal SDs within the two groups. Data are represented as mean ± SD [modified from 239]. The reuse of figures was allowed by AACR (Creative Commons CC-BY-NC-ND license).

To investigate whether the smaller tumors in the *NLE1* knockout transplanted mice arose from more slowly proliferating cells, tissue sections of all mice were stained for MKI67 via immunohistochemistry. MKI67 is a well-known marker for proliferation and often correlates with the clinical course of cancer [265, 266]. Indeed, *NLE1* wild-type derived tumors showed a higher fraction of MKI67+ cells than *NLE1* knockout tumors (Figure 38A, B).

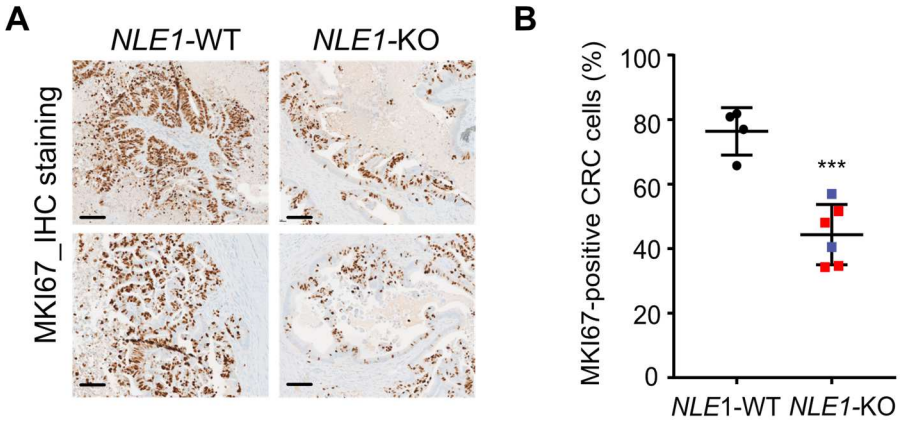

Figure 38: *NLE1* wild-type tumors show a higher fraction of MKI67+ cells compared to *NLE1* knockout tumors
A) Representative MKI67 immunohistochemistry on FPPE tissue slices generated from *NLE1* wild-type (WT) and *NLE1* knockout (KO) PDTO-derived primary tumors. The scale bar represents 100 µm. B) MKI67-positive tumor cells (in %) were quantified in FFPE tissue slices from *NLE1* wild-type (WT, n = 4) and *NLE1* knockout (KO, n = 6) primary tumors. Asterisks (*** P-value < 0.001) indicate statistical significance between groups as determined by an unpaired t-test. Data are represented as mean ± SD [adjusted from 239]. The reuse of figures was allowed by AACR (Creative Commons CC-BY-NC-ND license).

Furthermore, we wondered if a higher apoptosis level in *NLE1* knockout tumors *in vivo* could be observed as we already observed for *NLE1* knockout CRC cell lines *in vitro*. FFPE tissue sections of both genotypes were stained for cleaved caspase 3 via immunohistochemistry. In detail, "[…] caspase [3] is responsible for the majority of proteolysis during apoptosis, and detection of cleaved caspase 3 is therefore considered a reliable marker for cells that are dying or have died by apoptosis" [267]. Immunohistochemistry of cleaved caspase 3 in *NLE1* wild-type and *NLE1* knockout tumors revealed an overall elevated abundance of cleaved caspase 3 in *NLE1* knockout tumors (Figure 39).

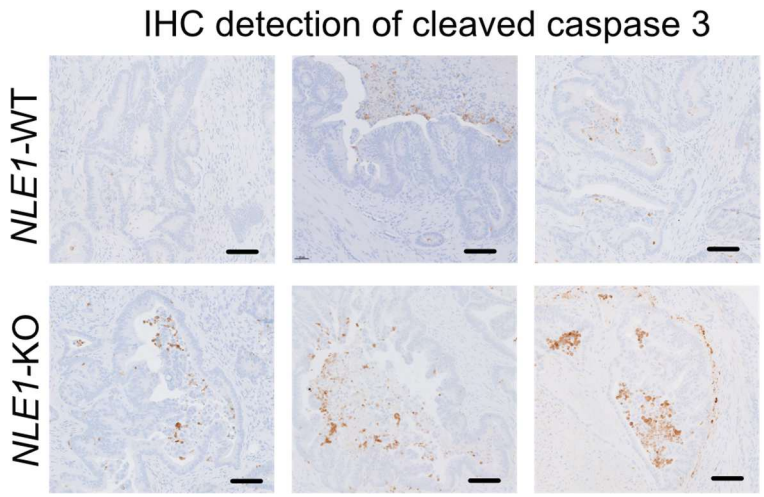

Figure 39: *NLE1* knockout tumors show higher cleaved caspase 3 levels than *NLE1* wild-type tumors
Representative cleaved caspase 3 immunohistochemistry on FPPE tissue slices generated from *NLE1* wild-type (WT) and *NLE1* knockout (KO) PDTO-derived primary tumors. The scale bar represents 100 µm [adapted from 239]. Reuse of the figure was allowed by AACR (Creative Commons CC-BY-NC-ND license).

Next, the liver metastatic burden of *NLE1* wild-type and *NLE1* knockout PDTO transplanted mice was investigated (Figure 40). In all *NLE1* wild-type PDTO transplanted mice, 4-5 liver metastasis were macroscopically visible. However, only 2 out of 6 mice in *NLE1* knockout PDTO transplanted mice showed 3 or 4 metastatic lesions. 4 out of 6 mice had formed none or only one metastatic lesion.

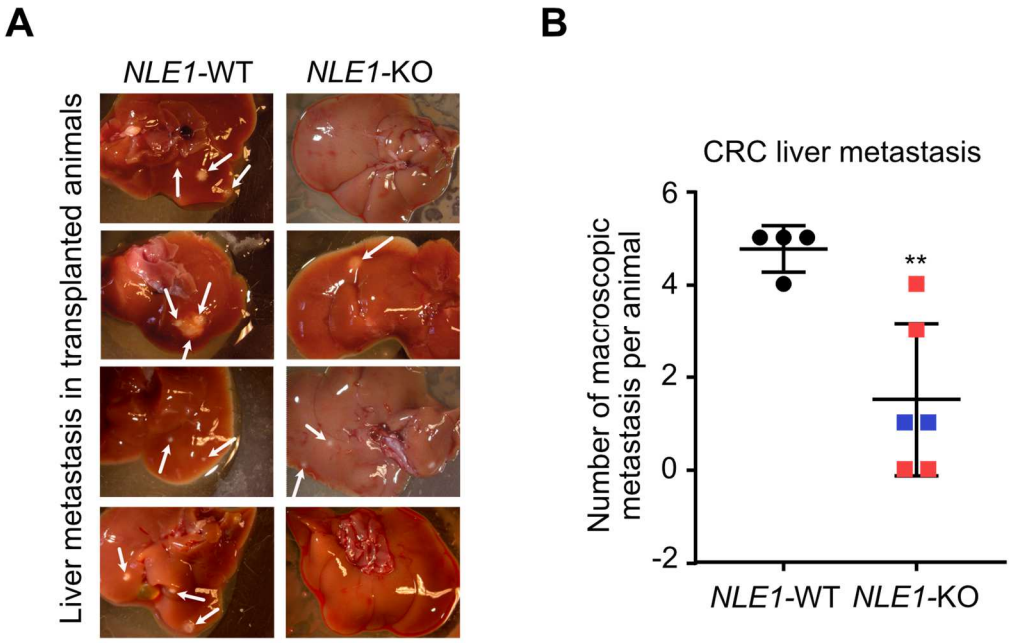

Figure 40: Liver metastatic burden is reduced in *NLE1* knockout transplanted mice
A) Macroscopic pictures of resected livers and CRC-derived liver metastases formed in immunodeficient mice 35 days after orthotopic transplantation with *NLE1* wild-type (WT) or *NLE1* knockout (KO) PDTOs. Arrows indicate metastatic foci. B) Macroscopically visible metastatic foci were counted in the liver of immunodeficient mice 35 days after orthotopic transplantation with *NLE1* wild-type (WT, black dots) PDTOs or *NLE1* knockout (KO, *NLE1*-targeting guide RNAs 1 (red dots) or 2 (blue dots)) PDTOs. Asterisks (** P-value < 0.01) indicate statistical significance between the *NLE1*-WT and *NLE1*-KO groups as determined by an unpaired t-test plus Welch's correction. Welch's correction was applied due to unequal SDs within the two groups. Data are represented as mean ± SD [modified from 239]. The reuse of figures was allowed by AACR (Creative Commons CC-BY-NC-ND license).

In conclusion, ablation of *NLE1* in an endoscopy-based orthotopic transplantation model suppresses primary tumor growth in the colon and diminishes the liver metastatic burden of xenotransplanted mice.

5.8. *NLE1* mRNA levels are increased in Wnt/MYC-expressing CRC molecular subtypes and predict relapse-free survival in CRC patients

To investigate if a higher *NLE1* expression could also be reflected in CRC patients compared to their healthy controls, *NLE1* gene expression data from TCGA (via the GDC Data Portal) was collected. Indeed, *NLE1* levels in 638 patients were upregulated (Figure 41A). Furthermore, analysis of 15 different CRC cohorts with patient-matched CRC and normal tissue pairs revealed an increased *NLE1* expression in CRC samples (Figure 41B).

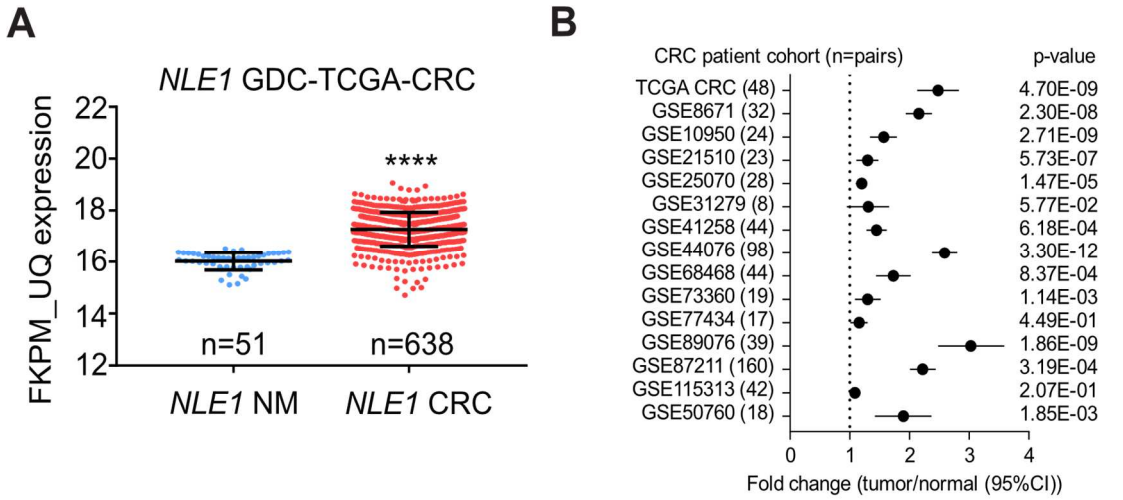

Figure 41: *NLE1* levels are increased in various CRC patient cohorts
A) RNA sequencing data of the human TCGA-COAD plus READ cohort (FKPM-UQ data) was used for the comparison of *NLE1* expression in normal colonic mucosa (n = 51) and CRC tumor tissue (n = 638). Asterisks (**** $p < 0.0001$) indicate statistical significance between groups as determined by an unpaired t-test. B) Fold changes of *NLE1* mRNA expression in CRC tumors and their matched adjacent normal colonic mucosa were calculated and represented as a forest plot. Publicly available data sets were used. Each GEO database accession number indicates one data set. The number in brackets represents the number of patient-matched tumor/normal pairs. Dots denote fold changes, while horizontal lines represent a 95% confidence interval (CI). A paired t-test determined statistical significance (p-value). Data in panel B was provided by Dr. Matjaz Rokavec [adjusted from 239]. The reuse of figures was allowed by AACR (Creative Commons CC-BY-NC-ND license).

We also analyzed if *NLE1* expression correlated with consensus molecular subtypes (CMS) and CRC intrinsic subtypes (CRIS) [235, 236]. The consensus molecular subtypes comprise four categories: "CMS1, microsatellite instable and strong immune activation; CMS2, canonical, WNT and MYC activation; CMS3, metabolic dysregulation; CMS4, mesenchymal, TGF-β activation" [236]. As expected from our previous data, *NLE1* levels positively correlated with the CMS2 subtype and negatively with the CMS4 subtype (Figure 42). For the CRIS classification, we observed something similar. The CRIS classification consists of 5 subtypes: "CRIS-A, mucinous, glycolytic, microsatellite instable, KRAS mutations; CRIS-B, TGF-β pathway activity, epithelial-mesenchymal transition, poor prognosis; CRIS-C, elevated epidermal growth factor receptor (EGFR) signaling, EGFR inhibitor sensitive; CRIS-D, WNT activation, Insulin-like growth factor 2 (IGF2) gene overexpression; CRIS-E, Paneth cell-like phenotype, *TP53* mutations" [235]. *NLE1* levels were highest in CRIS-C/D subtypes and lower in CRIS-B (Figure 42), which fits the previously described CMS classification.

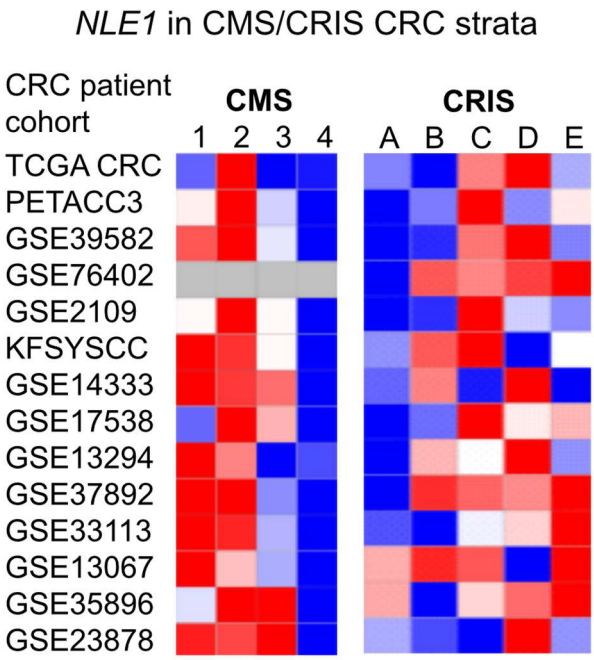

Figure 42: *NLE1* expression correlates with Wnt/MYC-expressing CRC molecular subtypes
Heat maps depicting relative *NLE1* mRNA expression in cancer molecular subtypes (CMS, from [236]) and CRC intrinsic subtypes (CRIS, from [235]) of different publicly available CRC cohort data sets. Each GEO database accession number indicates one data set. Relatively high expression levels of *NLE1* are colored in red, and relatively low expression levels of *NLE1* are colored in blue. Data was provided by Dr. Matjaz Rokavec [adapted from 239]. The reuse of figures was allowed by AACR (Creative Commons CC-BY-NC-ND license).

Since CMS2 and CRIS-C/D subtypes are associated with good patient prognosis, we wondered if *NLE1* levels in different patient cohorts could predict relapse-free survival. Therefore, the hazard ratio for relapse-free survival of CRC patients from 11 different, public availably cohorts was determined (Figure 43). 8 out of 11 cohorts showed that high *NLE1* levels correlated with increased relapse-free survival.

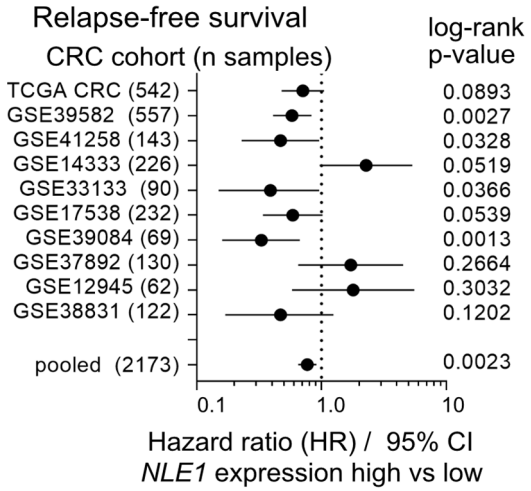

Figure 43: High *NLE1* expression is associated with increased relapse-free survival
Hazard ratios (HR) for relapse-free survival of CRC patients with either low or high *NLE1* mRNA expression were analyzed in different publically available CRC cohorts (TCGA CRC and NCBI Gene Expression Omnibus, GEO) and are represented as a forest plot. Each GEO database accession number indicates one data set. Dots denote HRs, while horizontal lines represent a 95% confidence interval (CI). Statistical significance (log-rank p-value) was calculated for each CRC cohort. Data was provided by Dr. Matjaz Rokavec [modified from 239]. Reuse of the figure was allowed by AACR (Creative Commons CC-BY-NC-ND license).

In conclusion, we could show that expression of *NLE1* is upregulated in CRC patient cohorts, correlates positively with Wnt/MYC-signature expressing CRC molecular subtypes and negatively with TGF-β signaling, and predicts relapse-free survival in CRC patients.

5.9. Loss of TP53 sensitizes NLE1-deficient, microsatellite-instable CRC cells to apoptosis

The tumor suppressor protein TP53 is frequently lost/inactivated in chromosomally instable CRC but retains wild-type in a higher fraction (~65-70%) of microsatellite instable CRC [268]. Since TP53 has also been shown to be activated during nucleolar stress and our data proposed NLE1 as a possible target for therapy of CRC rather than a predictor of unfavorable disease progression, we were wondering which consequences *NLE1* deletion has on CRC cells dependent on their *TP53* status [269, 270]. Hence, *TP53* knockout derivatives of the microsatellite instable cell line HCT116 were generated. After that, pools from *TP53* wild-type and *TP53* knockout HCT116 cells were edited via CRISPR/Cas9 to achieve *NLE1* knockout derivatives and analyzed concerning cell cycle progression and apoptosis induction (Figure 44).

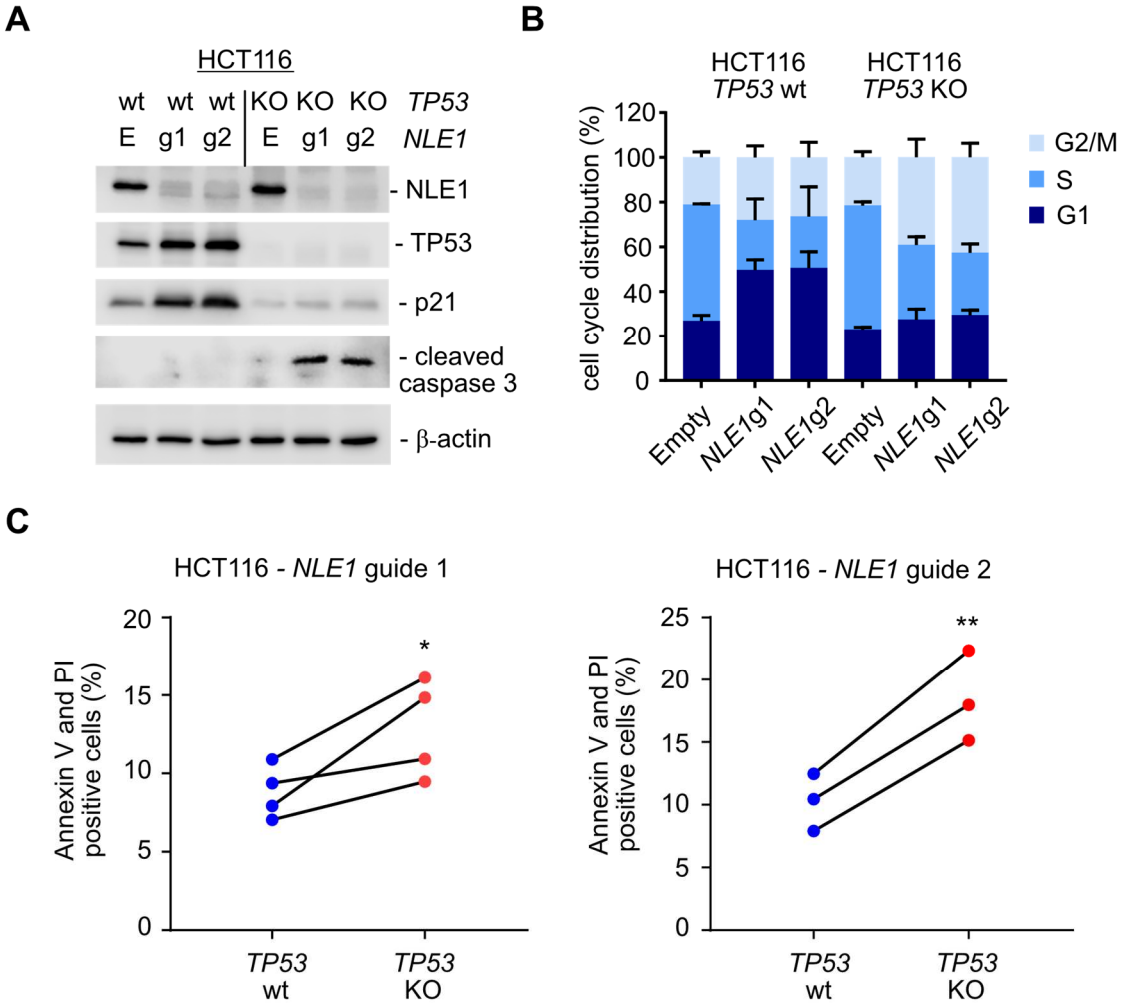

Figure 44: Loss of TP53 sensitizes NLE1-deficient, microsatellite instable CRC cells to apoptosis
A) Protein expression levels of NLE1, TP53, CDKN1A (p21), and cleaved caspase 3 in HCT116 *TP53* wild-type (*TP53* wt) and *TP53* knockout (*TP53* KO) cells edited via CRISPR/Cas9 to achieve *NLE1* knockout were detected by immunoblotting. Two different guide RNAs (NLE1g1, NLE1g2) were used. Control cells were transduced with the same vector but without guide RNAs (Empty). Housekeeping protein β-actin was used as a loading control. B) Cell-cycle analysis was performed in HCT116 *TP53* wild-type (*TP53* wt) and *TP53* knockout (*TP53* KO) cells edited via CRISPR/Cas9 to achieve *NLE1* knockout. Two different guide RNAs (NLE1g1, NLE1g2) were used. Control cells were transduced with the same vector but without guide RNAs (Empty). Cell-cycle distribution (in %) is represented as mean ± SD (n = 3). C) Apoptotic cell fractions of HCT116 *TP53* wild-type (*TP53* wt) and *TP53* knockout (*TP53* KO) cells edited via CRISPR/Cas9 to achieve *NLE1* knockout were quantified by Annexin-V/propidium iodide (PI) staining and flow cytometry analysis. Two different guide RNAs (left panel: NLE1g1, right panel: NLE1g2) were used. Control cells were transduced with the same vector but without guide RNAs (Empty). Asterisks (*: P-value ≤ 0.05, **: P-value ≤ 0.01) indicate statistical significance between pairs as determined by a ratio-paired t-test. Each pair of blue-red dots connected by solid lines depicts an independent experiment [adjusted from 239]. The reuse of figures was allowed by AACR (Creative Commons CC-BY-NC-ND license).

Immunoblot analysis revealed stabilization of TP53 and induction of the TP53 target gene CDKN1A/p21 in *TP53* wild-type *NLE1* knockout HCT116 cells, while no caspase 3 cleavage was observable. In contrast, *TP53* knockout *NLE1* knockout HCT116 cells showed increased levels of cleaved caspase 3, while p21 induction was not observed (Figure 44A). Cell cycle analysis on the different genotypes revealed a substantial difference between *TP53* wild-type and *TP53* knockout cells during the loss of NLE1

(Figure 44B). In detail, the G1-phase in *TP53* wild-type *NLE1* knockout cells was increased while the S-phase decreased. In contrast, loss of *NLE1* in *TP53* knockout cells increased G2/M-phase while reducing S-phase. Furthermore, the detection of apoptotic cells via flow cytometry revealed the induction of apoptotic cells in *TP53* knockout *NLE1* knockout HCT116 cells versus *TP53* wild-type *NLE1* knockout HCT116 cells (Figure 44C). These data imply that activation of TP53/p21 signaling and G1 arrest occurs due to NLE1 loss in microsatellite instable *TP53* wild-type CRC cells, while their *TP53* deficient counterpart may preferentially respond with apoptosis.

We also studied whether p21 induction occurs in microsatellite stable CRC (HT29, SW620) cells (Figure 45A, B). Both HT29 and SW620 cells express mutant variants of TP53 (HT29: R273H; SW620: R273H;P309S); therefore, we would not expect them to induce p21. Surprisingly, when analyzing with qRT-PCR and immunoblot analysis, an induction in p21 during ablation of *NLE1* could be observed. Still, SW620 cells responded less strongly compared to HT29 cells. We speculate that loss of NLE1 can also trigger TP53-independent processes leading to elevated levels of p21, thereby generating tumor cell-specific protection of CRC cells.

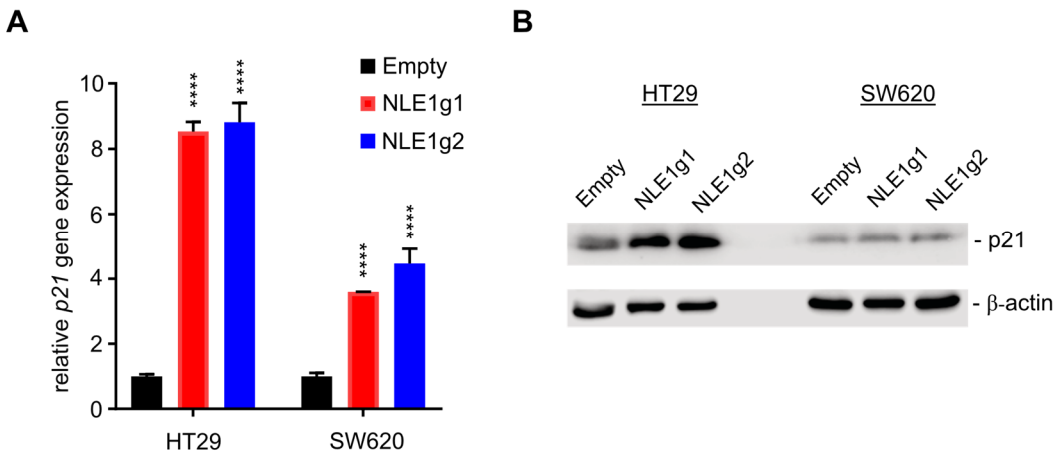

Figure 45: Deletion of *NLE1* leads to wild-type TP53-independent induction of p21 in microsatellite stable CRC cell lines
A) Gene expression level of *CDKN1A/p21* was analyzed in HT29 and SW620 cells edited via CRISPR/Cas9 to achieve *NLE1* knockout via qRT-PCR. Two different guide RNAs (NLE1g1, NLE1g2) were used. Control cells were transduced with the same vector but without guide RNAs (Empty). Asterisks (****: P-value ≤ 0.0001) indicate statistical significance between samples as determined by two-way ANOVA plus Dunnett´s multiple comparison test. Data are represented as mean ± SD (n = 3). B) Protein expression levels of CDKN1A/p21 in HT29 and SW620 cells edited via CRISPR/Cas9 to achieve *NLE1* knockout were detected by immunoblotting. Two different guide RNAs (NLE1g1, NLE1g2) were used. Control cells were transduced with the same vector but without guide RNAs (Empty). Housekeeping protein β-actin was used as a loading control. Notably, SW620 cells display lower amounts of p21 and show weaker induction of p21 upon *NLE1* ablation than HT29 cells [adapted from 239]. The reuse of figures was allowed by AACR (Creative Commons CC-BY-NC-ND license).

Furthermore, we questioned if *NLE1* expression correlated with *TP53* status in CRC patients. Therefore, 6 different cohorts of CRC patients with *TP53* wild-type or *TP53*

mutant tumors were analyzed (Figure 46). None of them showed any correlations between *TP53* status and *NLE1* expression. This suggests that *NLE1* expression is not dependent on *TP53* status in CRC patients.

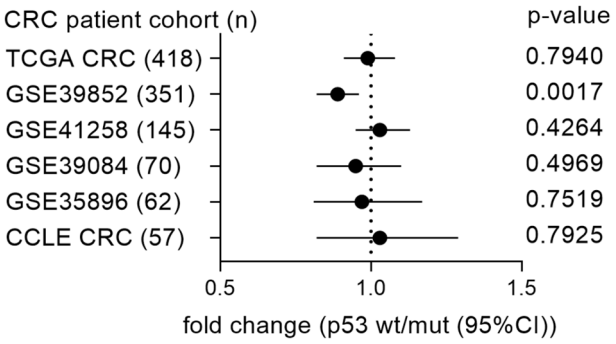

Figure 46: *TP53* status does not correlate with *NLE1* expression in CRC
Fold changes of *NLE1* mRNA expression between *TP53* wild-type and *TP53* mutant CRC tumors were calculated and represented as a forest plot. Publicly available data sets were used. Each GEO database accession number indicates one data set. In brackets, the number of patients in each cohort is mentioned. Dots denote fold changes, while horizontal lines represent a 95% confidence interval (CI). A paired t-test determined statistical significance (p-value). Data was provided by Dr. Matjaz Rokavec [modified from 239]. The reuse of figures was allowed by AACR (Creative Commons CC-BY-NC-ND license).

Taken together, wild-type TP53 can protect microsatellite instable CRC cells against NLE1 loss-mediated apoptosis via p21 induction but does not directly correlate with the magnitude of *NLE1* expression in CRC patients.

5.10. Deletion of *NLE1* in immortalized human colonic epithelial cells (HCEC-1CT) provokes cell cycle arrest rather than apoptosis

An existing therapeutic window implies that a substance might be helpful for patient treatment. To test if a therapeutic window for NLE1 might exist, we examined the effects of *NLE1* deletion in a normal colonic epithelial cell line regarding proliferation, cell cycle, and apoptosis.

NLE1 knockout derivatives of HCEC-1CT human colonic cells were generated via CRISPR/Cas9 and analyzed with the previously mentioned assays. As expected, knockout of *NLE1* in HCEC-1CT cells caused inhibition of proliferation (Figure 47A). Next, for cell cycle analysis, we could observe a decrease in the S-phase and an increase in the G2/M phase (Figure 47B). This might explain the halted proliferation we observed previously. Interestingly, when analyzing apoptosis via Annexin V/PI staining and immunoblot analysis, *NLE1* knockout cells did not respond with higher levels of apoptosis or apoptotic markers such as cleaved PARP and cleaved caspase 3 (Figure 47C, D). Therefore, we suggest that the ablation of *NLE1* in HCEC-1CT cells provokes cell cycle arrest rather than apoptosis.

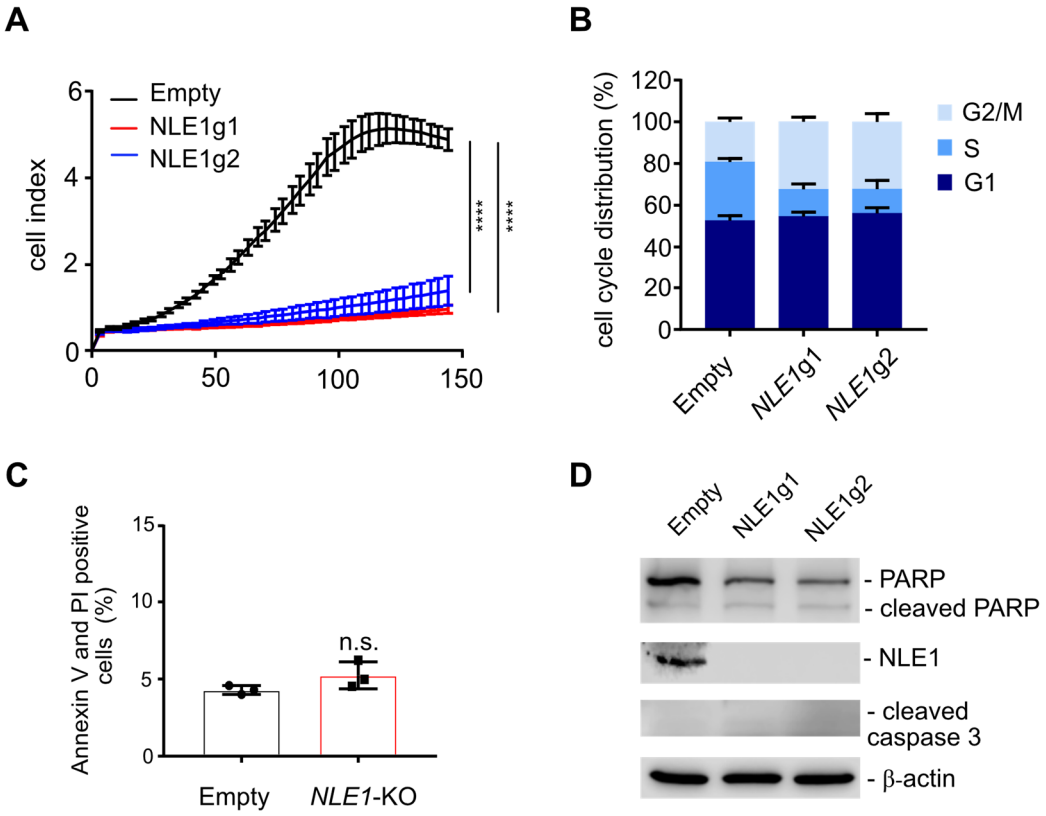

Figure 47: Loss of NLE1 in immortalized human colonic epithelial cells (HCEC-1CT) provokes cell cycle arrest rather than apoptosis
A) Proliferation kinetics of immortalized human colonic epithelial cells (HCEC-1CT) edited via CRISPR/Cas9 to achieve *NLE1* knockout were monitored using the xCELLigence system. Two different guide RNAs (NLE1g1 in red, NLE1g2 in blue) were used. Control cells were transduced with the same vector but without guide RNAs (Empty, black). Asterisks (****: P-value ≤ 0.0001) indicate statistical significance between samples for the latest time point as determined by two-way ANOVA plus Tukey's multiple comparisons test. Data are represented as mean ± SD (n = 7). B) Cell-cycle analysis was performed in HCEC-1CT cells edited via CRISPR/Cas9 to achieve *NLE1* knockout. Two different guide RNAs (NLE1g1, NLE1g2) were used. Control cells were transduced with the same vector but without guide RNAs (Empty). Cell-cycle distribution (in %) is represented as mean ± SD (n = 3). C) Apoptotic cell fractions of HCEC-1CT Empty (black) and *NLE1* knockout (KO, red) cells were quantified by Annexin-V/propidium iodide (PI) staining and flow cytometry analysis. Data are represented as mean ± SD (n = 3). No significant statistical difference was observed (n.s.). D) Protein expression levels of NLE1, PARP, cleaved PARP, and cleaved caspase 3 in HCEC-1CT edited via CRISPR/Cas9 to achieve *NLE1* knockout were detected via immunoblotting. Two different guide RNAs (NLE1g1, NLE1g2) were used. Control cells were transduced with the same vector but without guide RNAs (Empty). Housekeeping protein β-actin was used as a loading control [adjusted from 239]. The reuse of figures was allowed by AACR (Creative Commons CC-BY-NC-ND license).

We also investigated if loss of NLE1 inhibits *de novo* protein biosynthesis in non-malignant colon cells. Flow cytometry analysis of OPP incorporation in *NLE1* wild-type and *NLE1* knockout HCEC-1CT cells was performed (Figure 48). *NLE1* wild-type cells were treated with cycloheximide as a control for diminished protein biosynthesis. Indeed, loss of NLE1 diminished protein biosynthesis in HCEC-1CT cells, although to a lower extent when compared to CRC cell lines.

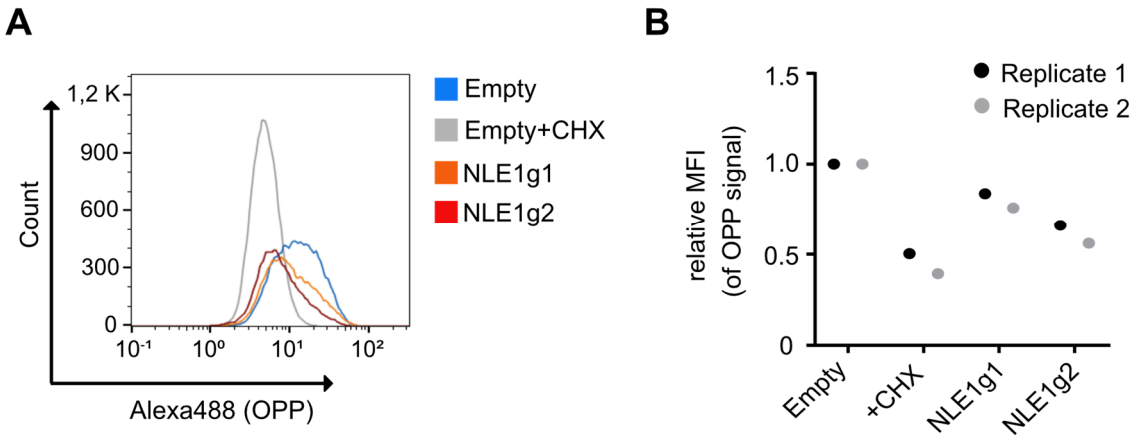

Figure 48: *De novo* protein biosynthesis is diminished in immortalized human colonic epithelial cells (HCEC-1CT) after *NLE1* ablation
A) Flow cytometry analysis of OPP incorporation in immortalized human colonic epithelial cells (HCEC-1CT) edited via CRISPR/Cas9 to achieve *NLE1* knockout. Two different guide RNAs (NLE1g1 in orange, NLE1g2 in red) were used. Control cells were transduced with the same vector but without guide RNAs (Empty, blue). As a positive control for inhibition of protein biosynthesis, Empty cells were treated with cycloheximide (Empty+CHX, grey). B) Mean fluorescence intensity (MFI) levels of HCEC-1CT control cells (Empty), Empty cells treated with CHX (+CHX) and *NLE1* knockout cells (NLE1g1, NLE1g2) labeled with OPP. MFI levels were normalized to Empty cells and used as a reference (relative MFI=1.0). Two replicates (n = 2) are shown [adapted from 239]. The reuse of figures was allowed by AACR (Creative Commons CC-BY-NC-ND license).

These results show that non-malignant colon cells depend on NLE1 expression but do not respond with apoptosis compared to CRC cell lines. Therefore, therapeutic inhibition of NLE1 in CRC patients could be possible. However, further studies are necessary to investigate the possible occurrence of on-target adverse events and toxicity upon NLE1 targeting in pre-clinical and clinical settings.

6. Discussion

The underlying mechanism of how metastasis in CRC arises is not fully understood yet. Mutations in critical components of TP53 or TGF-β signaling play an important role [55, 271, 272]. Especially the loss of SMAD4, a central protein in TGF-β signaling, was shown to promote tumor growth, metastasis, and therapy resistance in a manifold fashion [73, 74]. For example, *Smad4* loss leads to the upregulation of Ccl9, which recruits myeloid cells via Ccr1 and promotes CRC metastasis [92, 93]. Furthermore, cell-intrinsic factors are affected [73, 74]. TGF-β usually induces pro-apoptotic genes such as *BIM* and *DAPK*. When *SMAD4* is deleted, these genes are not induced by TGF-β signaling activation, and the cancer cells are less prone to undergo apoptosis [81, 83, 84].

Most of the two-dimensionally grown CRC cell lines suffer from loss of *SMAD4* or harbor *TGFBR* mutations, resulting from the long-term culture of cells in FBS-containing medium. FBS contains more than 1,000 different components, including TGF-β, thereby promoting the natural selection of CRC cells with inactivating alterations of the TGF-β pathway [273, 274]. Therefore, these cell lines no longer respond to TGF-β stimulation *in vitro*. In addition, attempts to re-express SMAD4 in SMAD4-deficient cell lines are difficult because the protein levels are often not physiological and therefore do not represent the basal levels in a tumor context.

To overcome these limitations and investigate which genes are commonly deregulated in SMAD4-deficient cells in a TGF-β-rich environment, this thesis aimed to introduce *SMAD4* mutations in PDTOs and analyze their gene expression profile in response to TGF-β. Subsequently, new TGF-β target genes that might confer a survival advantage for cancer cells were identified and characterized. This could lead to a better understanding of how *SMAD4* mutations promote tumor growth and metastasis and contribute to poorer overall survival in CRC patients [52, 53].

6.1. Modeling of a *SMAD4* mutation in PDTOs reveals the prevention of TGF-β-mediated downregulation of vulnerability genes

The first aim of this thesis was to investigate how the gene expression profile of PDTOs changes upon acquisition of a *SMAD4* deletion and exposure to TGF-β. Since PDTOs are cultured in a well-defined medium that prevents TGF-β signaling and does not impose selective pressure on *SMAD4* wild-type CRC cells, they are an excellent tool to identify new TGF-β target genes.

First, CRISPR/Cas9-mediated targeting of *SMAD4* in two different PDTO lines was performed. After selection with TGF-β for three weeks, we could observe a complete loss

of SMAD4 at the protein level. In addition, the T7EI mismatch cleavage assay proved the *SMAD4* knockout on the genomic level. This aligns with recent literature, which described the introduction of mutations in *KRAS*, *TP53*, *APC*, and *SMAD4* via CRISPR/Cas9-mediated genome editing in human small intestinal organoid stem cell cultures [226]. To select for SMAD4 deficient cells, Drost *et al.* used the intestinal organoids' dependency on the bone morphogenetic protein (BMP) pathway inhibitor noggin. They cultured organoids without noggin for 1-2 weeks [226, 275]. BMP signaling remained when noggin was missing; only SMAD4-deficient cells could grow under these conditions. In contrast, in our approach, PDTOs were cultured with noggin and simultaneously treated with recombinant TGF-β. Thereby active TGF-β signaling was promoted, and only cells with a loss of SMAD4 kept growing. Smit *et al.* used the same approach. To achieve the knockdown of *SMAD4*, they selected with recombinant TGF-β for at least 7 days [246]. Since SMAD4 is an essential component of the BMP and TGF-β pathway, both selection methods are eligible.

In addition, we could show that our SMAD4-deficient PDTOs grow normally under TGF-β treatment compared to their wild-type counterparts. This was expected because the complete loss of SMAD4 should lead to resistance to TGF-β, as already described in the literature. If TGF-β does not activate SMAD4 and cannot translocate into the nucleus to induce cell cycle arrest and apoptosis, the proliferation of cancer cells is sustained [276-278]. Hence, our observation that the PDTOs proliferated normally upon TGF-β treatment suggests the successful generation of SMAD4-deficient PDTOs.

We analyzed these SMAD4-deficient PDTOs and their wild-type counterparts under TGF-β treatment on a transcriptomic level. There we observed an enrichment for c-MYC target genes and human colonic stem cell gene sets and depletion for differentiation and TGF-β gene sets. It was already described that loss of *Smad4* increased the frequency of LGR5+ cells, thereby promoting tumor growth and metastasis *in vivo* [117]. Due to LGR5 being an essential marker for stem cells, this fits with our enrichment of stem cell genes in SMAD4-deficient PDTOs. In agreement with this observation, differentiation genes were depleted in SMAD4-deficient PDTOs under TGF-β, suggesting that SMAD4-deficient cells acquire a more stem cell-like phenotype. This concurs with literature describing that TGF-β induces differentiation in colonic epithelial cells [76, 77, 279]. In SMAD4-deficient cells, the induction of differentiation genes is prevented. Also, the enrichment for c-MYC target genes was expected because Warner *et al.* already showed that TGF-β downregulates *c-MYC* and thereby provokes cell cycle arrest [88]. Hence, if *c-MYCs* downregulation is prevented, its target genes are still active and contribute to cell proliferation. The observed depletion of specific TGF-β target genes also fits our hypothesis because one would expect that TGF-β regulated genes in wild-type cells should not change in SMAD4-deficient cells. Therefore, an enrichment in these genes concerning their mRNA expression levels in SMAD4-deficient cells should be observed.

For example, *PMEPA1*, a known TGF-β target gene in CRC, was not induced in SMAD4-deficient PDTOs under TGF-β treatment compared to their wild-type controls [241]. We conclude that SMAD4-deficient PDTOs under TGF-β treatment acquired a more stem cell-like phenotype, confirming that the *in vivo* observed phenotype in mice could also be reflected in CRC patients.

The second aim of this thesis was to examine which of these deregulated genes in SMAD4-deficient PDTOs in exposition to TGF-β might confer an advantage for tumor cell fitness. Therefore, we combined our list of deregulated genes with the DepMap project. The Cancer Dependency Map project systematically identifies genetic dependencies and small molecule sensitivities in a tumor-specific manner. Therefore, it uses genome-wide CRISPR/Cas9 and shRNA screens in different cancer cell lines [243, 244]. We identified only 11 out of 284 genes (*FBL, GINS2, IFITM3, LSM6, MYC, NAT10, NLE1, POLR3K, PRMT1, PSMG4,* and *RRP1*) to be essential. Reasons for this low number of essential genes include factors mediating interactions between cancer cells and their adjacent microenvironment and genes that may have redundant functions. Still, these 11 genes show consistency with recent literature. For example, the knockdown of *IFITM3* in CRC cell lines diminished proliferation and migration/invasion *in vitro*. In addition, tumor growth and liver metastasis declined *in vivo* [280]. Also, the knockdown of *c-MYC* or *GINS2* resulted in cell cycle arrest and disturbed proliferation [281, 282]. The literature has already described connections of TGF-β signaling with *c-MYC*, GINS2, and IFITM3 [88, 283, 284]. For example, the downregulation of *c-MYC* by TGF-β was shown in 1999 [88]. This proves that our screening method can identify TGF-β regulated genes essential for cellular fitness.

Surprisingly, 4 of these 11 genes (*FBL*, *NAT10*, *NLE1,* and *RRP1*) participate in ribosome biogenesis and might contribute to tumor progression. Recent studies described the relevance of elevated protein biosynthesis levels in CRC [246, 285]. Upon the acquisition of *TP53* and *SMAD4* mutations, an increase in global biosynthesis rates could be observed [246]. Furthermore, colorectal CSCs showed the highest rates of ribosomal DNA transcription and protein biosynthesis within a tumor [286]. However, which factors contribute to this phenotype remains to be shown.

Based on the previously described literature about NLE1 and our screening results, we decided to investigate the role of NLE1 in the progression of CRC in more detail.

6.2. c-MYC binds to the *NLE1* promoter and prevents TGF-β mediated downregulation of NLE1 in CRC

Since TGF-β downregulated *NLE1* and *c-MYC* in our SMAD4 wild-type PDTOs compared to their SMAD4-deficient counterparts and c-MYC is known to regulate

protein biosynthesis in multiple ways, we investigated if a direct regulation between c-MYC, TGF-β, and NLE1 might exist. Indeed, we could show that c-MYC bound to the promoter of *NLE1* and rescued TGF-β-mediated downregulation of it.

This aligns with previously published data showing that c-MYC enhanced ribosome biogenesis in multiple ways, either by upregulating Pol I transcription or altering RNA modifications [131-133]. For example, c-MYC interacts with rDNA loci and recruits SL1, activating *Pol* I transcription [142-144]. Moreover, c-MYC can directly bind to the promoter of *DKC1*, a pseudouridine synthase in complex with H + ACA small nuclear RNAs, and mediates post-transcriptional modifications of ribosomal RNA (rRNA). Mutations in this gene were associated with increased tumor formation [247, 249, 287]. Furthermore, c-MYC can bind to the promoter of *NPM1*, an RNA-binding protein that directly binds to C/D box small nucleolar RNAs (snoRNAs) to regulate 2-O' methylation on rRNA. Thereby translation is modulated. Mutations in *NPM1* were associated with hematological disease [248, 250]. We conclude that c-MYC can similarly modify the expression of *NLE1* like *DKC1* or *NPM1*. When *SMAD4* is deleted, TGF-β cannot repress c-MYC, and c-MYC can induce *NLE1* expression, promoting protein biosynthesis. With this enhanced protein biosynthesis, SMAD4-deficient cancer cells can proliferate faster in a TGF-β rich environment.

However, it should be noted that our experimental setting imposed some restrictions. For example, the ChIP assay was performed in cell lines instead of PDTOs because a considerable amount of chromatin is necessary, which is impossible using PDTOs. We could only detect if c-MYC binds to the *NLE1* promoter without TGF-β treatment because CRC cell lines are not responsive to TGF-β treatment. Since c-MYC expression should decrease upon TGF-β treatment, we would expect that also NLE1 levels would decrease. This would prove the direct connection between TGF-β, c-MYC, and NLE1. Next, the chromatin's quality and the antibody's specificity are also critical. Otherwise, the proteins cannot bind to the DNA fragments, or unspecific fragments are enriched. Hence, we included an isotype-matched control antibody (Immunoglobulin G, IgG) to control for the assay's background. Furthermore, positive and negative control loci were measured. Positive control loci were *NPM1* and *DKC1*, which are known to bind to c-MYC. The negative control locus was a DNA region 5 kb downstream of the *NLE1* promoter amplicon where c-MYC should not bind. Also, the TGF-β/c-MYC/NLE1 rescue experiment has restraints. The dosage of an overexpressed gene is not physiological compared to the endogenous levels observed in patients or cells. We only used wild-type PDTOs to investigate what occurs under TGF-β or TGF-β combined with c-MYC overexpression. It would also be interesting to use CRISPR/Cas9-mediated mutagenesis to modify the c-MYC binding site in the promoter region of *NLE1*. Different guide RNAs targeting a sequence on the (+) or the (-) strand of the c-MYC binding site should be used.

When cells are treated with TGF-β or TGF-β combined with c-MYC overexpression, c-MYC should not affect *NLE1* expression anymore.

Future studies should uncover the exact mechanism of how this interplay between TGF-β, c-MYC, and NLE1 contributes to the ribosome biogenesis levels in CRC.

6.3. Knockout of *NLE1* suppresses *de novo* protein biosynthesis and diminishes CRC growth, migration/invasion, and survival

As already mentioned before, NLE1 was characterized as being part of the ribosome assembly and maturation [136, 140, 141]. Therefore, we analyzed *de novo* protein biosynthesis rates in CRC cell lines and PDTOs and could indeed observe a reduction in the translational capacity of *NLE1* knockout CRC cells.

Recently, several studies showed that defects in ribosomal proteins lead to impaired ribosome biogenesis and therefore reduce protein synthesis [166, 288, 289]. Teng *et al.* performed siRNA-mediated knockdown of *RPL5* and *RPL11*, both components of the ribosomal 60S subunit, and analyzed their polysome profiles. An increase in 40S ribosomal subunits and a decrease in 60S subunits were observed. In addition, they detected reduced mean polysome size, increased formation of half-mer polysomes, and decreased translation rates measured by 35S-labeled methionine incorporation assay [288]. Another example was shown in the *RPL15* gene. Dong *et al.* reported overexpression of RPL15 in CRC and showed that RPL15 was required for 60S ribosomal subunit biogenesis. In detail, siRNA-mediated knockdown of *RPL15* in HeLa cells was performed and then analyzed via sucrose gradient by ultracentrifugation. The knockdown of *RPL15* showed much higher levels of the 40S ribosomal subunits and a decrease in the 60S subunits. In addition, the nucleolar structures became incompact upon *RPL15* depletion [289]. Furthermore, mutations in ribosomal proteins of the 40S subunit occur. For example, in CLL, patients showed mutations in the *RPS15* gene. Some of these mutations reduced 35S-Met/Cys incorporation, proving that global protein synthesis was reduced. Bretones *et al.* suggested that modifications in mRNA translation patterns were the reason for the observed phenotype [166].

These are just a few examples showing ribosome composition's importance in maintaining global translation levels. Knockout of *NLE1* might impair the ratio between the 40S and 60S subunit, thereby promoting the formation of half-mer polysomes. Moreover, the nucleolar structure itself might be affected [289]. This could account for the observed reduction in *de novo* protein biosynthesis levels.

An issue with our applied OPP incorporation assay is that we could only measure protein synthesis rates semi-quantitatively because flow cytometry discriminates between high

and low levels of OPP incorporation but does not determine the absolute rates. To quantify absolute protein rates, radioactive 35S-methionine pulse labeling is used. This assay is more sensitive and shows a better signal-to-noise ratio than OPP labeling. The OPP assay's sensitivity depends on how well the Click-It reaction works and in which growth phase the cells are. Moreover, we did not perform polysome profiling to determine the ratio between the 40S and 60S subunits, which could prove the occurrence of defective polysomes. Therefore, we can only conclude that the deletion of *NLE1* reduces protein biosynthesis in CRC cell lines and PDTOs. Future studies should determine if loss of NLE1 leads to a lower number of polysomes or accumulation of dysfunctional polysomes.

As expected, ablation of *NLE1* also affected various parameters in CRC cell lines and PDTOs: *NLE1* knockout in CRC cell lines led to slower proliferation kinetics, less colony formation, and impaired anchorage-independent growth. Furthermore, *NLE1* knockout cells showed higher levels of apoptosis, less migratory/invasive capacity, and underwent cell cycle arrest. In the case of PDTOs, loss of NLE1 resulted in smaller organoid sizes and reduced clonogenicity after organoid cell re-seeding.

Our data agree with recent literature showing that dysregulation of ribosomal proteins is associated with cellular fitness and malignant transformation of cancer cells. For example, Labriet *et al.* demonstrated that the knockdown of *RPL28* in HCT116 and HT-29 cells led to slower proliferation kinetics [290]. Accordingly, the knockdown of *RPL15* in HCT116 cells resulted in slower proliferation. Furthermore, *RPL15* knockdown in HCT116 cells led to increased apoptosis, as shown by enhanced Annexin V/PI double-positive cells and expression of cleaved caspase 3 [289]. This proves that the loss of ribosomal proteins induces apoptosis in CRC cells. In addition, the knockdown of *RPL27A* in triple-negative breast cancer (TNBC) cells was associated with decreased cell migration and invasion [291]. Knockdown of *RPL34* in osteosarcoma cell lines resulted in an impaired cell cycle. In particular, there was an increase in the G2/M phase and a decrease in the S phase, indicating growth arrest [292]. In total, loss of NLE1 in CRC cell lines leads to the same phenotype observed for other ribosomal proteins in various tumor entities.

The reduced organoid size and clonogenicity in *NLE1* knockout PDTOs were comparable to a study from Otto *et al.,* who described that treatment with the RNA Pol I inhibitor CX-5461 led to a smaller size and less viability in murine tumor organoids (MTOs) and PDTOs. CX-5461 perturbs the recruitment of SL1 to the chromatin and thereby prevents the interaction of RNA Pol I with rDNA. With this defective ribosome biogenesis, MTOs and PDTOs could not proliferate anymore. In contrast, wild-type mouse organoids did not respond as strongly and continued proliferating [293]. Unfortunately, there is not much literature on this topic available. Especially, loss-of-function studies of ribosomal

proteins in organoids are missing. Nevertheless, we can conclude that disruption of ribosome biogenesis by loss of NLE1 or inhibition of RNA Pol I results in decreased organoid size and formation, proving that ribosomal proteins are essential for organoid growth.

Interestingly, the differences observed in our PDTOs were mild compared to CRC cell lines which showed massive effects. One possible explanation is that the PDTOs showed a more extensive genetic diversity and ribosomal heterogeneity than long-term cultured cell lines. The passage number of PDTOs was relatively low compared to cell lines established decades ago. During this time, one might have selected clones more sensitive to the loss of ribosomal proteins. In contrast, PDTOs could partially tolerate the loss of NLE1 and circumvent the stress that NLE1 mediates in CRC cell lines. Another possibility is that due to the overall slow and heterogenous growth kinetics in PDTOs, the effect of NLE1 loss on ribosome biogenesis was already abolished, and other ribosomal proteins substituted for the loss of NLE1. Furthermore, the medium of PDTOs could contain factors that compensate for the loss of NLE1; thereby, PDTOs could still grow normally. Future studies are warranted to investigate the differences in effect size between cell lines and PDTOs upon *NLE1* deletion.

To complement our loss of function studies of NLE1, we also implemented gain of function studies. Overexpression of NLE1 in PDTOs or the immortalized normal human colonic cell line (HCEC-1CT) did not promote proliferation or *de novo* protein biosynthesis. Also, overexpressing NLE1 could not rescue TGF-β-mediated growth inhibition in PDTOs.

This contradicts prior research that found that overexpression of ribosomal proteins can accelerate tumor growth. Shi *et al.* examined the overexpression of RPL15 in liver cancer cell lines and could show that this promoted cell proliferation, colony formation, cell cycle progression, migration/invasion, and resistance to apoptosis [294]. Ebright *et al.* showed that the overexpression of RPL15 or RPL35 promoted metastatic burden in breast cancer *in vivo,* and RPL15 overexpression also promoted the translation of core ribosomal proteins [295].

One possible explanation for our results is that inducing *NLE1* for 4 to 8 days was not long enough to affect ribosome biogenesis and promote protein synthesis. Maybe a permanent overexpression could be used instead. Furthermore, cells could have reached already a plateau phase where even more NLE1 does not increase ribosome biogenesis. Ribosome biogenesis is a complex process involving many different proteins. If there was an excess of NLE1 but not of other ribosomal components, no more ribosomes could be generated. Hence, proliferation was not accelerated. In cancer cells, the most likely way NLE1 expression could promote proliferation is in combination with other factors. Usually, cancer cells do not show expression changes in only a single protein but in a

large number of proteins. This would also fit our TGF-β rescue experiment, where we showed that NLE1 alone could not rescue growth inhibition by TGF-β. Combined with other ribosomal proteins (NAT10, FBL, RRP1), overexpression might rescue the TGF-β-mediated growth inhibition. Additional experiments are required to investigate how the interplay of different ribosomal proteins promotes cancer progression over a long time.

6.4. NLE1 deficiency causes p38/MAPK-phosphorylation, impaired autophagy, and increased ROS levels in CRC cells

Considering that inhibition of protein synthesis is associated with ribotoxic stress response (RSR) pathways and thereby promotes apoptosis, we investigated the downstream effects of *NLE1* ablation in CRC cell lines [254, 255]. We observed that *NLE1* knockout cells activated p38/MAPK but not JNK signaling. Moreover, NLE1-deficient cells showed impaired autophagy and increased ROS levels compared to their wild-type counterparts.

This is in line with observations made by others. In 2011, Kim *et al.* described that the knockdown of *RPS3* and *RPS6* induced ribosomal stress and activated p38/MAPK signaling, as shown by the phosphorylation of p38. They also showed that JNK was not phosphorylated during *RPS3* depletion [296]. Another example of how p38/MAPK signaling becomes activated is when cells are treated with doxorubicin or cycloheximide, two drugs that inhibit protein biosynthesis. Nevertheless, in contrast to the study of Kim *et al.*, JNK signaling was also activated upon exposure of cells to these compounds [297-300]. Furthermore, inhibition of protein synthesis by drugs or genetic loss-of-function studies led to impaired autophagy. For example, cycloheximide treatment inhibited autophagic degradation and lysosomal enzyme delivery [256]. In accordance, the loss of RPL3 in colon cancer cells enhanced autophagosome and lysosome formation [301]. Knockdown of ribosomal protein lateral stalk subunit P0 (*RPLP0*), ribosomal protein lateral stalk subunit P1 (*RPLP1*), and ribosomal protein lateral stalk subunit P2 (*RPLP2*) in a breast cancer cell line (MCF-7) led to an accumulation of autophagosomes [302]. This accumulation was accompanied by ROS production. When ROS production was inhibited, the growth capacity of the cancer cells could be restored [302]. Knockdown of *RPS19* in HEK293 cells resulted in a similar phenotype [303].

Based on our results and the previous literature, we hypothesize that NLE1 deficiency causes impaired autophagy and accumulation of ROS. This might provide feedback on p38/MAPK signaling and could affect cellular fitness. However, additional experiments are necessary to prove this hypothesis. First, it should be investigated how these events are connected and in which order they occur. Therefore experiments with p38 inhibitors and/or N-acetyl-cysteine (NAC), a ROS scavenger, should be performed to investigate if the stress response triggered by NLE1 loss can be rescued and, thereby, apoptosis can be

prevented in CRC cell lines. Second, it should be investigated if PDTOs also respond with impaired autophagy, ROS accumulation, and p38 phosphorylation to NLE1 loss. However, these features are difficult to address in PDTOs, since organoids are embedded in Matrigel, which needs to be dissolved before one can analyze the abundance of these short-lived molecular states. Especially, phosphorylation sites such as p38 could be lost already during the procedure because of their short half-life. Also, FACS analysis of ROS in PDTOs is not feasible because one would need much material to quantify this. Third, other possible downstream pathways should be investigated because the organoid medium already contains a p38 inhibitor and NAC, and still, PDTOs massively died shortly after NLE1 loss. This implies that other mechanisms are involved in the observed phenotype. One could establish a conditional knock-out system to circumvent the massive deterioration of cells after the ablation of *NLE1*. Hence, it would be possible to analyze the direct effects of NLE1 loss in PDTOs and to have enough material for flow cytometry-based assays.

6.5. Knockout of *NLE1* reduces tumor burden and metastasis in an orthotopic mouse transplantation model

Since *NLE1* ablation reduced the self-renewal and growth capacity of PDTOs *in vitro*, we decided to elucidate this effect *in vivo*. Indeed, mice transplanted with *NLE1* knockout PDTOs formed on average smaller tumors and had less distant metastases in the liver than their wild-type counterparts.

Following our results, other studies confirmed the relevance of ribosomal proteins for tumor growth and metastasis *in vivo*. For example, mice subcutaneously transplanted with SGC7901 cells, a gastric cancer cell line transfected with siRNA against *RPL15*, showed a massive reduction in tumor size [304]. Shi *et al.* observed that *RPL15* knockdown in hepatocellular carcinoma cells led to tumor reduction [294]. Bee *et al.* also investigated if the knockdown of *RPL19* in prostate cancer cells leads to the same effect. Indeed, tumor size was reduced in this study [305]. This phenotype was also reflected by treatment with the RNA Pol I inhibitor CX-5461. It showed strong effects in several studies [285, 306]. Besides the loss of function and treatment studies, the gain of function studies also support our hypothesis. When RPL15 or RPL35 were overexpressed in circulating tumor cells (CTCs), which had been delivered into mice by tail vein injection, the metastatic burden increased. In contrast, overexpression of RPL8 or RPL13 did not increase the metastatic burden. Therefore not all ribosomal proteins promoted a pro-metastatic phenotype [295]. The importance of these genes could also be reflected in human settings. When gene expression profiles from human primary and metastatic triple-negative breast cancer (TNBC) tissues were compared, many ribosomal proteins were upregulated, especially *RPL27A* and *RPL15* [291].

In our *in vivo* approach, we could not exclude that the decreased primary tumor burden observed in mice transplanted with PDTOs deficient for NLE1 represented a substantial confounder variable. It can be anticipated that the chance for tumor dissemination in an already advanced, big tumor was higher than in a small tumor. Therefore one should test the effect of *NLE1* expression in other tumor models. For example, *NLE1* wild-type and knockout cells could be transplanted via tail vein injection and then monitored for metastatic onset. The advantage is that the same number of cells are delivered into the bloodstream, and only extravasation and lung colonization capacity are quantified. However, the disadvantage is that the tumor cells preferentially metastasize into the lung independently of the investigated tumor entity. Crucial steps such as intravasation are missing [307]. Therefore, it is not a suitable model for liver metastasis. Another model system to investigate metastatic spreading in CRC *in vivo* was recently developed in Eduard Batlle's lab: Canellas-Socias *et al.* resected the primary tumor after a given time and investigated metastatic lesions' recurrence [219]. The significant advantage of this model is that mice do not die from the primary tumor and have more time to develop metastatic lesions. We could exclude the confounder variable we observed in our study. To that, one could remove the *NLE1* knockout tumor when it has reached the same size as the *NLE1* wild-type tumor and then determine if the *NLE1* knockout tumor spawns the same number of metastatic cells as the *NLE1* wild-type tumor does.

We conclude that *NLE1* expression limits primary tumor growth and metastasis in CRC *in vivo.* However, it remains to be shown how this elevated *NLE1* expression confers an advantage during the different stages of metastasis. For example, NLE1 could alter the expression of ECM-degrading proteins and thereby promote the cancer cells' migratory capacity, similar to a study by Yang *et al.* They showed that RPL23 facilitated metastasis in hepatocellular carcinoma (HCC) via enhancing matrix metallopeptidase 9 (*MMP9*) mRNA stability [308]. MMP9 is an enzyme that can degrade ECM and thereby promotes metastasis [309].

Another possibility might be enhanced survival of NLE1 high-expressing tumor cells. During the establishment of metastasis at secondary sites, most tumor cells undergo apoptosis within 24 hours. Therefore tumor cells must acquire resistance mechanisms to apoptosis [310]. In 2019, Liu *et al.* observed that RPS15A promoted gastric cancer progression via activation of the Akt/inhibitor of nuclear factor kappa B kinase subunit β/nuclear factor κ-light-chain-enhancer of activated B cells (Akt/IKK-β/NF-κB) signaling pathway [311]. NF-κB is a crucial transcription factor that activates anti-apoptotic genes such as CASP8 and FADD-like apoptosis regulator (CFLAR), B-cell lymphoma-extra large (BCL-xL), Myeloid cell leukemia 1 (MCL1), and cellular inhibitor of apoptosis proteins (cIAPs), thereby promoting cell survival [312, 313]. One could hypothesize that high expression of NLE1 might lead to similar effects.

However, one has to consider that ectopic expression of NLE1 had no apparent effect on tumor cells, and its expression is enhanced in the context of an overall elevated signature of biosynthetic and proliferative capacity. Hence, NLE1 might represent one component of a large panel of proteins, which together confer enhanced fitness, plasticity, and migration capacity to tumor cells. Further studies are necessary to investigate this in detail.

6.6. *NLE1* levels are increased in Wnt/MYC-expressing CRC molecular subtypes and predict survival in CRC patients

Our previous results questioned whether *NLE1* expression also correlates with patient characteristics. *NLE1* expression was higher in CRC tumors than in normal tissue and correlated with increased relapse-free survival in CRC patients. Interestingly, *NLE1* was mainly expressed in CMS2 and CRIS-C/D subtypes, whereas the lowest was observed in CMS4 and CRIS-B.

The upregulation of ribosomal proteins was already described in various tumor entities [289, 292, 304, 314]. Wang *et al.* reported upregulation of RPL15 in gastric cancer patients [304]. The same was observed for CRC patients [289]. Further examples were the upregulation of RPL34 in osteosarcoma or RPS11 in kidney renal cell carcinoma (KIRC) [292, 314]. These examples show that the upregulation of ribosomal proteins is a common phenomenon in cancer cells and represents an essential feature for cancer progression. In addition, the correlation between high *NLE1* mRNA levels and increased relapse-free survival in CRC patients fits previous studies where high c-MYC expression correlated with better overall and progression-free survival in CRC patients [315, 316]. This is because fast proliferating cells (c-MYC high) respond better to “Standard of Care” (SoC) patient treatments [317, 318]. Since *NLE1* was induced by c-MYC and correlated positively with c-MYC expression, it was not surprising that patients with high *NLE1* expression also showed an increased relapse-free survival. Our observation also supported that *NLE1* was highly expressed in CMS2 and CRIS-C/D subtypes of CRC patients characterized by c-MYC activation. In contrast, the high expression of ribosomal proteins, such as *RPL19* in prostate cancer or *RPL27A* in hepatocellular carcinoma, was shown to correlate with poor survival [319, 320]. The reasons for these differences are difficult to define. The expression of every single gene is tissue-dependent and, therefore, might act differently in other tumor entities. Furthermore, when these genes are independent of c-MYC regulation, they probably show other expression patterns. Recent literature also showed that CMS4-classified CRC cells are more resistant to oxaliplatin and 5'-fluorouracil (5-FU) based chemotherapies, which are well known to provoke ribosomal stress [321-323]. This would fit our observation that *NLE1* levels were lowest in CMS4 and CRIS-B, associated with active TGF-β signaling and poor patient prognosis

[235, 236]. It is possible that *de novo* protein biosynthesis is relatively lower in these molecular subtypes. This would imply that they might respond less to chemotherapeutic agents that partially rely on provoking ribosomal stress. Therefore, maybe other agents are more valuable. For example, irinotecan-based combination therapies were shown to be more effective in the CMS4 subtype of CRC patients [324].

However, future studies should investigate how different *NLE1* levels correlate with responsiveness to different types of chemotherapy in CRC patients.

6.7. Loss of TP53 sensitizes NLE1-deficient, microsatellite-instable CRC cells to apoptosis

Chromosomally instable CRC patients often show inactivation or loss of the tumor suppressor protein TP53, which gets activated during nucleolar stress. In contrast, microsatellite instable CRC patients often retain wild-type TP53. Therefore, we wondered what effect the loss of *NLE1* expression has on CRC cells, dependent on their *TP53* status, and if it could represent a potential target for CRC therapy [269, 270]. Indeed, wild-type TP53 prevented microsatellite instable HCT116 cells from NLE1-loss mediated apoptosis by induction of p21. Interestingly, the *TP53* status did not correlate with *NLE1* expression in CRC patients, and deletion of *NLE1* in *TP53* mutated chromosomally stable HT-29 and SW620 cells also led to the induction of p21, even though these cell lines underwent apoptosis upon NLE1 loss.

It was already described that the disruption of rRNA or ribosomal protein synthesis, processing, transport, assembly, or function led to TP53 stabilization and transactivation of TP53 target genes [325]. For example, depletion of LAS1-like ribosome biogenesis factor (*LAS1L*), which is involved in the biogenesis of the 60S ribosomal subunit, in *TP53* wild-type HCT116 cells led to stabilization of TP53, induction of p21, and a G1-mediated cell cycle arrest. This was not observed in *TP53* knockout HCT116 cells [326, 327]. Sun *et al.* reported similar effects when *RPL29* or *RPL30* were depleted in the osteosarcoma cell line U2OS. They observed a clear induction of p21 and stabilization of TP53 in *TP53* wild-type U2OS cells, whereas *TP53* knockout U2OS cells failed to induce p21. Their proliferation rates also reflected this: *TP53* wild-type U2OS cells with *RPL29* or *RPL30* knockdown showed a substantial growth reduction. In contrast, *TP53* knockout U2OS cells showed no differences in overall proliferation upon *RPL29* or *RPL30* knockdown [328]. These data follow our observations after the loss of NLE1 in *TP53* wild-type and *TP53* knockout HCT116 cells. Since NLE1 also interacts with the Rix1 complex as LAS1L does, we hypothesize that the loss of NLE1 may lead to a similar transcriptional survival program as the loss of LAS1L [329].

Next, a correlation analysis between *TP53* status and the expression of ribosomal proteins in cancer is still missing. Only one publication from Marcel *et al.* demonstrated that fibrillarin (FBL) expression is inversely associated with TP53 activity in cell lines and human breast cancer samples [165]. Fibrillarin is essential for the processing of pre-rRNAs. It functions as a methyltransferase via 2'-O-ribose-methylation [330, 331]. In detail, TP53 could directly bind to the *FBL* promoter, thereby repressing its expression. During the loss of TP53, FBL levels were increased and contributed to tumor progression. Unfortunately, this correlation was not significant in breast cancer patients. Only a trend was discernible [165]. Hence, it is not easy to define possible reasons for this observation. Translation of *in vitro* experiments into the clinic is always challenging. Many cell lines are polyclonal and have adapted to the mostly non-physiological conditions imposed by *in vitro* culture conditions. Therefore, they do, in most cases, not behave like the tumor from which they were derived. Also, there is no influence from the tumor microenvironment (TME) in cultured cell lines. Similar arguments on organoids are discussed; only early passages might mimic the actual disease well. In contrast, other cell types also contribute to the tumor mass in patients. This can then influence the results of the gene expression profiles used for the correlation analysis. Furthermore, expression levels are compared between *TP53* mutant and *TP53* wild-type patients. Here, the problem is that different patients are compared with each other. Different patients have different genetic backgrounds and are unique in their gene expression profiles. If one patient acquires a higher ribosomal gene expression by *TP53* mutation, this expression could still be as high as in a different *TP53* wild-type patient. This is possible because this *TP53* wild-type patient generally has a higher level of this ribosomal gene than the *TP53* mutant patient. Therefore, an isogenic model is necessary to obtain unequivocal evidence. Future studies could isolate PDTOs from *TP53* wild-type patients and then introduce *TP53* mutations to see how this influences the expression of ribosomal genes.

Unexpectedly, the deletion of *NLE1* in *TP53* mutated cells (HT29, SW620) led also to the induction of p21. Still, it fits previous literature because nucleolar stress can result in TP53-independent activation of cell cycle control mechanisms [332-334]. Donati *et al.* depleted RNA polymerase I subunit A (*POLR1A*) in U2OS and HCT-116 cells (both *TP53* wild-type) and observed TP53 stabilization, induction of p21, and cell cycle arrest, similar to what we observed upon deletion of *NLE1*. Furthermore, *TP53* was silenced in both cell lines, and Donati *et al.* observed a similar phenotype to the *TP53* wild-type cells. Even introducing a dominant negative inactive form of murine *Tp53* in HCT116 cells resulted in the same phenotype. Therefore, silencing of *POLR1A* leads to cell cycle arrest in a TP53-independent manner. Responsible for this phenotype was that silencing *POLR1A* led to reduced E2F transcription factor 1 (E2F1) expression. This then hindered cell cycle progression in a retinoblastoma protein (pRB)-dependent manner in *TP53* wild-type cells [333]. Moreover, the depletion of pescadillo, which is part of the PeBoW

complex, in *TP53* knockout (MDA-MB-435) and *TP53* wild-type (ZR-75-30) breast cancer cells resulted in cell cycle arrest [332, 335, 336]. This cell cycle arrest was mediated by decreased expression of cyclin D1, upregulation of cyclin-dependent kinase inhibitor 1B (CDKN1B/$p27^{Kip1}$), and reduction of pRB phosphorylation [332]. In line with these examples, we conclude that *NLE1* deletion in *TP53* mutant CRC cells causes p21 induction, but the underlying mechanism needs further investigation. For example, one could investigate if a reduction in E2F1 expression or pRB phosphorylation might be responsible for the observed phenotype.

Furthermore, it is unclear how this p21 induction in NLE1-deficient HT29 and SW620 cells is connected to the elevated levels of apoptosis previously observed in NLE1-deficient HT29 and SW620 cells. Since both cell lines are mutated in *TP53*, we expected that they do not induce p21 upon NLE1 loss, as HCT116 *TP53* knockout cells did. One possible explanation could be that TP53 in HT29 and SW620 cells still has some residual activity compared to the complete knockout of *TP53* in HCT116 cells. Therefore target genes such as *p21* can still be induced partially.

However, further experiments should investigate the downstream effects of NLE1 loss in cancer cells dependent on their *TP53* status and how this can be exploited for therapeutic targeting of CRC in a clinical setting.

6.8. Deletion of *NLE1* provokes cell cycle arrest rather than apoptosis in immortalized human colonic cells (HCEC-1CT)

To investigate whether NLE1 could be used for therapeutic targeting of CRC, we performed deletion of *NLE1* in immortalized benign human colonic epithelial cells. Surprisingly, *NLE1* ablation induced cell cycle arrest rather than apoptosis in this cellular context, although *de novo* protein biosynthesis was diminished.

This aligns with a recent study from Dong *et al.*: This group investigated the effects of *RPL15* knockdown in human retinal pigment epithelial-1 (RPE-1) cells. Analysis of cell growth revealed a decrease in the proliferation rate of RPL15-deficient RPE-1 cells but not a complete inhibition. This was also reflected in their cell cycle analysis: Ablation of *RPL15* led to an increased accumulation of cells in the G1 to G1/S phase and induction of p21. To investigate apoptosis induction, they performed Annexin V/PI staining and immunoblot analysis. Interestingly, RPL15-deficient RPE-1 cells showed no increase in Annexin V/PI staining and no induction of cleaved caspase 3 [289]. In accordance, inhibition of protein synthesis by the RNA Pol I inhibitor CX-5461 resulted in a substantial decrease in cell viability of tumor organoids, whereas normal organoids responded less sensitively [293]. CX-5461 was already tested in clinical trials for patients with advanced hematological cancers and different solid tumors [337, 338]. These

examples show that targeting ribosome biogenesis factors is feasible and can help overcome limitations such as toxicity and specificity during drug development. Especially toxicity is a common problem in drug development because patients do not tolerate the dose necessary to affect tumor growth positively. Specificity is also problematic because the drug should not damage normal cells, which might also depend on the nature of the target [339, 340]. Therefore, drug development is a time-consuming and complex process [341].

Regarding NLE1, one must find a strategy to tackle its expression. Therefore, a good understanding of NLE1 and its' interaction partners is necessary. For example, NLE1 interacts with Midasin during ribosome maturation [136, 140, 141]. To develop small molecules or peptide drugs that inhibit this interaction, a structure-guided drug development approach, as described by Orea-Ordóñez *et al.,* might be helpful [342]. They developed specific peptides that interfere between Erb1 and Ytm1, the yeast homologs to BOP1 and WDR12 [136, 342, 343]. NOP7 (mammals: PeBoW) complex formation was prevented, and ribosome biogenesis was blocked [342]. Another possibility to target NLE1 could be a proteolysis-targeting chimera (PROTAC). PROTACs are heterobifunctional small molecules with two active domains and a linker. One domain binds to the target protein, which should be degraded; the other domain mediates specific ubiquitination, leading to the degradation of the target protein. One famous example of their use is mutant KRAS, previously described as "undruggable" [344]. Hence, PROTACs might be an effective way to treat abnormally high levels of NLE1 in CRC. A third strategy to suppress *NLE1* expression might be siRNAs or microRNAs. siRNA or microRNA are delivered into the cell by nano-carriers and initiate the degradation of complementary mRNA molecules via the cells internal machinery. This results in reduced gene expression [345]. A successful example has already been established. Sendi *et al.* developed a galactose-targeted lipid calcium phosphate (Gal-LCP) nanoformulation of miR-122 and could show that it effectively prevented CRC derived liver metastasis [346].

In conclusion, our study revealed that loss of SMAD4 in PDTOs induces c-MYC-mediated upregulation of NLE1, thereby contributing to tumor growth and metastasis in CRC. Furthermore, ablation of *NLE1* in TP53 proficient cancer and normal human colonic epithelial cells led to cell cycle arrest rather than apoptosis. This provides the opportunity that therapeutic targeting of NLE1 could present a feasible strategy to tackle CRC. Therefore, future studies should aim to develop drugs directed against NLE1 or its interaction partners and validate their applicability for treating CRC.

7. Summary

TGF-β signaling plays an essential role in colorectal cancer (CRC) progression. Patients frequently suffer from mutations in the *TGFBR2* gene or deletions of *SMAD4*. These mutations correlate with a poorer survival rate in CRC patients. How these genetic changes contribute to tumor growth and metastatic spread is not fully understood. Thus, an in-depth analysis of the gene expression profiles of CRC patients acquiring a *SMAD4* deletion could help to identify new therapeutic options.

Here, we used the CRISPR/Cas9 approach to introduce a deletion of *SMAD4* in patient-derived tumor organoids (PDTOs) and investigate their effect on the gene expression profile when exposed to a TGF-β-rich environment. Thereby, we could observe that SMAD4-deficient PDTOs acquire an enrichment in the expression of c-MYC target genes and human colonic stem cell gene sets. Only 11 of the 284 deregulated genes (*FBL, GINS2, IFITM3, LSM6, MYC, NAT10, NLE1, POLR3K, PRMT1, PSMG4, RRP1*) confer an advantage for tumor cell fitness according to DepMap. Four of these genes (*FBL*, *NAT10*, *NLE1*, *RRP1*) are part of ribosome biogenesis. They might contribute to the increased protein biosynthesis levels observed in advanced CRC. Since the role of NLE1 in the progression of CRC is not fully understood, we decided to focus our studies on the regulation and function of NLE1 in CRC.

We found that *NLE1* expression was upregulated upon SMAD4 loss in TGF-β-exposed PDTOs and that c-MYC can bind to the promoter of *NLE1*. Thereby, c-MYC prevents TGF-β-mediated downregulation of *NLE1*. Furthermore, *NLE1* levels were higher in different CRC cohorts than in normal tissues and significantly enriched in Wnt/MYC CRC molecular subtypes. After the deletion of *NLE1* in different CRC cell lines and PDTOs, we could observe an apparent reduction in *de novo* protein biosynthesis rates. In accordance, the deletion of *NLE1* also resulted in slower proliferation kinetics, reduced colony formation, and less anchorage-independent growth in CRC cell lines. Moreover, *NLE1* knockout cells showed higher levels of apoptosis, a reduced migratory/invasive capacity, and underwent cell cycle arrest and apoptosis. In the case of PDTOs, smaller organoid sizes and reduced clonogenicity during the loss of NLE1 were observed. This phenotype was also reflected in an endoscopy-guided orthotopic mouse transplantation model. Primary tumors lacking *NLE1* expression were smaller than *NLE1* wild-type derived tumors, and the affected animals showed less metastatic burden in the liver. As a downstream effect, NLE1-deficient cells showed activation of p38/MAPK, accumulation of p62- and LC3-positive structures, which defines impaired autophagy, and higher ROS levels. Furthermore, deletion of *NLE1* in TP53 proficient cancer and normal human colonic epithelial cells led to cell cycle arrest rather than apoptosis, and *NLE1* mRNA levels predicted relapse-free survival in CRC patients.

In summary, we could show that a TGF-β/SMAD4/c-MYC axis regulates NLE1 and represents a limiting factor for *de novo* protein biosynthesis and the tumorigenic potential of advanced CRC. To which extent therapeutic targeting of NLE1 can be used as a treatment of CRC in a clinical setting warrants further investigation.

8. Zusammenfassung

Der TGF-β Signalweg spielt eine zentrale Rolle bei der Entstehung von Darmkrebs. Häufig zeigen Patienten Mutationen im TGFBR2 Gen oder Deletionen von SMAD4. Diese Mutationen korrelieren mit einer schlechten Überlebensrate von Darmkrebspatienten. Wie diese genetischen Veränderungen zum Tumorwachstum und zur Ausbreitung von Metastasen beitragen, ist bisher nicht vollständig verstanden. Daher könnte eine umfassende Analyse der Genexpressionsprofile von Darmkrebspatienten, die eine SMAD4-Deletion erwerben, helfen, neue therapeutische Ansätze zu identifizieren.

Zunächst wurde mittels CRISPR/Cas9 eine Deletion von SMAD4 in Patienten-abgeleiteten Tumororganoiden (PDTOs) eingeführt, um dann ihre Wirkung auf das Genexpressionsprofil zu untersuchen, wenn sie einer TGF-β reichen Umgebung ausgesetzt sind. Dabei konnten wir beobachten, dass SMAD4-defiziente PDTOs eine Anreicherung für c-MYC-Zielgene und humane Kolonstammzellgene erwerben. Interessanterweise zeigten nur 11 der 284 deregulierten Gene (FBL, GINS2, IFITM3, LSM6, MYC, NAT10, NLE1, POLR3K, PRMT1, PSMG4, RRP1) einen Vorteil für die Fitness von Tumorzellen. 4 dieser Gene (FBL, NAT10, NLE1, RRP1) sind Teil der Ribosomenbiogenese und könnten zu einer erhöhten Proteinbiosynthese beitragen, die bei fortgeschrittenem Darmkrebs beobachtet wird. Da die Rolle von NLE1 beim Fortschreiten von Darmkrebs noch nicht vollständig geklärt ist, hatten wir uns entschlossen, unseren Fokus daraufzulegen.

Dabei fanden wir heraus, dass die Expression von NLE1 nach SMAD4 Verlust in TGF-β-exponierten PDTOs hochreguliert wurde und dass c-MYC in der Lage ist, an den Promotor von NLE1 zu binden. Dadurch verhindert c-MYC das TGF-β-vermittelte Herunterregeln von NLE1. Darüber hinaus war die Expression von NLE1 in verschiedenen Kohorten von Darmkrebspatienten höher im Vergleich zu Normalgewebe und insbesondere in Wnt/MYC Subgruppen von Darmkrebspatienten angereichert. Nach Deletion von NLE1 in verschiedenen kolorektalen Krebszelllinien und PDTOs konnten wir eine deutliche Reduktion der *de-novo*-Proteinbiosyntheseraten beobachten. Dementsprechend führte die Deletion von NLE1 auch zu einer langsameren Proliferationskinetik, weniger Koloniebildung und weniger verankerungsunabhängigem Wachstum in kolorektalen Krebszelllinien. Darüber hinaus zeigten NLE1-defiziente Zellen verstärkt Apoptose, eine geringere Migrations-/Invasionskapazität und einen Stillstand des Zellzyklus. Bei den PDTOs wurde eine kleinere Organoidgröße und eine verringerte Klonogenität nach Verlusts von NLE1 beobachtet. Dieser Phänotyp spiegelte sich auch in einem Endoskopie-gestützten orthotopen Maustransplantationsmodell wieder. Primärtumore von NLE1-defizienten Zellen waren im Vergleich zu Tumoren, die vom NLE1 Wildtyp Zellen stammten, kleiner und zeigten auch eine geringere Fähigkeit zur Ausbildung von Metastasen in der Leber. Des Weiteren zeigten NLE1-defiziente

Zellen eine Aktivierung von p38/MAPK, eine Akkumulation von p62- und LC3-positiven Strukturen, was eine beeinträchtigte Autophagie definiert, und vermehrt oxidativen Stress. Darüber hinaus führte die Deletion von NLE1 in TP53 Wildtyp Krebs- und normalen menschlichen Dickdarmepithelzellen eher zu einem Zellzyklusstillstand als zu Apoptose, und die NLE1 mRNA Expression prognostizierte ein Rezidiv-freies Überleben bei Darmkrebspatienten.

Zusammenfassend konnte gezeigt werden, dass NLE1 durch eine TGF-β/SMAD4/c-MYC-Achse reguliert wird und ein limitierender Faktor für die *de-novo*-Proteinbiosynthese und das tumorogene Potenzial von fortgeschrittenem Darmkrebs darstellt. Inwieweit eine Blockierung von NLE1 als therapeutischer Ansatzpunkt im Darmkrebs dienen kann, müssen weitere Studien erst noch zeigen.

9. References

1. Sung, H., et al., *Global Cancer Statistics 2020: GLOBOCAN Estimates of Incidence and Mortality Worldwide for 36 Cancers in 185 Countries.* CA Cancer J Clin, 2021. **71**(3): p. 209-249.
2. Siegel, R.L., et al., *Cancer statistics, 2022.* CA Cancer J Clin, 2022. **72**(1): p. 7-33.
3. Hanahan, D., *Hallmarks of Cancer: New Dimensions.* Cancer Discov, 2022. **12**(1): p. 31-46.
4. Hanahan, D. and R.A. Weinberg, *The hallmarks of cancer.* Cell, 2000. **100**(1): p. 57-70.
5. Hanahan, D. and R.A. Weinberg, *Hallmarks of cancer: the next generation.* Cell, 2011. **144**(5): p. 646-74.
6. Dvorak, H.F., et al., *Induction of a fibrin-gel investment: an early event in line 10 hepatocarcinoma growth mediated by tumor-secreted products.* J Immunol, 1979. **122**(1): p. 166-74.
7. Dvorak, H.F., *Tumors: wounds that do not heal. Similarities between tumor stroma generation and wound healing.* N Engl J Med, 1986. **315**(26): p. 1650-9.
8. Warburg, O., *On the origin of cancer cells.* Science, 1956. **123**(3191): p. 309-14.
9. Warburg, O., *On respiratory impairment in cancer cells.* Science, 1956. **124**(3215): p. 269-70.
10. *The Metabolism of Tumours: Investigations from the Kaiser Wilhelm Institute for Biology, Berlin-Dahlem.* Journal of the American Medical Association, 1931. **96**(23): p. 1982-1982.
11. Hayflick, L., *The Limited in Vitro Lifetime of Human Diploid Cell Strains.* Exp Cell Res, 1965. **37**: p. 614-36.
12. Hayflick, L. and P.S. Moorhead, *The serial cultivation of human diploid cell strains.* Exp Cell Res, 1961. **25**: p. 585-621.
13. Hwang, H.J., et al., *Endothelial cells under therapy-induced senescence secrete CXCL11, which increases aggressiveness of breast cancer cells.* Cancer Lett, 2020. **490**: p. 100-110.
14. Dekker, E., et al., *Colorectal cancer.* Lancet, 2019. **394**(10207): p. 1467-1480.
15. Guren, M.G., *The global challenge of colorectal cancer.* Lancet Gastroenterol Hepatol, 2019. **4**(12): p. 894-895.
16. Keum, N. and E. Giovannucci, *Global burden of colorectal cancer: emerging trends, risk factors and prevention strategies.* Nat Rev Gastroenterol Hepatol, 2019. **16**(12): p. 713-732.
17. Xi, Y. and P. Xu, *Global colorectal cancer burden in 2020 and projections to 2040.* Transl Oncol, 2021. **14**(10): p. 101174.
18. Jasperson, K.W., et al., *Hereditary and familial colon cancer.* Gastroenterology, 2010. **138**(6): p. 2044-58.
19. Tian, Y., et al., *Familial colorectal cancer risk in half siblings and siblings: nationwide cohort study.* BMJ, 2019. **364**: p. l803.

20. Lichtenstein, P., et al., *Environmental and heritable factors in the causation of cancer--analyses of cohorts of twins from Sweden, Denmark, and Finland.* N Engl J Med, 2000. **343**(2): p. 78-85.

21. Muller, M.F., A.E. Ibrahim, and M.J. Arends, *Molecular pathological classification of colorectal cancer.* Virchows Arch, 2016. **469**(2): p. 125-34.

22. Graff, R.E., et al., *Familial Risk and Heritability of Colorectal Cancer in the Nordic Twin Study of Cancer.* Clin Gastroenterol Hepatol, 2017. **15**(8): p. 1256-1264.

23. Norat, T., et al., *Meat consumption and colorectal cancer risk: dose-response meta-analysis of epidemiological studies.* Int J Cancer, 2002. **98**(2): p. 241-56.

24. Schmid, D. and M.F. Leitzmann, *Television viewing and time spent sedentary in relation to cancer risk: a meta-analysis.* J Natl Cancer Inst, 2014. **106**(7).

25. Tabung, F.K., et al., *Association of Dietary Inflammatory Potential With Colorectal Cancer Risk in Men and Women.* JAMA Oncol, 2018. **4**(3): p. 366-373.

26. Amin, M.B., et al., *AJCC Cancer Staging Manual*. 2018: Springer International Publishing.

27. Sinkovics, J.G., *RNA/DNA and Cancer*. 2016: Springer International Publishing.

28. Grady, W.M. and J.M. Carethers, *Genomic and epigenetic instability in colorectal cancer pathogenesis.* Gastroenterology, 2008. **135**(4): p. 1079-99.

29. Lengauer, C., K.W. Kinzler, and B. Vogelstein, *Genetic instability in colorectal cancers.* Nature, 1997. **386**(6625): p. 623-7.

30. Fearon, E.R. and B. Vogelstein, *A genetic model for colorectal tumorigenesis.* Cell, 1990. **61**(5): p. 759-67.

31. Pinto, D. and H. Clevers, *Wnt, stem cells and cancer in the intestine.* Biol Cell, 2005. **97**(3): p. 185-96.

32. Markowitz, S.D. and M.M. Bertagnolli, *Molecular origins of cancer: Molecular basis of colorectal cancer.* N Engl J Med, 2009. **361**(25): p. 2449-60.

33. Behrens, J., et al., *Functional interaction of beta-catenin with the transcription factor LEF-1.* Nature, 1996. **382**(6592): p. 638-42.

34. Molenaar, M., et al., *XTcf-3 transcription factor mediates beta-catenin-induced axis formation in Xenopus embryos.* Cell, 1996. **86**(3): p. 391-9.

35. He, T.C., et al., *Identification of c-MYC as a target of the APC pathway.* Science, 1998. **281**(5382): p. 1509-12.

36. Schneikert, J. and J. Behrens, *The canonical Wnt signalling pathway and its APC partner in colon cancer development.* Gut, 2007. **56**(3): p. 417-25.

37. Vogelstein, B., et al., *Genetic alterations during colorectal-tumor development.* N Engl J Med, 1988. **319**(9): p. 525-32.

38. Zhu, G., et al., *Role of oncogenic KRAS in the prognosis, diagnosis and treatment of colorectal cancer.* Mol Cancer, 2021. **20**(1): p. 143.

39. Bos, J.L., et al., *Prevalence of ras gene mutations in human colorectal cancers.* Nature, 1987. **327**(6120): p. 293-7.

40. Downward, J., *Ras signalling and apoptosis.* Curr Opin Genet Dev, 1998. **8**(1): p. 49-54.

41. Chen, J., et al., *BRAF V600E mutation and KRAS codon 13 mutations predict poor survival in Chinese colorectal cancer patients.* BMC Cancer, 2014. **14**: p. 802.

42. Li, W., et al., *Colorectal carcinomas with KRAS codon 12 mutation are associated with more advanced tumor stages.* BMC Cancer, 2015. **15**: p. 340.

43. Davies, H., et al., *Mutations of the BRAF gene in human cancer.* Nature, 2002. **417**(6892): p. 949-54.

44. Weisenberger, D.J., et al., *CpG island methylator phenotype underlies sporadic microsatellite instability and is tightly associated with BRAF mutation in colorectal cancer.* Nat Genet, 2006. **38**(7): p. 787-93.

45. Baker, S.J., et al., *p53 gene mutations occur in combination with 17p allelic deletions as late events in colorectal tumorigenesis.* Cancer Res, 1990. **50**(23): p. 7717-22.

46. Baker, S.J., et al., *Chromosome 17 deletions and p53 gene mutations in colorectal carcinomas.* Science, 1989. **244**(4901): p. 217-21.

47. Baker, S.J., et al., *Suppression of human colorectal carcinoma cell growth by wild-type p53.* Science, 1990. **249**(4971): p. 912-5.

48. Vazquez, A., et al., *The genetics of the p53 pathway, apoptosis and cancer therapy.* Nat Rev Drug Discov, 2008. **7**(12): p. 979-87.

49. Fearon, E.R., et al., *Identification of a chromosome 18q gene that is altered in colorectal cancers.* Science, 1990. **247**(4938): p. 49-56.

50. Grady, W.M., et al., *Mutation of the type II transforming growth factor-beta receptor is coincident with the transformation of human colon adenomas to malignant carcinomas.* Cancer Res, 1998. **58**(14): p. 3101-4.

51. Mehrvarz Sarshekeh, A., et al., *Association of SMAD4 mutation with patient demographics, tumor characteristics, and clinical outcomes in colorectal cancer.* PLoS One, 2017. **12**(3): p. e0173345.

52. Alazzouzi, H., et al., *SMAD4 as a prognostic marker in colorectal cancer.* Clin Cancer Res, 2005. **11**(7): p. 2606-11.

53. Yan, P., et al., *Reduced Expression of SMAD4 Is Associated with Poor Survival in Colon Cancer.* Clin Cancer Res, 2016. **22**(12): p. 3037-47.

54. Zhang, B., et al., *Loss of Smad4 in colorectal cancer induces resistance to 5-fluorouracil through activating Akt pathway.* Br J Cancer, 2014. **110**(4): p. 946-57.

55. Fumagalli, A., et al., *Genetic dissection of colorectal cancer progression by orthotopic transplantation of engineered cancer organoids.* Proc Natl Acad Sci U S A, 2017. **114**(12): p. E2357-E2364.

56. Boland, C.R., et al., *A National Cancer Institute Workshop on Microsatellite Instability for cancer detection and familial predisposition: development of international criteria for the determination of microsatellite instability in colorectal cancer.* Cancer Res, 1998. **58**(22): p. 5248-57.

57. Boland, C.R. and A. Goel, *Microsatellite instability in colorectal cancer.* Gastroenterology, 2010. **138**(6): p. 2073-2087 e3.

58. Fishel, R., et al., *The human mutator gene homolog MSH2 and its association with hereditary nonpolyposis colon cancer.* Cell, 1993. **75**(5): p. 1027-38.

59. Hemminki, A., et al., *Loss of the wild type MLH1 gene is a feature of hereditary nonpolyposis colorectal cancer.* Nat Genet, 1994. **8**(4): p. 405-10.

60. Nicolaides, N.C., et al., *Mutations of two PMS homologues in hereditary nonpolyposis colon cancer.* Nature, 1994. **371**(6492): p. 75-80.

61. Aarnio, M., et al., *Cancer risk in mutation carriers of DNA-mismatch-repair genes.* Int J Cancer, 1999. **81**(2): p. 214-8.

62. Kolodner, R.D., et al., *Germ-line msh6 mutations in colorectal cancer families.* Cancer Res, 1999. **59**(20): p. 5068-74.

63. Herman, J.G., et al., *Incidence and functional consequences of hMLH1 promoter hypermethylation in colorectal carcinoma.* Proc Natl Acad Sci U S A, 1998. **95**(12): p. 6870-5.

64. Veigl, M.L., et al., *Biallelic inactivation of hMLH1 by epigenetic gene silencing, a novel mechanism causing human MSI cancers.* Proc Natl Acad Sci U S A, 1998. **95**(15): p. 8698-702.

65. Markowitz, S., et al., *Inactivation of the type II TGF-beta receptor in colon cancer cells with microsatellite instability.* Science, 1995. **268**(5215): p. 1336-8.

66. Parsons, R., et al., *Microsatellite instability and mutations of the transforming growth factor beta type II receptor gene in colorectal cancer.* Cancer Res, 1995. **55**(23): p. 5548-50.

67. Nazemalhosseini Mojarad, E., et al., *The CpG island methylator phenotype (CIMP) in colorectal cancer.* Gastroenterol Hepatol Bed Bench, 2013. **6**(3): p. 120-8.

68. Rashid, A., et al., *CpG island methylation in colorectal adenomas.* Am J Pathol, 2001. **159**(3): p. 1129-35.

69. Petko, Z., et al., *Aberrantly methylated CDKN2A, MGMT, and MLH1 in colon polyps and in fecal DNA from patients with colorectal polyps.* Clin Cancer Res, 2005. **11**(3): p. 1203-9.

70. Lao, V.V. and W.M. Grady, *Epigenetics and colorectal cancer.* Nat Rev Gastroenterol Hepatol, 2011. **8**(12): p. 686-700.

71. Simons, C.C., et al., *A novel classification of colorectal tumors based on microsatellite instability, the CpG island methylator phenotype and chromosomal instability: implications for prognosis.* Ann Oncol, 2013. **24**(8): p. 2048-56.

72. Jasmine, F., et al., *Interaction between Microsatellite Instability (MSI) and Tumor DNA Methylation in the Pathogenesis of Colorectal Carcinoma.* Cancers (Basel), 2021. **13**(19).

73. Jung, B., J.J. Staudacher, and D. Beauchamp, *Transforming Growth Factor beta Superfamily Signaling in Development of Colorectal Cancer.* Gastroenterology, 2017. **152**(1): p. 36-52.

74. Itatani, Y., K. Kawada, and Y. Sakai, *Transforming Growth Factor-beta Signaling Pathway in Colorectal Cancer and Its Tumor Microenvironment.* Int J Mol Sci, 2019. **20**(23).

75. Wrana, J.L., et al., *Mechanism of activation of the TGF-beta receptor.* Nature, 1994. **370**(6488): p. 341-7.

76. Heldin, C.H., K. Miyazono, and P. ten Dijke, *TGF-beta signalling from cell membrane to nucleus through SMAD proteins.* Nature, 1997. **390**(6659): p. 465-71.

77. Ikushima, H. and K. Miyazono, *TGFbeta signalling: a complex web in cancer progression.* Nat Rev Cancer, 2010. **10**(6): p. 415-24.

78. Moustakas, A. and C.H. Heldin, *Non-Smad TGF-beta signals.* J Cell Sci, 2005. **118**(Pt 16): p. 3573-84.

79. Zhang, Y.E., *Non-Smad pathways in TGF-beta signaling.* Cell Res, 2009. **19**(1): p. 128-39.

80. Voorneveld, P.W., et al., *Loss of SMAD4 alters BMP signaling to promote colorectal cancer cell metastasis via activation of Rho and ROCK.* Gastroenterology, 2014. **147**(1): p. 196-208 e13.

81. Jang, C.W., et al., *TGF-beta induces apoptosis through Smad-mediated expression of DAP-kinase.* Nat Cell Biol, 2002. **4**(1): p. 51-8.

82. Takekawa, M., et al., *Smad-dependent GADD45beta expression mediates delayed activation of p38 MAP kinase by TGF-beta.* EMBO J, 2002. **21**(23): p. 6473-82.

83. Ohgushi, M., et al., *Transforming growth factor beta-dependent sequential activation of Smad, Bim, and caspase-9 mediates physiological apoptosis in gastric epithelial cells.* Mol Cell Biol, 2005. **25**(22): p. 10017-28.

84. Egle, A., et al., *Bim is a suppressor of Myc-induced mouse B cell leukemia.* Proc Natl Acad Sci U S A, 2004. **101**(16): p. 6164-9.

85. Chen, C.R., et al., *E2F4/5 and p107 as Smad cofactors linking the TGFbeta receptor to c-myc repression.* Cell, 2002. **110**(1): p. 19-32.

86. Gomis, R.R., et al., *C/EBPbeta at the core of the TGFbeta cytostatic response and its evasion in metastatic breast cancer cells.* Cancer Cell, 2006. **10**(3): p. 203-14.

87. Seoane, J., et al., *TGFbeta influences Myc, Miz-1 and Smad to control the CDK inhibitor p15INK4b.* Nat Cell Biol, 2001. **3**(4): p. 400-8.

88. Warner, B.J., et al., *Myc downregulation by transforming growth factor beta required for activation of the p15(Ink4b) G(1) arrest pathway.* Mol Cell Biol, 1999. **19**(9): p. 5913-22.

89. Seoane, J., et al., *Integration of Smad and forkhead pathways in the control of neuroepithelial and glioblastoma cell proliferation.* Cell, 2004. **117**(2): p. 211-23.

90. Tauriello, D.V.F., et al., *TGFbeta drives immune evasion in genetically reconstituted colon cancer metastasis.* Nature, 2018. **554**(7693): p. 538-543.

91. Means, A.L., et al., *Epithelial Smad4 Deletion Up-Regulates Inflammation and Promotes Inflammation-Associated Cancer.* Cell Mol Gastroenterol Hepatol, 2018. **6**(3): p. 257-276.

92. Kitamura, T., et al., *SMAD4-deficient intestinal tumors recruit CCR1+ myeloid cells that promote invasion.* Nat Genet, 2007. **39**(4): p. 467-75.

93. Kitamura, T., et al., *Inactivation of chemokine (C-C motif) receptor 1 (CCR1) suppresses colon cancer liver metastasis by blocking accumulation of immature myeloid cells in a mouse model.* Proc Natl Acad Sci U S A, 2010. **107**(29): p. 13063-8.

94. Munro, M.J., et al., *Cancer stem cells in colorectal cancer: a review.* J Clin Pathol, 2018. **71**(2): p. 110-116.

95. Batlle, E. and H. Clevers, *Cancer stem cells revisited.* Nat Med, 2017. **23**(10): p. 1124-1134.

96. Clayton, E., et al., *A single type of progenitor cell maintains normal epidermis.* Nature, 2007. **446**(7132): p. 185-9.

97. Barker, N., et al., *Identification of stem cells in small intestine and colon by marker gene Lgr5.* Nature, 2007. **449**(7165): p. 1003-7.

98. Barker, N., et al., *Lgr5(+ve) stem cells drive self-renewal in the stomach and build long-lived gastric units in vitro.* Cell Stem Cell, 2010. **6**(1): p. 25-36.

99. Sato, T., et al., *Paneth cells constitute the niche for Lgr5 stem cells in intestinal crypts.* Nature, 2011. **469**(7330): p. 415-8.

100. Schwitalla, S., et al., *Intestinal tumorigenesis initiated by dedifferentiation and acquisition of stem-cell-like properties.* Cell, 2013. **152**(1-2): p. 25-38.

101. Snippert, H.J., et al., *Intestinal crypt homeostasis results from neutral competition between symmetrically dividing Lgr5 stem cells.* Cell, 2010. **143**(1): p. 134-44.

102. Lopez-Garcia, C., et al., *Intestinal stem cell replacement follows a pattern of neutral drift.* Science, 2010. **330**(6005): p. 822-5.

103. Snippert, H.J., et al., *Biased competition between Lgr5 intestinal stem cells driven by oncogenic mutation induces clonal expansion.* EMBO Rep, 2014. **15**(1): p. 62-9.

104. Leushacke, M., et al., *Lgr5(+) gastric stem cells divide symmetrically to effect epithelial homeostasis in the pylorus.* Cell Rep, 2013. **5**(2): p. 349-56.

105. Doupe, D.P., et al., *The ordered architecture of murine ear epidermis is maintained by progenitor cells with random fate.* Dev Cell, 2010. **18**(2): p. 317-23.

106. Shimokawa, M., et al., *Visualization and targeting of LGR5(+) human colon cancer stem cells.* Nature, 2017. **545**(7653): p. 187-192.

107. Tetteh, P.W., et al., *Replacement of Lost Lgr5-Positive Stem Cells through Plasticity of Their Enterocyte-Lineage Daughters.* Cell Stem Cell, 2016. **18**(2): p. 203-13.

108. Tata, P.R., et al., *Dedifferentiation of committed epithelial cells into stem cells in vivo.* Nature, 2013. **503**(7475): p. 218-23.

109. Chen, B., et al., *Differential pre-malignant programs and microenvironment chart distinct paths to malignancy in human colorectal polyps.* Cell, 2021. **184**(26): p. 6262-6280 e26.

110. Shih, I.M., et al., *Top-down morphogenesis of colorectal tumors.* Proc Natl Acad Sci U S A, 2001. **98**(5): p. 2640-5.

111. Boesch, M., G. Spizzo, and A. Seeber, *Concise Review: Aggressive Colorectal Cancer: Role of Epithelial Cell Adhesion Molecule in Cancer Stem Cells and Epithelial-to-Mesenchymal Transition.* Stem Cells Transl Med, 2018. **7**(6): p. 495-501.

112. McDonald, T., et al., *Identification and cloning of an orphan G protein-coupled receptor of the glycoprotein hormone receptor subfamily.* Biochem Biophys Res Commun, 1998. **247**(2): p. 266-70.

113. Glinka, A., et al., *LGR4 and LGR5 are R-spondin receptors mediating Wnt/beta-catenin and Wnt/PCP signalling.* EMBO Rep, 2011. **12**(10): p. 1055-61.

114. Carmon, K.S., et al., *R-spondins function as ligands of the orphan receptors LGR4 and LGR5 to regulate Wnt/beta-catenin signaling.* Proc Natl Acad Sci U S A, 2011. **108**(28): p. 11452-7.

115. Kemper, K., et al., *Monoclonal antibodies against Lgr5 identify human colorectal cancer stem cells.* Stem Cells, 2012. **30**(11): p. 2378-86.

116. Yang, L., et al., *LGR5 Promotes Breast Cancer Progression and Maintains Stem-Like Cells Through Activation of Wnt/beta-Catenin Signaling.* Stem Cells, 2015. **33**(10): p. 2913-24.

117. de Sousa e Melo, F., et al., *A distinct role for Lgr5(+) stem cells in primary and metastatic colon cancer.* Nature, 2017. **543**(7647): p. 676-680.

118. Hirsch, D., et al., *LGR5 positivity defines stem-like cells in colorectal cancer.* Carcinogenesis, 2014. **35**(4): p. 849-58.

119. Sato, T., et al., *Single Lgr5 stem cells build crypt-villus structures in vitro without a mesenchymal niche.* Nature, 2009. **459**(7244): p. 262-5.

120. van de Wetering, M., et al., *The beta-catenin/TCF-4 complex imposes a crypt progenitor phenotype on colorectal cancer cells.* Cell, 2002. **111**(2): p. 241-50.

121. Cortina, C., et al., *A genome editing approach to study cancer stem cells in human tumors.* EMBO Mol Med, 2017. **9**(7): p. 869-879.

122. Dieter, S.M., H. Glimm, and C.R. Ball, *Colorectal cancer-initiating cells caught in the act.* EMBO Mol Med, 2017. **9**(7): p. 856-858.

123. Dame, M.K., et al., *Identification, isolation and characterization of human LGR5-positive colon adenoma cells.* Development, 2018. **145**(6).

124. Leng, Z., et al., *Lgr5+CD44+EpCAM+ Strictly Defines Cancer Stem Cells in Human Colorectal Cancer.* Cell Physiol Biochem, 2018. **46**(2): p. 860-872.

125. Litvinov, S.V., et al., *Ep-CAM: a human epithelial antigen is a homophilic cell-cell adhesion molecule.* J Cell Biol, 1994. **125**(2): p. 437-46.

126. Maetzel, D., et al., *Nuclear signalling by tumour-associated antigen EpCAM.* Nat Cell Biol, 2009. **11**(2): p. 162-71.

127. Nubel, T., et al., *Claudin-7 regulates EpCAM-mediated functions in tumor progression.* Mol Cancer Res, 2009. **7**(3): p. 285-99.

128. Wang, M.H., et al., *Epithelial cell adhesion molecule overexpression regulates epithelial-mesenchymal transition, stemness and metastasis of nasopharyngeal carcinoma cells via the PTEN/AKT/mTOR pathway.* Cell Death Dis, 2018. **9**(1): p. 2.

129. Hiraga, T., S. Ito, and H. Nakamura, *EpCAM expression in breast cancer cells is associated with enhanced bone metastasis formation.* Int J Cancer, 2016. **138**(7): p. 1698-708.

130. Seeber, A., et al., *Predominant expression of truncated EpCAM is associated with a more aggressive phenotype and predicts poor overall survival in colorectal cancer.* Int J Cancer, 2016. **139**(3): p. 657-63.

131. Pelletier, J., G. Thomas, and S. Volarevic, *Ribosome biogenesis in cancer: new players and therapeutic avenues.* Nat Rev Cancer, 2018. **18**(1): p. 51-63.

132. Pecoraro, A., et al., *Ribosome Biogenesis and Cancer: Overview on Ribosomal Proteins.* Int J Mol Sci, 2021. **22**(11).

133. Elhamamsy, A.R., et al., *Ribosome Biogenesis: A Central Player in Cancer Metastasis and Therapeutic Resistance.* Cancer Res, 2022. **82**(13): p. 2344-2353.

134. Holzel, M., et al., *Mammalian WDR12 is a novel member of the Pes1-Bop1 complex and is required for ribosome biogenesis and cell proliferation.* J Cell Biol, 2005. **170**(3): p. 367-78.

135. Rohrmoser, M., et al., *Interdependence of Pes1, Bop1, and WDR12 controls nucleolar localization and assembly of the PeBoW complex required for maturation of the 60S ribosomal subunit.* Mol Cell Biol, 2007. **27**(10): p. 3682-94.

136. Romes, E.M., M. Sobhany, and R.E. Stanley, *The Crystal Structure of the Ubiquitin-like Domain of Ribosome Assembly Factor Ytm1 and Characterization of Its Interaction with the AAA-ATPase Midasin.* J Biol Chem, 2016. **291**(2): p. 882-93.

137. Tang, L., et al., *Interactions among Ytm1, Erb1, and Nop7 required for assembly of the Nop7-subcomplex in yeast preribosomes.* Mol Biol Cell, 2008. **19**(7): p. 2844-56.

138. Bassler, J., et al., *The AAA-ATPase Rea1 drives removal of biogenesis factors during multiple stages of 60S ribosome assembly.* Mol Cell, 2010. **38**(5): p. 712-21.

139. Kressler, D., et al., *The power of AAA-ATPases on the road of pre-60S ribosome maturation--molecular machines that strip pre-ribosomal particles.* Biochim Biophys Acta, 2012. **1823**(1): p. 92-100.

140. Ulbrich, C., et al., *Mechanochemical removal of ribosome biogenesis factors from nascent 60S ribosomal subunits.* Cell, 2009. **138**(5): p. 911-22.

141. Chen, Z., et al., *Structural Insights into Mdn1, an Essential AAA Protein Required for Ribosome Biogenesis.* Cell, 2018. **175**(3): p. 822-834 e18.

142. Boon, K., et al., *N-myc enhances the expression of a large set of genes functioning in ribosome biogenesis and protein synthesis.* EMBO J, 2001. **20**(6): p. 1383-93.

143. Arabi, A., et al., *c-Myc associates with ribosomal DNA and activates RNA polymerase I transcription.* Nat Cell Biol, 2005. **7**(3): p. 303-10.

144. Grandori, C., et al., *c-Myc binds to human ribosomal DNA and stimulates transcription of rRNA genes by RNA polymerase I.* Nat Cell Biol, 2005. **7**(3): p. 311-8.

145. Felton-Edkins, Z.A., et al., *Direct regulation of RNA polymerase III transcription by RB, p53 and c-Myc.* Cell Cycle, 2003. **2**(3): p. 181-4.

146. Gomez-Roman, N., et al., *Direct activation of RNA polymerase III transcription by c-Myc.* Nature, 2003. **421**(6920): p. 290-4.

147. Stefanovsky, V.Y., et al., *An immediate response of ribosomal transcription to growth factor stimulation in mammals is mediated by ERK phosphorylation of UBF.* Mol Cell, 2001. **8**(5): p. 1063-73.

148. Zhao, J., et al., *ERK-dependent phosphorylation of the transcription initiation factor TIF-IA is required for RNA polymerase I transcription and cell growth.* Mol Cell, 2003. **11**(2): p. 405-13.

149. Zisi, A., J. Bartek, and M.S. Lindstrom, *Targeting Ribosome Biogenesis in Cancer: Lessons Learned and Way Forward.* Cancers (Basel), 2022. **14**(9).

150. Nigro, J.M., et al., *Mutations in the p53 gene occur in diverse human tumour types.* Nature, 1989. **342**(6250): p. 705-8.

151. Hollstein, M., et al., *p53 mutations in human cancers.* Science, 1991. **253**(5015): p. 49-53.

152. Cairns, C.A. and R.J. White, *p53 is a general repressor of RNA polymerase III transcription.* EMBO J, 1998. **17**(11): p. 3112-23.

153. Budde, A. and I. Grummt, *p53 represses ribosomal gene transcription.* Oncogene, 1999. **18**(4): p. 1119-24.

154. Zhai, W. and L. Comai, *Repression of RNA polymerase I transcription by the tumor suppressor p53.* Mol Cell Biol, 2000. **20**(16): p. 5930-8.

155. Cavanaugh, A.H., et al., *Activity of RNA polymerase I transcription factor UBF blocked by Rb gene product.* Nature, 1995. **374**(6518): p. 177-80.

156. Ayrault, O., et al., *Human Arf tumor suppressor specifically interacts with chromatin containing the promoter of rRNA genes.* Oncogene, 2004. **23**(49): p. 8097-104.

157. Zhang, C., L. Comai, and D.L. Johnson, *PTEN represses RNA Polymerase I transcription by disrupting the SL1 complex.* Mol Cell Biol, 2005. **25**(16): p. 6899-911.

158. Metge, B.J., et al., *Hypoxia re-programs 2'-O-Me modifications on ribosomal RNA.* iScience, 2021. **24**(1): p. 102010.

159. Maden, B.E., *Identification of the locations of the methyl groups in 18 S ribosomal RNA from Xenopus laevis and man.* J Mol Biol, 1986. **189**(4): p. 681-99.

160. Maden, B.E., *Locations of methyl groups in 28 S rRNA of Xenopus laevis and man. Clustering in the conserved core of molecule.* J Mol Biol, 1988. **201**(2): p. 289-314.

161. Maden, E.H. and J.A. Wakeman, *Pseudouridine distribution in mammalian 18 S ribosomal RNA. A major cluster in the central region of the molecule.* Biochem J, 1988. **249**(2): p. 459-64.

162. Kiss-Laszlo, Z., et al., *Site-specific ribose methylation of preribosomal RNA: a novel function for small nucleolar RNAs.* Cell, 1996. **85**(7): p. 1077-88.

163. Ganot, P., M.L. Bortolin, and T. Kiss, *Site-specific pseudouridine formation in preribosomal RNA is guided by small nucleolar RNAs.* Cell, 1997. **89**(5): p. 799-809.

164. Marcel, V., et al., *Ribosomal RNA 2'O-methylation as a novel layer of inter-tumour heterogeneity in breast cancer.* NAR Cancer, 2020. **2**(4): p. zcaa036.

165. Marcel, V., et al., *p53 acts as a safeguard of translational control by regulating fibrillarin and rRNA methylation in cancer.* Cancer Cell, 2013. **24**(3): p. 318-30.

166. Bretones, G., et al., *Altered patterns of global protein synthesis and translational fidelity in RPS15-mutated chronic lymphocytic leukemia.* Blood, 2018. **132**(22): p. 2375-2388.

167. Burtin, F., C.S. Mullins, and M. Linnebacher, *Mouse models of colorectal cancer: Past, present and future perspectives.* World J Gastroenterol, 2020. **26**(13): p. 1394-1426.

168. Nascimento-Goncalves, E., et al., *Animal Models of Colorectal Cancer: From Spontaneous to Genetically Engineered Models and Their Applications.* Vet Sci, 2021. **8**(4).

169. Johnson, R.L. and J.C. Fleet, *Animal models of colorectal cancer.* Cancer Metastasis Rev, 2013. **32**(1-2): p. 39-61.

170. Mittal, V.K., J.S. Bhullar, and K. Jayant, *Animal models of human colorectal cancer: Current status, uses and limitations.* World J Gastroenterol, 2015. **21**(41): p. 11854-61.

171. Kwong, L.N. and W.F. Dove, *APC and its modifiers in colon cancer.* Adv Exp Med Biol, 2009. **656**: p. 85-106.

172. Treuting, P.M., S. Dintzis, and K.S. Montine, *Comparative Anatomy and Histology: A Mouse, Rat, and Human Atlas*. 2017: Elsevier Science.

173. Holyoak, D.T., et al., *Osteoarthritis: Pathology, Mouse Models, and Nanoparticle Injectable Systems for Targeted Treatment.* Ann Biomed Eng, 2016. **44**(6): p. 2062-75.

174. Vdoviakova, K., et al., *Surgical Anatomy of the Gastrointestinal Tract and Its Vasculature in the Laboratory Rat.* Gastroenterol Res Pract, 2016. **2016**: p. 2632368.

175. Kobaek-Larsen, M., et al., *Review of colorectal cancer and its metastases in rodent models: comparative aspects with those in humans.* Comp Med, 2000. **50**(1): p. 16-26.

176. Miyamoto, M. and Y. Tani, *A study on colon cancer-prone rats of WF-Osaka strain.* Med J Osaka Univ, 1989. **38**(1-4): p. 1-12.

177. Newmark, H.L., et al., *Western-style diet-induced colonic tumors and their modulation by calcium and vitamin D in C57Bl/6 mice: a preclinical model for human sporadic colon cancer.* Carcinogenesis, 2009. **30**(1): p. 88-92.

178. Burdette, W.J., *Carcinoma of the Colon and Antecedent Epithelium*. 1970: Thomas.

179. Reddy, B.S., et al., *Colon carcinogenesis with azoxymethane and dimethylhydrazine in germ-free rats.* Cancer Res, 1975. **35**(2): p. 287-90.

180. Sohn, O.S., et al., *Enhancement of rat liver microsomal metabolism of azoxymethane to methylazoxymethanol by chronic ethanol administration: similarity to the microsomal metabolism of N-nitrosodimethylamine.* Cancer Res, 1987. **47**(12): p. 3123-9.

181. Derry, M.M., et al., *Characterization of azoxymethane-induced colon tumor metastasis to lung in a mouse model relevant to human sporadic colorectal cancer and evaluation of grape seed extract efficacy.* Exp Toxicol Pathol, 2014. **66**(5-6): p. 235-42.

182. Tanaka, T., et al., *A novel inflammation-related mouse colon carcinogenesis model induced by azoxymethane and dextran sodium sulfate.* Cancer Sci, 2003. **94**(11): p. 965-73.

183. De Robertis, M., et al., *The AOM/DSS murine model for the study of colon carcinogenesis: From pathways to diagnosis and therapy studies.* J Carcinog, 2011. **10**: p. 9.

184. Narisawa, T., et al., *Carcinoma of the colon and rectum of rats by rectal infusion of N-methyl-N'-nitro-N-nitrosoguanidine.* Gan, 1971. **62**(3): p. 231-4.

185. Narisawa, T. and J.H. Weisburger, *Colon cancer induction in mice by intrarectal instillation of N-methylnitosorurea (38498).* Proc Soc Exp Biol Med, 1975. **148**(1): p. 166-9.

186. Wyatt, M.D. and D.L. Pittman, *Methylating agents and DNA repair responses: Methylated bases and sources of strand breaks.* Chem Res Toxicol, 2006. **19**(12): p. 1580-94.

187. Moser, A.R., H.C. Pitot, and W.F. Dove, *A dominant mutation that predisposes to multiple intestinal neoplasia in the mouse.* Science, 1990. **247**(4940): p. 322-4.

188. Groden, J., et al., *Identification and characterization of the familial adenomatous polyposis coli gene.* Cell, 1991. **66**(3): p. 589-600.

189. Bisgaard, M.L., et al., *Familial adenomatous polyposis (FAP): frequency, penetrance, and mutation rate.* Hum Mutat, 1994. **3**(2): p. 121-5.

190. Yamada, Y. and H. Mori, *Multistep carcinogenesis of the colon in Apc(Min/+) mouse.* Cancer Sci, 2007. **98**(1): p. 6-10.

191. Sauer, B. and N. Henderson, *Site-specific DNA recombination in mammalian cells by the Cre recombinase of bacteriophage P1.* Proc Natl Acad Sci U S A, 1988. **85**(14): p. 5166-70.

192. Lakso, M., et al., *Targeted oncogene activation by site-specific recombination in transgenic mice.* Proc Natl Acad Sci U S A, 1992. **89**(14): p. 6232-6.

193. Sansom, O.J., et al., *Loss of Apc allows phenotypic manifestation of the transforming properties of an endogenous K-ras oncogene in vivo.* Proc Natl Acad Sci U S A, 2006. **103**(38): p. 14122-7.

194. Sakai, E., et al., *Combined Mutation of Apc, Kras, and Tgfbr2 Effectively Drives Metastasis of Intestinal Cancer.* Cancer Res, 2018. **78**(5): p. 1334-1346.

195. Takaku, K., et al., *Intestinal tumorigenesis in compound mutant mice of both Dpc4 (Smad4) and Apc genes.* Cell, 1998. **92**(5): p. 645-56.

196. Alberici, P., et al., *Smad4 haploinsufficiency in mouse models for intestinal cancer.* Oncogene, 2006. **25**(13): p. 1841-51.

197. Nakayama, M., et al., *Intestinal cancer progression by mutant p53 through the acquisition of invasiveness associated with complex glandular formation.* Oncogene, 2017. **36**(42): p. 5885-5896.

198. Rygaard, J. and C.O. Povlsen, *Heterotransplantation of a human malignant tumour to "Nude" mice.* Acta Pathol Microbiol Scand, 1969. **77**(4): p. 758-60.

199. Kyriazis, A.P., et al., *Growth patterns and metastatic behavior of human tumors growing in athymic mice.* Cancer Res, 1978. **38**(10): p. 3186-90.

200. Boven, E., et al., *Phase II preclinical drug screening in human tumor xenografts: a first European multicenter collaborative study.* Cancer Res, 1992. **52**(21): p. 5940-7.

201. Langdon, S.P., et al., *Preclinical phase II studies in human tumor xenografts: a European multicenter follow-up study.* Ann Oncol, 1994. **5**(5): p. 415-22.

202. Yang, Y.S., et al., *Recent advances in the development of transplanted colorectal cancer mouse models.* Transl Res, 2022. **249**: p. 128-143.

203. Tanaka, Y., et al., *Inhibition of HT-29 human colon cancer growth under the renal capsule of severe combined immunodeficient mice by an analogue of 1,25-dihydroxyvitamin D3, DD-003.* Cancer Res, 1994. **54**(19): p. 5148-53.

204. Lawrentschuk, N., et al., *Xenografting tumour beneath the renal capsule using modern surgical equipment.* Eur Surg Res, 2006. **38**(3): p. 340-6.

205. Katsiampoura, A., et al., *Modeling of Patient-Derived Xenografts in Colorectal Cancer.* Mol Cancer Ther, 2017. **16**(7): p. 1435-1442.

206. Mullins, C.S., et al., *Integrated Biobanking and Tumor Model Establishment of Human Colorectal Carcinoma Provides Excellent Tools for Preclinical Research.* Cancers (Basel), 2019. **11**(10).

207. Guenot, D., et al., *Primary tumour genetic alterations and intra-tumoral heterogeneity are maintained in xenografts of human colon cancers showing chromosome instability.* J Pathol, 2006. **208**(5): p. 643-52.

208. Prall, F., et al., *Colorectal carcinoma tumour budding and podia formation in the xenograft microenvironment.* PLoS One, 2017. **12**(10): p. e0186271.

209. Burgenske, D.M., et al., *Establishment of genetically diverse patient-derived xenografts of colorectal cancer.* Am J Cancer Res, 2014. **4**(6): p. 824-37.

210. Blomme, A., et al., *Murine stroma adopts a human-like metabolic phenotype in the PDX model of colorectal cancer and liver metastases.* Oncogene, 2018. **37**(9): p. 1237-1250.

211. Hylander, B.L., et al., *Origin of the vasculature supporting growth of primary patient tumor xenografts.* J Transl Med, 2013. **11**: p. 110.

212. Bertotti, A., et al., *A molecularly annotated platform of patient-derived xenografts ("xenopatients") identifies HER2 as an effective therapeutic target in cetuximab-resistant colorectal cancer.* Cancer Discov, 2011. **1**(6): p. 508-23.

213. Lazzari, L., et al., *Patient-Derived Xenografts and Matched Cell Lines Identify Pharmacogenomic Vulnerabilities in Colorectal Cancer.* Clin Cancer Res, 2019. **25**(20): p. 6243-6259.

214. Dangles-Marie, V., et al., *Establishment of human colon cancer cell lines from fresh tumors versus xenografts: comparison of success rate and cell line features.* Cancer Res, 2007. **67**(1): p. 398-407.

215. Prasetyanti, P.R., et al., *Capturing colorectal cancer inter-tumor heterogeneity in patient-derived xenograft (PDX) models.* Int J Cancer, 2019. **144**(2): p. 366-371.

216. Wetterauer, C., et al., *Early development of human lymphomas in a prostate cancer xenograft program using triple knock-out immunocompromised mice.* Prostate, 2015. **75**(6): p. 585-92.

217. Bresalier, R.S., et al., *A new animal model for human colon cancer metastasis.* Int J Cancer, 1987. **39**(5): p. 625-30.

218. Fu, X.Y., et al., *Models of human metastatic colon cancer in nude mice orthotopically constructed by using histologically intact patient specimens.* Proc Natl Acad Sci U S A, 1991. **88**(20): p. 9345-9.

219. Cañellas-Socias, A., et al., *Metastatic recurrence in colorectal cancer arises from residual EMP1+ cells.* Nature, 2022.

220. Cespedes, M.V., et al., *Orthotopic microinjection of human colon cancer cells in nude mice induces tumor foci in all clinically relevant metastatic sites.* Am J Pathol, 2007. **170**(3): p. 1077-85.

221. Oliveira, R.C., et al., *The role of mouse models in colorectal cancer research-The need and the importance of the orthotopic models.* Animal Model Exp Med, 2020. **3**(1): p. 1-8.

222. Zigmond, E., et al., *Utilization of murine colonoscopy for orthotopic implantation of colorectal cancer.* PLoS One, 2011. **6**(12): p. e28858.

223. Roper, J., et al., *In vivo genome editing and organoid transplantation models of colorectal cancer and metastasis.* Nat Biotechnol, 2017. **35**(6): p. 569-576.

224. Roper, J., et al., *Colonoscopy-based colorectal cancer modeling in mice with CRISPR-Cas9 genome editing and organoid transplantation.* Nat Protoc, 2018. **13**(2): p. 217-234.

225. Bettenworth, D., et al., *Endoscopy-guided orthotopic implantation of colorectal cancer cells results in metastatic colorectal cancer in mice.* Clin Exp Metastasis, 2016. **33**(6): p. 551-62.

226. Drost, J., et al., *Sequential cancer mutations in cultured human intestinal stem cells.* Nature, 2015. **521**(7550): p. 43-7.

227. Ran, F.A., et al., *Genome engineering using the CRISPR-Cas9 system.* Nat Protoc, 2013. **8**(11): p. 2281-2308.

228. Dietinger, V., et al., *Wnt-driven LARGE2 mediates laminin-adhesive O-glycosylation in human colonic epithelial cells and colorectal cancer.* Cell Commun Signal, 2020. **18**(1): p. 102.

229. Tovar, C., et al., *Small-molecule MDM2 antagonists reveal aberrant p53 signaling in cancer: implications for therapy.* Proc Natl Acad Sci U S A, 2006. **103**(6): p. 1888-93.

230. Heinz, S., et al., *Simple combinations of lineage-determining transcription factors prime cis-regulatory elements required for macrophage and B cell identities.* Mol Cell, 2010. **38**(4): p. 576-89.

231. Kim, D., et al., *TopHat2: accurate alignment of transcriptomes in the presence of insertions, deletions and gene fusions.* Genome Biol, 2013. **14**(4): p. R36.

232. Anders, S., P.T. Pyl, and W. Huber, *HTSeq--a Python framework to work with high-throughput sequencing data.* Bioinformatics, 2015. **31**(2): p. 166-9.

233. Love, M.I., W. Huber, and S. Anders, *Moderated estimation of fold change and dispersion for RNA-seq data with DESeq2.* Genome Biol, 2014. **15**(12): p. 550.

234. Grossman, R.L., et al., *Toward a Shared Vision for Cancer Genomic Data.* N Engl J Med, 2016. **375**(12): p. 1109-12.

235. Isella, C., et al., *Selective analysis of cancer-cell intrinsic transcriptional traits defines novel clinically relevant subtypes of colorectal cancer.* Nat Commun, 2017. **8**: p. 15107.

236. Guinney, J., et al., *The consensus molecular subtypes of colorectal cancer.* Nat Med, 2015. **21**(11): p. 1350-6.

237. Liberzon, A., et al., *The Molecular Signatures Database (MSigDB) hallmark gene set collection.* Cell Syst, 2015. **1**(6): p. 417-425.

238. Subramanian, A., et al., *Gene set enrichment analysis: a knowledge-based approach for interpreting genome-wide expression profiles.* Proc Natl Acad Sci U S A, 2005. **102**(43): p. 15545-50.

239. Loevenich, L.P., et al., *SMAD4 Loss Induces c-MYC-Mediated NLE1 Upregulation to Support Protein Biosynthesis, Colorectal Cancer Growth, and Metastasis.* Cancer Res, 2022. **82**(24): p. 4604-4623.

240. Jung, P., et al., *Isolation and in vitro expansion of human colonic stem cells.* Nat Med, 2011. **17**(10): p. 1225-7.

241. Brunschwig, E.B., et al., *PMEPA1, a transforming growth factor-beta-induced marker of terminal colonocyte differentiation whose expression is maintained in primary and metastatic colon cancer.* Cancer Res, 2003. **63**(7): p. 1568-75.

242. Wasserman, I., et al., *SMAD4 Loss in Colorectal Cancer Patients Correlates with Recurrence, Loss of Immune Infiltrate, and Chemoresistance.* Clin Cancer Res, 2019. **25**(6): p. 1948-1956.

243. Behan, F.M., et al., *Prioritization of cancer therapeutic targets using CRISPR-Cas9 screens.* Nature, 2019. **568**(7753): p. 511-516.

244. Tsherniak, A., et al., *Defining a Cancer Dependency Map.* Cell, 2017. **170**(3): p. 564-576 e16.

245. Jung, P. and H. Hermeking, *The c-MYC-AP4-p21 cascade.* Cell Cycle, 2009. **8**(7): p. 982-9.

246. Smit, W.L., et al., *Driver mutations of the adenoma-carcinoma sequence govern the intestinal epithelial global translational capacity.* Proc Natl Acad Sci U S A, 2020. **117**(41): p. 25560-25570.

247. Alawi, F. and M.N. Lee, *DKC1 is a direct and conserved transcriptional target of c-MYC.* Biochem Biophys Res Commun, 2007. **362**(4): p. 893-8.

248. Nachmani, D., et al., *Germline NPM1 mutations lead to altered rRNA 2'-O-methylation and cause dyskeratosis congenita.* Nat Genet, 2019. **51**(10): p. 1518-1529.

249. Schwartz, S., et al., *Transcriptome-wide mapping reveals widespread dynamic-regulated pseudouridylation of ncRNA and mRNA.* Cell, 2014. **159**(1): p. 148-162.

250. Zeller, K.I., et al., *An integrated database of genes responsive to the Myc oncogenic transcription factor: identification of direct genomic targets.* Genome Biol, 2003. **4**(10): p. R69.

251. Consortium, E.P., *An integrated encyclopedia of DNA elements in the human genome.* Nature, 2012. **489**(7414): p. 57-74.

252. Liu, J., et al., *Imaging protein synthesis in cells and tissues with an alkyne analog of puromycin.* Proc Natl Acad Sci U S A, 2012. **109**(2): p. 413-8.

253. Borowicz, S., et al., *The soft agar colony formation assay.* J Vis Exp, 2014(92): p. e51998.

254. Sui, X., et al., *p38 and JNK MAPK pathways control the balance of apoptosis and autophagy in response to chemotherapeutic agents.* Cancer Lett, 2014. **344**(2): p. 174-9.

255. Vind, A.C., A.V. Genzor, and S. Bekker-Jensen, *Ribosomal stress-surveillance: three pathways is a magic number.* Nucleic Acids Res, 2020. **48**(19): p. 10648-10661.

256. Lawrence, B.P. and W.J. Brown, *Inhibition of protein synthesis separates autophagic sequestration from the delivery of lysosomal enzymes.* J Cell Sci, 1993. **105 (Pt 2)**: p. 473-80.

257. Runwal, G., et al., *LC3-positive structures are prominent in autophagy-deficient cells.* Sci Rep, 2019. **9**(1): p. 10147.

258. Mauthe, M., et al., *Chloroquine inhibits autophagic flux by decreasing autophagosome-lysosome fusion.* Autophagy, 2018. **14**(8): p. 1435-1455.

259. Kongara, S. and V. Karantza, *The interplay between autophagy and ROS in tumorigenesis.* Front Oncol, 2012. **2**: p. 171.

260. Mathew, R., et al., *Autophagy suppresses tumorigenesis through elimination of p62.* Cell, 2009. **137**(6): p. 1062-75.

261. Hardman, R.A., C.A. Afshari, and J.C. Barrett, *Involvement of mammalian MLH1 in the apoptotic response to peroxide-induced oxidative stress.* Cancer Res, 2001. **61**(4): p. 1392-7.

262. Nieminen, A.L., et al., *Mitochondrial permeability transition in hepatocytes induced by t-BuOOH: NAD(P)H and reactive oxygen species.* Am J Physiol, 1997. **272**(4 Pt 1): p. C1286-94.

263. Shultz, L.D., et al., *Human lymphoid and myeloid cell development in NOD/LtSz-scid IL2R gamma null mice engrafted with mobilized human hemopoietic stem cells.* J Immunol, 2005. **174**(10): p. 6477-89.

264. Shultz, L.D., F. Ishikawa, and D.L. Greiner, *Humanized mice in translational biomedical research.* Nat Rev Immunol, 2007. **7**(2): p. 118-30.

265. Scholzen, T. and J. Gerdes, *The Ki-67 protein: from the known and the unknown.* J Cell Physiol, 2000. **182**(3): p. 311-22.

266. Sonnenblick, A., et al., *Final 10-year results of the Breast International Group 2-98 phase III trial and the role of Ki67 in predicting benefit of adjuvant docetaxel in patients with oestrogen receptor positive breast cancer.* Eur J Cancer, 2015. **51**(12): p. 1481-9.

267. Crowley, L.C. and N.J. Waterhouse, *Detecting Cleaved Caspase-3 in Apoptotic Cells by Flow Cytometry.* Cold Spring Harb Protoc, 2016. **2016**(11).

268. Liu, Y., et al., *Comparative Molecular Analysis of Gastrointestinal Adenocarcinomas.* Cancer Cell, 2018. **33**(4): p. 721-735 e8.

269. Deisenroth, C. and Y. Zhang, *Ribosome biogenesis surveillance: probing the ribosomal protein-Mdm2-p53 pathway.* Oncogene, 2010. **29**(30): p. 4253-60.

270. Donehower, L.A., et al., *Integrated Analysis of TP53 Gene and Pathway Alterations in The Cancer Genome Atlas.* Cell Rep, 2019. **28**(11): p. 3010.

271. Nakayama, M., et al., *Loss of wild-type p53 promotes mutant p53-driven metastasis through acquisition of survival and tumor-initiating properties.* Nat Commun, 2020. **11**(1): p. 2333.

272. Park, J.W., et al., *Smad4 and p53 synergize in suppressing autochthonous intestinal cancer.* Cancer Med, 2022. **11**(9): p. 1925-1936.

273. Danielpour, D., et al., *Sandwich enzyme-linked immunosorbent assays (SELISAs) quantitate and distinguish two forms of transforming growth factor-beta (TGF-beta 1 and TGF-beta 2) in complex biological fluids.* Growth Factors, 1989. **2**(1): p. 61-71.

274. Oida, T. and H.L. Weiner, *Depletion of TGF-beta from fetal bovine serum.* J Immunol Methods, 2010. **362**(1-2): p. 195-8.

275. Sato, T., et al., *Long-term expansion of epithelial organoids from human colon, adenoma, adenocarcinoma, and Barrett's epithelium.* Gastroenterology, 2011. **141**(5): p. 1762-72.

276. Park, K., et al., *Genetic changes in the transforming growth factor beta (TGF-beta) type II receptor gene in human gastric cancer cells: correlation with sensitivity to growth inhibition by TGF-beta.* Proc Natl Acad Sci U S A, 1994. **91**(19): p. 8772-6.

277. Zhou, S., et al., *Targeted deletion of Smad4 shows it is required for transforming growth factor beta and activin signaling in colorectal cancer cells.* Proc Natl Acad Sci U S A, 1998. **95**(5): p. 2412-6.

278. Dai, J.L., R.K. Bansal, and S.E. Kern, *G1 cell cycle arrest and apoptosis induction by nuclear Smad4/Dpc4: phenotypes reversed by a tumorigenic mutation.* Proc Natl Acad Sci U S A, 1999. **96**(4): p. 1427-32.

279. Liao, Y., M. Zhang, and B. Lonnerdal, *Growth factor TGF-beta induces intestinal epithelial cell (IEC-6) differentiation: miR-146b as a regulatory component in the negative feedback loop.* Genes Nutr, 2013. **8**(1): p. 69-78.

280. Li, D., et al., *KLF4-mediated negative regulation of IFITM3 expression plays a critical role in colon cancer pathogenesis.* Clin Cancer Res, 2011. **17**(11): p. 3558-68.

281. Satoh, K., et al., *Global metabolic reprogramming of colorectal cancer occurs at adenoma stage and is induced by MYC.* Proc Natl Acad Sci U S A, 2017. **114**(37): p. E7697-E7706.

282. Hu, H., L. Ye, and Z. Liu, *GINS2 regulates the proliferation and apoptosis of colon cancer cells through PTP4A1.* Mol Med Rep, 2022. **25**(4).

283. Liu, X., et al., *IFITM3 promotes bone metastasis of prostate cancer cells by mediating activation of the TGF-beta signaling pathway.* Cell Death Dis, 2019. **10**(7): p. 517.

284. Ye, Y., et al., *GINS2 promotes cell proliferation and inhibits cell apoptosis in thyroid cancer by regulating CITED2 and LOXL2.* Cancer Gene Ther, 2019. **26**(3-4): p. 103-113.

285. Wang, S., et al., *ZNF545 loss promotes ribosome biogenesis and protein translation to initiate colorectal tumorigenesis in mice.* Oncogene, 2021. **40**(48): p. 6590-6600.

286. Morral, C., et al., *Zonation of Ribosomal DNA Transcription Defines a Stem Cell Hierarchy in Colorectal Cancer.* Cell Stem Cell, 2020. **26**(6): p. 845-861 e12.

287. Ruggero, D., et al., *Dyskeratosis congenita and cancer in mice deficient in ribosomal RNA modification.* Science, 2003. **299**(5604): p. 259-62.

288. Teng, T., et al., *Loss of tumor suppressor RPL5/RPL11 does not induce cell cycle arrest but impedes proliferation due to reduced ribosome content and translation capacity.* Mol Cell Biol, 2013. **33**(23): p. 4660-71.

289. Dong, Z., et al., *Ribosomal Protein L15 is involved in Colon Carcinogenesis.* Int J Med Sci, 2019. **16**(8): p. 1132-1141.

290. Labriet, A., et al., *Germline variability and tumor expression level of ribosomal protein gene RPL28 are associated with survival of metastatic colorectal cancer patients.* Sci Rep, 2019. **9**(1): p. 13008.

291. Zhao, W., et al., *Ribosome Proteins Represented by RPL27A Mark the Development and Metastasis of Triple-Negative Breast Cancer in Mouse and Human.* Front Cell Dev Biol, 2021. **9**: p. 716730.

292. Luo, S., et al., *Highly expressed ribosomal protein L34 indicates poor prognosis in osteosarcoma and its knockdown suppresses osteosarcoma proliferation probably through translational control.* Sci Rep, 2016. **6**: p. 37690.

293. Otto, C., et al., *RNA polymerase I inhibition induces terminal differentiation, growth arrest, and vulnerability to senolytics in colorectal cancer cells.* Mol Oncol, 2022. **16**(15): p. 2788-2809.

294. Shi, R. and Z. Liu, *RPL15 promotes hepatocellular carcinoma progression via regulation of RPs-MDM2-p53 signaling pathway.* Cancer Cell Int, 2022. **22**(1): p. 150.

295. Ebright, R.Y., et al., *Deregulation of ribosomal protein expression and translation promotes breast cancer metastasis.* Science, 2020. **367**(6485): p. 1468-1473.

296. Kim, H.D., T.S. Kim, and J. Kim, *Aberrant ribosome biogenesis activates c-Myc and ASK1 pathways resulting in p53-dependent G1 arrest.* Oncogene, 2011. **30**(30): p. 3317-27.

297. Iordanov, M.S., et al., *Ribotoxic stress response: activation of the stress-activated protein kinase JNK1 by inhibitors of the peptidyl transferase reaction and by sequence-specific RNA damage to the alpha-sarcin/ricin loop in the 28S rRNA.* Mol Cell Biol, 1997. **17**(6): p. 3373-81.

298. Sauter, K.A., et al., *ZAK is required for doxorubicin, a novel ribotoxic stressor, to induce SAPK activation and apoptosis in HaCaT cells.* Cancer Biol Ther, 2010. **10**(3): p. 258-66.

299. Wong, J., et al., *Small molecule kinase inhibitors block the ZAK-dependent inflammatory effects of doxorubicin.* Cancer Biol Ther, 2013. **14**(1): p. 56-63.

300. Vind, A.C., et al., *ZAKalpha Recognizes Stalled Ribosomes through Partially Redundant Sensor Domains.* Mol Cell, 2020. **78**(4): p. 700-713 e7.

301. Pecoraro, A., et al., *Role of uL3 in the Crosstalk between Nucleolar Stress and Autophagy in Colon Cancer Cells.* Int J Mol Sci, 2020. **21**(6).

302. Artero-Castro, A., et al., *Disruption of the ribosomal P complex leads to stress-induced autophagy.* Autophagy, 2015. **11**(9): p. 1499-519.

303. Heijnen, H.F., et al., *Ribosomal protein mutations induce autophagy through S6 kinase inhibition of the insulin pathway.* PLoS Genet, 2014. **10**(5): p. e1004371.

304. Wang, H., et al., *Overexpression of ribosomal protein L15 is associated with cell proliferation in gastric cancer.* BMC Cancer, 2006. **6**: p. 91.

305. Bee, A., et al., *siRNA knockdown of ribosomal protein gene RPL19 abrogates the aggressive phenotype of human prostate cancer.* PLoS One, 2011. **6**(7): p. e22672.

306. Prakash, V., et al., *Ribosome biogenesis during cell cycle arrest fuels EMT in development and disease.* Nat Commun, 2019. **10**(1): p. 2110.

307. Rashid, O.M., et al., *Is tail vein injection a relevant breast cancer lung metastasis model?* J Thorac Dis, 2013. **5**(4): p. 385-92.

308. Yang, M., et al., *Ribosomal Protein L23 Drives the Metastasis of Hepatocellular Carcinoma via Upregulating MMP9.* Front Oncol, 2021. **11**: p. 779748.

309. Barillari, G., *The Impact of Matrix Metalloproteinase-9 on the Sequential Steps of the Metastatic Process.* Int J Mol Sci, 2020. **21**(12).

310. Sahai, E., *Illuminating the metastatic process.* Nat Rev Cancer, 2007. **7**(10): p. 737-49.

311. Liu, C., et al., *RPS15A promotes gastric cancer progression via activation of the Akt/IKK-beta/NF-kappaB signalling pathway.* J Cell Mol Med, 2019. **23**(3): p. 2207-2218.

312. Azijli, K., et al., *Non-canonical kinase signaling by the death ligand TRAIL in cancer cells: discord in the death receptor family.* Cell Death Differ, 2013. **20**(7): p. 858-68.

313. Gilmore, T.D., *Introduction to NF-kappaB: players, pathways, perspectives.* Oncogene, 2006. **25**(51): p. 6680-4.

314. Zhou, C., et al., *High RPS11 level in hepatocellular carcinoma associates with poor prognosis after curative resection.* Ann Transl Med, 2020. **8**(7): p. 466.

315. Toon, C.W., et al., *Immunohistochemistry for myc predicts survival in colorectal cancer.* PLoS One, 2014. **9**(2): p. e87456.

316. Lee, K.S., et al., *Favorable prognosis in colorectal cancer patients with co-expression of c-MYC and ss-catenin.* BMC Cancer, 2016. **16**(1): p. 730.

317. Arango, D., et al., *c-Myc overexpression sensitises colon cancer cells to camptothecin-induced apoptosis.* Br J Cancer, 2003. **89**(9): p. 1757-65.

318. Holch, J., S. Stintzing, and V. Heinemann, *Treatment of Metastatic Colorectal Cancer: Standard of Care and Future Perspectives.* Visc Med, 2016. **32**(3): p. 178-83.

319. Bee, A., et al., *Ribosomal protein l19 is a prognostic marker for human prostate cancer.* Clin Cancer Res, 2006. **12**(7 Pt 1): p. 2061-5.

320. Rao, B., et al., *RPL19 Is a Prognostic Biomarker and Promotes Tumor Progression in Hepatocellular Carcinoma.* Front Cell Dev Biol, 2021. **9**: p. 686547.

321. Takimoto, C.H., et al., *Correlation between ribosomal RNA production and RNA-directed fluoropyrimidine cytotoxicity.* Biochem Pharmacol, 1987. **36**(19): p. 3243-8.

322. Bruno, P.M., et al., *A subset of platinum-containing chemotherapeutic agents kills cells by inducing ribosome biogenesis stress.* Nat Med, 2017. **23**(4): p. 461-471.

323. Linnekamp, J.F., et al., *Consensus molecular subtypes of colorectal cancer are recapitulated in in vitro and in vivo models.* Cell Death Differ, 2018. **25**(3): p. 616-633.

324. Del Rio, M., et al., *Molecular subtypes of metastatic colorectal cancer are associated with patient response to irinotecan-based therapies.* Eur J Cancer, 2017. **76**: p. 68-75.

325. Deisenroth, C., D.A. Franklin, and Y. Zhang, *The Evolution of the Ribosomal Protein-MDM2-p53 Pathway.* Cold Spring Harb Perspect Med, 2016. **6**(12).

326. Castle, C.D., et al., *Las1L is a nucleolar protein required for cell proliferation and ribosome biogenesis.* Mol Cell Biol, 2010. **30**(18): p. 4404-14.

327. Liao, H., et al., *p53 induces a survival transcriptional response after nucleolar stress.* Mol Biol Cell, 2021. **32**(20): p. ar3.

328. Sun, X.X., et al., *Perturbation of 60 S ribosomal biogenesis results in ribosomal protein L5- and L11-dependent p53 activation.* J Biol Chem, 2010. **285**(33): p. 25812-21.

329. Castle, C.D., E.K. Cassimere, and C. Denicourt, *LAS1L interacts with the mammalian Rix1 complex to regulate ribosome biogenesis.* Mol Biol Cell, 2012. **23**(4): p. 716-28.

330. Tollervey, D., et al., *Temperature-sensitive mutations demonstrate roles for yeast fibrillarin in pre-rRNA processing, pre-rRNA methylation, and ribosome assembly.* Cell, 1993. **72**(3): p. 443-57.

331. Newton, K., et al., *Fibrillarin is essential for early development and required for accumulation of an intron-encoded small nucleolar RNA in the mouse.* Mol Cell Biol, 2003. **23**(23): p. 8519-27.

332. Li, J., et al., *Down-regulation of pescadillo inhibits proliferation and tumorigenicity of breast cancer cells.* Cancer Sci, 2009. **100**(12): p. 2255-60.

333. Donati, G., et al., *Selective inhibition of rRNA transcription downregulates E2F-1: a new p53-independent mechanism linking cell growth to cell proliferation.* J Cell Sci, 2011. **124**(Pt 17): p. 3017-28.

334. Russo, A., et al., *Human rpL3 induces G(1)/S arrest or apoptosis by modulating p21 (waf1/cip1) levels in a p53-independent manner.* Cell Cycle, 2013. **12**(1): p. 76-87.

335. Lapik, Y.R., et al., *Physical and functional interaction between Pes1 and Bop1 in mammalian ribosome biogenesis.* Mol Cell, 2004. **15**(1): p. 17-29.

336. Grimm, T., et al., *Dominant-negative Pes1 mutants inhibit ribosomal RNA processing and cell proliferation via incorporation into the PeBoW-complex.* Nucleic Acids Res, 2006. **34**(10): p. 3030-43.

337. Xu, H., et al., *CX-5461 is a DNA G-quadruplex stabilizer with selective lethality in BRCA1/2 deficient tumours.* Nat Commun, 2017. **8**: p. 14432.

338. Khot, A., et al., *First-in-Human RNA Polymerase I Transcription Inhibitor CX-5461 in Patients with Advanced Hematologic Cancers: Results of a Phase I Dose-Escalation Study.* Cancer Discov, 2019. **9**(8): p. 1036-1049.

339. Sun, D., et al., *Why 90% of clinical drug development fails and how to improve it?* Acta Pharm Sin B, 2022. **12**(7): p. 3049-3062.

340. Hughes, J.P., et al., *Principles of early drug discovery.* Br J Pharmacol, 2011. **162**(6): p. 1239-49.

341. Mohs, R.C. and N.H. Greig, *Drug discovery and development: Role of basic biological research.* Alzheimers Dement (N Y), 2017. **3**(4): p. 651-657.

342. Orea-Ordonez, L., S. Masia, and J. Bravo, *Peptides Targeting the Interaction Between Erb1 and Ytm1 Ribosome Assembly Factors.* Front Mol Biosci, 2021. **8**: p. 718941.

343. Pestov, D.G., et al., *ERB1, the yeast homolog of mammalian Bop1, is an essential gene required for maturation of the 25S and 5.8S ribosomal RNAs.* Nucleic Acids Res, 2001. **29**(17): p. 3621-30.

344. Bekes, M., D.R. Langley, and C.M. Crews, *PROTAC targeted protein degraders: the past is prologue.* Nat Rev Drug Discov, 2022. **21**(3): p. 181-200.

345. Xin, Y., et al., *Nano-based delivery of RNAi in cancer therapy.* Mol Cancer, 2017. **16**(1): p. 134.

346. Sendi, H., et al., *Nanoparticle Delivery of miR-122 Inhibits Colorectal Cancer Liver Metastasis.* Cancer Res, 2022. **82**(1): p. 105-113.

10. Acknowledgments

First of all, I would like to thank Dr. Peter Jung for his kind supervision and for allowing me to perform my Ph.D. thesis in his laboratory. He was always open to questions, challenges, and new ideas. I learned many new techniques, and this work's success would have been impossible without him.

I also want to thank Prof. Dr. Heiko Hermeking for agreeing to supervise my thesis and for all the exciting and inspiring discussions about my project during lab meetings and institute seminars. His knowledge and ideas helped me to improve this project.

Moreover, I would like to thank Prof. Dr. Thomas Kirchner and Prof. Dr. Jens Neumann for their collaboration and supply with patient material to set up our living biobank of PDTOs. I also thank Prof. Dr. Frederick Klauschen for providing access to resources.

Special thanks to Ursula Götz, who always supported me with protocols and chemicals, especially in last-minute situations! I also want to thank Dr. Matjaz Rokavec for performing bioinformatics analyses and the rest of the Hermeking lab for their support in the lab, helpful discussions during lab meetings, and the lovely lunch and coffee breaks we had together.

I also appreciate AG Saur for their excellent cooperation. Dr. Markus Tschurtschenthaler and Dr. Miguel G. Silva introduced me to the endoscopy-guided orthotopic transplantation mouse models with much patience, interest, and helpfulness.

Additionally, I want to thank my former colleagues in our group: First, Dr. Sophie Boos, whom I could always count on, and working with her was a pleasure. You taught me a lot in the lab, and I probably would never make it this far without your support. Second, Dr. Vanessa Gebauer, whose genomic expertise was beneficial and always open to answering my questions. Lastly, Dr. Cira Garcia de Durango, our Spanish scientist, brought cheerfulness to our group and knew how to motivate us when having a bad day in the lab.

Finally, I want to thank my friends and parents for their intense emotional support throughout my studies. You were always open to lend an ear to me.